NSF Grant ATM-0121546
and Award #0313747
National Science Foundation

AN INTEGRATED DISPLAY AND ANALYSIS TOOL FOR MULTI-VARIABLE RADAR DISPLAY

by Brenda A. Dolan

Colorado State University

DEPARTMENT OF ATMOSPHERIC SCIENCE

PAPER NO. 753

AN INTEGRATED DISPLAY AND ANALYSIS TOOL FOR MULTI-VARIABLE RADAR DATA

by

Brenda A. Dolan

Department of Atmospheric Science

Colorado State University

Fort Collins, CO 80523

Research Supported by

National Science Foundation

under Grants ATM-0121546 and Award No. 0313747

Fall 2004

Atmospheric Science Paper No. 753

ABSTRACT

AN INTEGRATED DISPLAY AND ANALYSIS TOOL FOR MULTI-VARIABLE RADAR DATA

Doppler and polarimetric radars provide valuable information about the kinematics and microphysics of storms. However, radar products, such as Doppler-derived wind vectors and hydrometeor identification, which assist with in-depth analysis of storms, have not been readily available in (near) real-time. The goal of this project is to develop and integrate radar algorithms currently used in post-processing with meteorological observations to develop a near real-time integrated display and analysis tool for use in nowcasting. This software has been linked to and is now available for real-time radar operations at the CSU-CHILL radar facility.

This methodology was also developed for a network of four Doppler radars, including one polarimetric radar, along the Northern Colorado front range. The four radars include two National Weather Service WSR-88D radars (KFTG and KCYS) and two research radars (PAWNEE and CSU-CHILL) operated by Colorado State University. These four radars form three dual-Doppler pairs, in which the radial velocities can be synthesized to obtain three-dimensional wind vectors. The analysis also incorporates algorithms for hydrometeor identification and rainfall rate estimation using the polarimetric measurements from CSU-CHILL, as well as rain rate calculation using standard midlatitude Z-R relationships.

The software was successfully tested at the CSU-CHILL radar facility during the summer of 2004 using data from three of the radars. CHILL data were available within 3 minutes after a volume scan, WSR-88D was displayed approximately 12 minutes after the start of a volume scan, therefore the dual-Doppler winds lagged by 13-15 minutes after the start of the first volume scan. Among other things, users have the ability to zoom in and out of interesting radar features, change the grid resolution and origin, create vertical cross sections, contour data, and archive data as they use the software in real-time. Despite the lag time, the tool helped diagnose areas of intense rainfall and possible hail, updrafts, and wind field features such as mesocyclones and convergence lines. Two case studies from June 2004 are used to demonstrate the utility of the software in this thesis. The software was found to be a valuable resource for assisting scientists with the real-time analysis and visualization of copious amounts of data from a network of multi-variable radars. This tool could be especially useful during large field experiments, especially those in which one research aircraft requires guidance from ground-based radars.

Brenda A. Dolan
Atmospheric Science Department
Colorado State University
Fort Collins, CO 80523
Spring 2005

ACKNOWLEDGEMENTS

This project would not have been possible without the knowledge and input from many different people. I would like to thank Dr. Steve Rutledge for his direction and enthusiasm for this project. I would also like to thank Dr. Chandrasekar and Dr. William Cotton for serving on my committee and offering their comments. The display widget would not have come together nearly as quickly without the base structure designed and written by Kyle Wiens, and I would like to additionally thank him for all his IDL help and knowledge. Thanks to Paul Hein, who assisted in many ways regarding the programming and computer aspects of this thesis. I extend a grateful thank you to Dr. Rob Cifelli for all his insightful suggestions and discussion. Natalie Tourville and Dennis Flanigan assisted me in working with the NEXRAD level II data. Dr. Larry Carey, Dr. Walt Petersen, Pat Kennedy and Dave Brunkow supported this project with discussions about different aspects of the data processing and interpretation. I would like to thank the entire radarmet group, specifically Sarah Tessendorf, Steve Nesbitt and Margi Cech, for their continuous help and support. This research was funded primarily by the National Science Foundation Information Technology Research grant ATM-0121546 awarded to Colorado State University. This work was supported in part by the Engineering Research Centers Program of the National Science Foundation under NSF Award Number 0313747.

TABLE OF CONTENTS

LIST OF FIGURES

LIST OF TABLES

CHAPTER 1

Introduction

1.1 Motivation

During a field experiment, it is the radar scientist's job to make decisions in real-time using the data available to direct aircraft operations, develop radar scanning strategies to best meet the scientific objectives of the project, do project nowcasting, develop scientific insight, etc. This can be a difficult task, especially for extensive projects involving several aircraft and multiple ground-based sensors. Having too much data available can inhibit operations too, since the scientist may have to take time to interpret many different variables from several radars, and combine them with data from other instruments. An integrated analysis and display tool can aide the scientist in making educated decisions quickly.

In past projects, there have been a wide variety of instruments and data available to radar scientists. During the Cooperative Convective Precipitation Experiment (CCOPE) from May-August 1981, eight radars including seven Doppler and two dual-wavelength, 123 mesonet stations, seven upper-air sounding sites, and 14 research aircraft were involved in the project (Knight, 1982). CCOPE had ten broad scientific objectives, including hydrometeor evolution, cloud lifetime, storm structure and the environment, storm initiation, and the origins of ice. Operations were driven each day by these research objectives, and it was the duty of the six scientists in the Operations Center to use the available data to coordinate the activities in order to meet these objectives (Biter and Johnson, 1982). These six scientists performed the following tasks: One person operated the NCAR Cloud-Physics-2 radar antenna, which was vital to the control center because it provided the radar data for all the radar displays in the center, another coordinated the other seven Doppler radars in the network to insure good multiple-Doppler coverage, and the others directed a subset of the aircraft flying the mission. The overall coordination and daily scientific emphasis were determined by the operations director. The Sunday Creek center was an important factor in the success of a project as large as CCOPE (Biter and Johnson, 1982).

Advances in dual-Doppler observations were made during the Severe Environmental Storms and Mesoscale Experiment (SESAME) in 1979. The National Severe Storm Lab's Norman and Cimarron Doppler radars were used to study a tornado-producing storm near Agawam, Oklahoma. The data collected yielded unprecedented dual-Doppler observations of a tornadic cell (Brown, 1992). Coupled with the documentation of the storm environment by the mesonet and rawinsonde network, as well as WSR-57's, this data set was used to test hypotheses about the process leading to updraft rotation. Heymsfield *et al.* (1983) used the dual-Doppler data combined with satellite data from several channels and sounding data to study the upper-level structure of Oklahoma tornadic storms.

The Oklahoma-Kansas Preliminary Regional Experiment for STORM-Central (OK PRE-STORM) in 1985 integrated many new instruments in one field experiment designed to study the structure and dynamics of mesoscale convective systems (MCSs). PRE-STORM also demonstrated the utility of multiple-Doppler observations and real-time color displays of Doppler radar data (Houze *et al.*, 1989). Although it was a secondary goal of the project, PRE-STORM intended to test a number of new sensing systems and scanning strategies in order to evaluate and optimize them for future research (Cunning, 1986). These observing systems included a number of NWS rawinsonde stations, wind-profilers, a lightning location network, a surface mesoscale network, satellites and a number of radars, both ground based and airborne. Two Doppler radar pairs were operated independently, unless the meteorological situation warranted coordinated scanning. The NOAA Office of Aircraft Operations participated with a P-3 aircraft fitted with a 3 cm vertically scanning tail radar with Doppler capabilities. This airborne radar could either contribute to the dual-Doppler coverage of the ground-based radars, or independently derive the wind field using dual-Doppler techniques given the right flight path (Cunning, 1986). Six Weather Surveillance Radar-1957 radar sites in proximity to the PRE-STORM domain also recorded 2° volume scan data up to six times per hour.

These many atmospheric observing platforms provided unique insights into the characteristics of MCSs. The Doppler radar data revealed real-time kinematic information, specifically mesoscale flow patterns in the stratiform region of a squall-line which were later investigated using dual-Doppler analysis (Houze *et al.*, 1989). Houze *et al.* (1989) recognized "single-Doppler-radar" patterns in the radial velocity that can be used to characterize and interpret MCSs in real-time. Though not all of the data were available for real-time analysis, one of the major goals of the project, which was to achieve a reliable and coordinated observing system for investigating MCSs while incorporating many new sensing systems and sensing strategies, was accomplished (Cunning, 1986).

The hydrometeor identification algorithm described by Vivekanandan *et al.* (1999) was available in real-time during the Cooperative Atmospheric Surface Exchange Study (CASES-97). Vivekanandan *et al.* (1999) comment that results of the fuzzy logic based particle classification approach show important aspects of the microphysical structure of a typical convective thunderstorm. They also note that one advantage of a hydrometeor identification algorithm is that a radar meteorologist is not required to know the intricate details of interpreting polarimetric radar data. The algorithm has been incorporated into the S-Pol precipitation product package and has been available in subsequent field projects such as the Florida component of TRMM/Texas and Florida Underflights (TEFLUN-B) and the North American Monsoon Experiment (NAME) in 2004.

Methods for real-time retrieval of three-dimensional winds from a bistatic multiple-Doppler radar system have been proposed by Wurman (1994), Satoh and Wurman (1999), and Protat and Zawadzki (1999). However, it was not until the joint efforts of the radar groups at the Centre National de Recherches Meteorologiques and Laboratoire d'Aerologie during the Mesoscale Alpine Programme (MAP) in 1999 that real-time dual-Doppler winds were attempted from a ground-based radar network (Chong *et al.*, 2000). The scientific objectives of MAP were to investigate orographically generated and/or heavy precipitation events and study their mechanisms. Winds generated from the real-time dual-Doppler synthesis were primarily used for assistance in aircraft guidance and nowcasting (Chong *et al.*, 2000).

The special observing period (SOP) of MAP took place between 7 September and 15 November 1999 in the Alps of northern Italy. The French RONSARD C-band radar and the Swiss Monte Lema C-band radar comprised the dual-Doppler network. Additionally, the National Center for Atmospheric Research (NCAR) S-Pol (polarimetric) radar was positioned in between the C-band radars to provide validation of the precipitation and microphysical structure. Winds were synthesized at the Project Operation Centre at Milano Linate military airport on a PC-Linux machine using the real-time and automated multiple-Doppler analysis method (RAMDAM) described in Chong *et al.* (2000). Once the wind synthesis was complete, it was displayed using the MountainZebra system developed at the University of Washington (James *et al.*, 2000). The MountainZebra is an interactive system that allows the user to display the dual-Doppler derived winds simultaneously with data from the S-Pol radar, such as hydrometeor identification. An example screen shot is illustrated in Fig. 1.1. The real-time winds were calculated over a 147 km x 147 km x 11 km domain using a grid resolution of 3 km x 3 km x 0.5 km, and processing took approximately 15-20 minutes. The resolution was limited by the transmission of the RONSARD radar data over an ISDN line to the project operation centre. Chong *et al.* (2000) suggest that results from the real-time dual-Doppler analysis were important in determining the precipitation and airflow structure, which aided in the selection of the regions to be sampled by the airborne Doppler radars.

The innovative use and development of real-time data processing algorithms in past field projects has provided motivation and ground work for the software created in this thesis project. The utility of having real-time data from multiple Doppler radars for radar scientists was demonstrated during CCOPE and PRE-STORM, where color displays of velocity helped identify air flow patterns in MCSs. Real-time dual-Doppler winds accessible during MAP supplied scientists with airflow characteristics, which assisted with better nowcasting and direction of the aircraft involved in the project. Additionally, hydrometeor identification using a real-time fuzzy logic algorithm has been an integrated part of radar visualization at S-Pol for several field projects. This has helped radar scientists in determining the microphysical structures of storms in real-time.

The network of radars available along the Front Range of Colorado and Wyoming coupled with the atmospheric observing systems such as the Denver sounding station and surface observation stations provide a plethora of meteorological data for scientists. Therefore, an integrated display and analysis tool to assist in the real-time interpretation and analysis of these data sets would be beneficial to radar scientists working at the CSU-CHILL radar facility.

1.2 Front Range Radars

Data from four S-band radars were used for the development of this multi-variable algorithm. The PAWNEE radar and the Colorado State University – Universities of Chicago and Illinois (CSU-CHILL) radar are research radars maintained and operated by Colorado State University. The PAWNEE radar is a 11 cm S-band Doppler radar located in the Pawnee Grasslands in Northern Colorado (see Fig. 1.2), which can measure the received power, mean velocity, and normalized coherent power. The technical specifications for PAWNEE radar are listed in Table 1.1. The CSU-CHILL radar is a 11.01 cm S-band, well maintained, state-of-the-art dual-polarized Doppler radar located near Greeley, Colorado (see Fig. 1.2). The polarimetric capabilities of CSU-CHILL allow for the measurement of co-polar and cross-polar ratios (Z_{dr}, L_{dr}), as well as phase data (ϕ_{dp}), which will be discussed in Chapter 2, as well as the received power, mean velocity, and normalized coherent power. The technical specifications of CSU-CHILL are listed in Table 1.2. The two research radars cover a significant portion of northern Colorado. Figs. 1.3 and 1.4 illustrate the increasing beam height with increasing slant range for common elevation angles used by the research radars.

In addition to CSU-CHILL and PAWNEE, two National Weather Service (NWS) Weather Surveillance Radar-1988 Doppler (WSR-88D) radars were used. The Denver-Front Range (KFTG) radar located near Denver, Colorado (see Fig. 1.2), and the Cheyenne (KCYS) radar located in Cheyenne, Wyoming (see Fig. 1.2) are 10.3-11.01 cm S-band Doppler radars, with the capabilities to measure received power, radial velocity, and spectral width. Technical specifications of the NWS NEXt generation RADar (NEXRAD) network are shown in Table 1.3. The WSR-88D has four different scanning strategies, called Volume Coverage Patterns (VCPs), which are selected by the NWS scientist to optimize the sampling of certain types of weather while still providing coverage of the entire domain. Volume Coverage Pattern 31, or 'clear-air mode', is used to detect air mass discontinuities, wind profiles, and the onset of convection using 5 elevation angle sweeps over 10 minutes with a long pulse length. This pattern is shown in Fig. 1.5. VCP 32 is similar to VCP 21, but uses a shorter wave pulse. In these two modes, a separate surveillance and Doppler scans are performed for each of the lowest three elevation angles. This is done to help eliminate second trip echo. When precipitation is in the coverage area, VCP 11, or " Severe Weather Precipitation Mode", is used. This VCP uses 14 elevation angle sweeps in 5 minutes at a short wave pulse, shown in Fig. 1.6. When storms are farther away, the antenna is slowed down in order to provide more accurate radial velocity data for a second precipitation mode, VCP 21. This sweeps out 9 elevation angles in 6 minutes (Fig. 1.7). Both precipitation modes use separate surveillance and Doppler scans at the lowest two elevation angles.

1.3 Objectives and Organization of Thesis

The four radars described above provide coverage from southern Wyoming through northern and central Colorado. They form three dual-Doppler networks that can assist in determining the kinematic and, supplemented by the polarimetric measurements from CSU-CHILL, microphysics of storms along the front range. However, data from four Doppler radars can be difficult to interpret and analyze in real-time. The objective of this thesis was to investigate, develop, and test software using data from all four radars, as well as supplemental meteorological data, to efficiently and quickly provide processed data for analysis in real-time.

This thesis is organized into five chapters. Radar variables, multiple Doppler analysis, and algorithms for derived radar products will be discussed in Chapter 2.

The software developed for this study will be detailed in chapter 3, including the program specifications, data processing and examples of output. Two case studies in which the software was used at the CSU-CHILL radar facility will be examined in chapter 4. In chapter 5 conclusions from this work will be drawn, and future work to build off this study will be proposed.

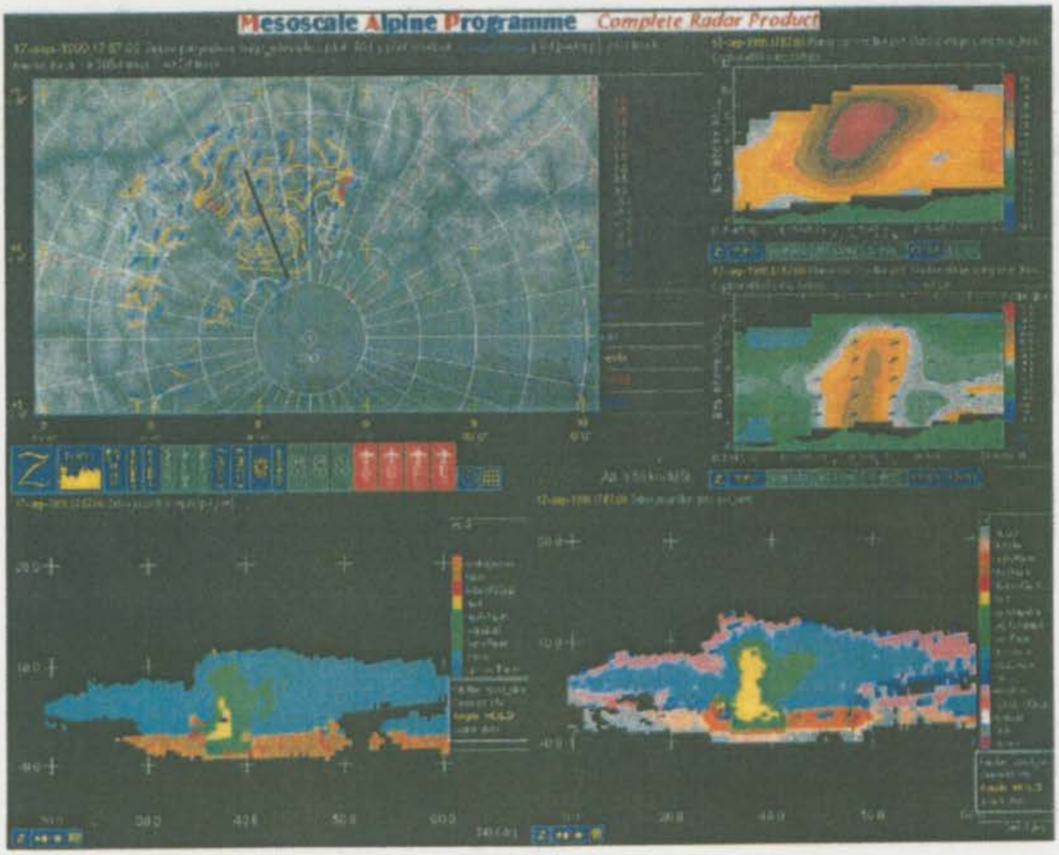

Figure 1.1: An example real-time screen shot from the MAP experiment in 1999 using the MountainZebra visualization package. This shows three-dimensional wind field vectors (upper panels, blue arrows) from RONSARD and Monte Lema radar data overlaid on background topography, and particle-type distribution from S-Pol data (lower panels) at 1757 UTC 17 Sep 1999. The upper right panels show vertical reflectivity and radial velocity from S-Pol data, with wind vectors from the dual-Doppler synthesis between RONSARD and Monte Lema (from Chong *et al.*, 2000).

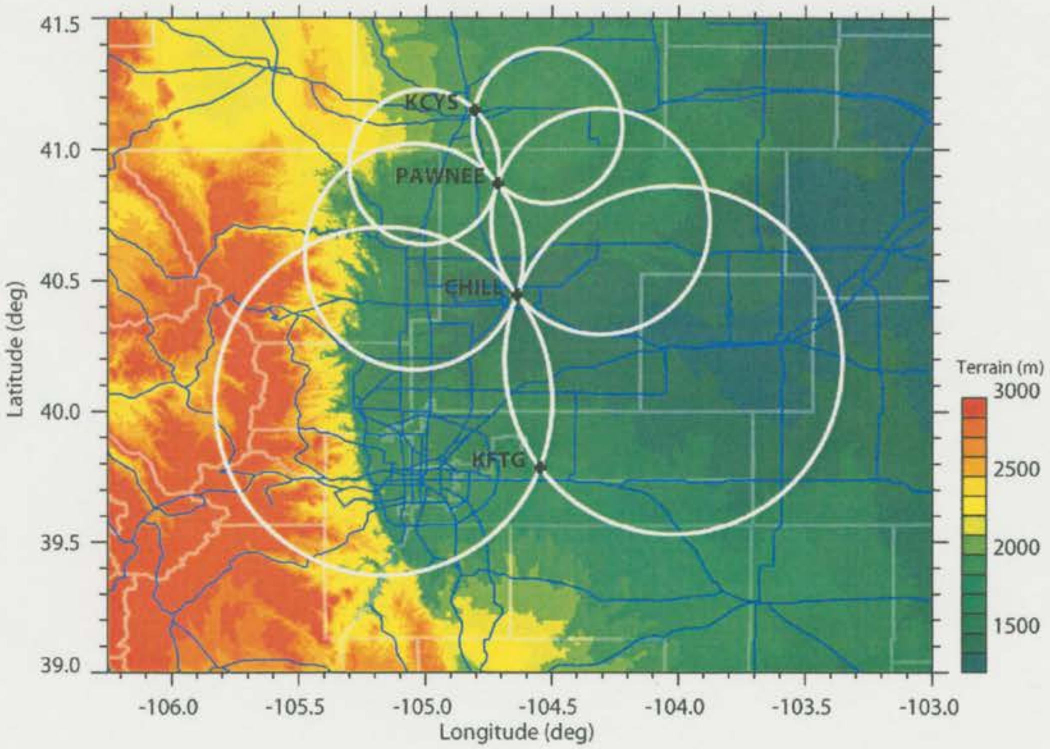

Figure 1.2: The Northern Colorado Doppler radar network. From top, Cheyenne, WY WSR-88D (KCYS), PAWNEE, CSU-CHILL, and Denver, CO WSR-88D (KFTG). The white circles depict the 30° dual-Doppler beam crossing angles, and the shaded colors indicate the topography of the region in meters. The blue lines indicate major roads and rivers, light grey lines are state and county boundaries.

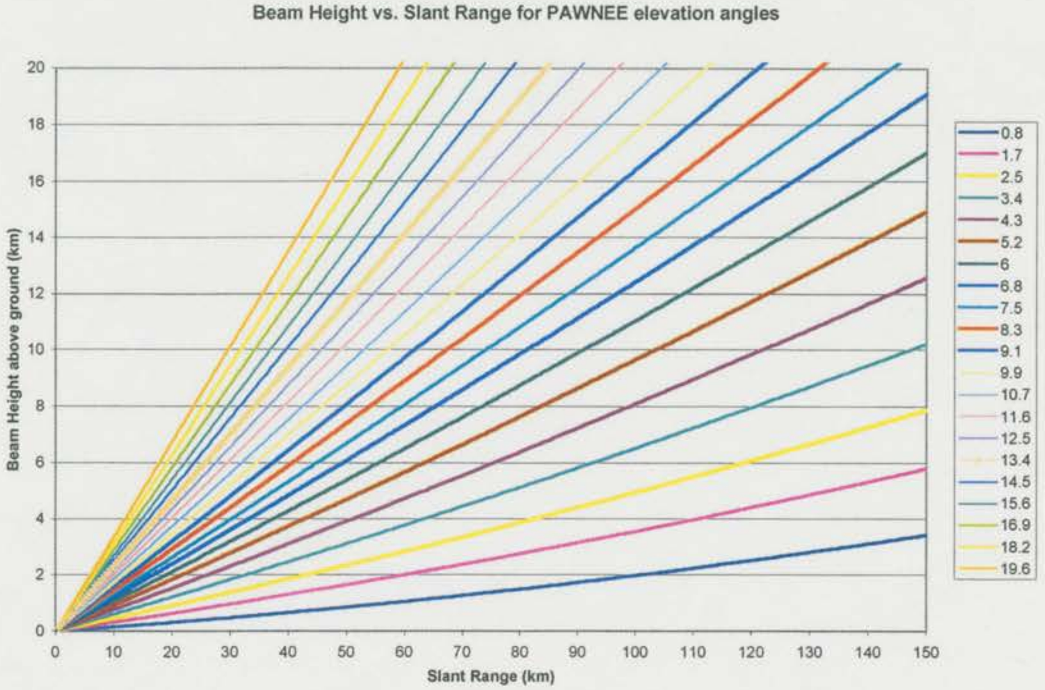

Figure 1.3: Beam height versus slant range for several common elevation angles for the PAWNEE radar. Range and beam height are in km.

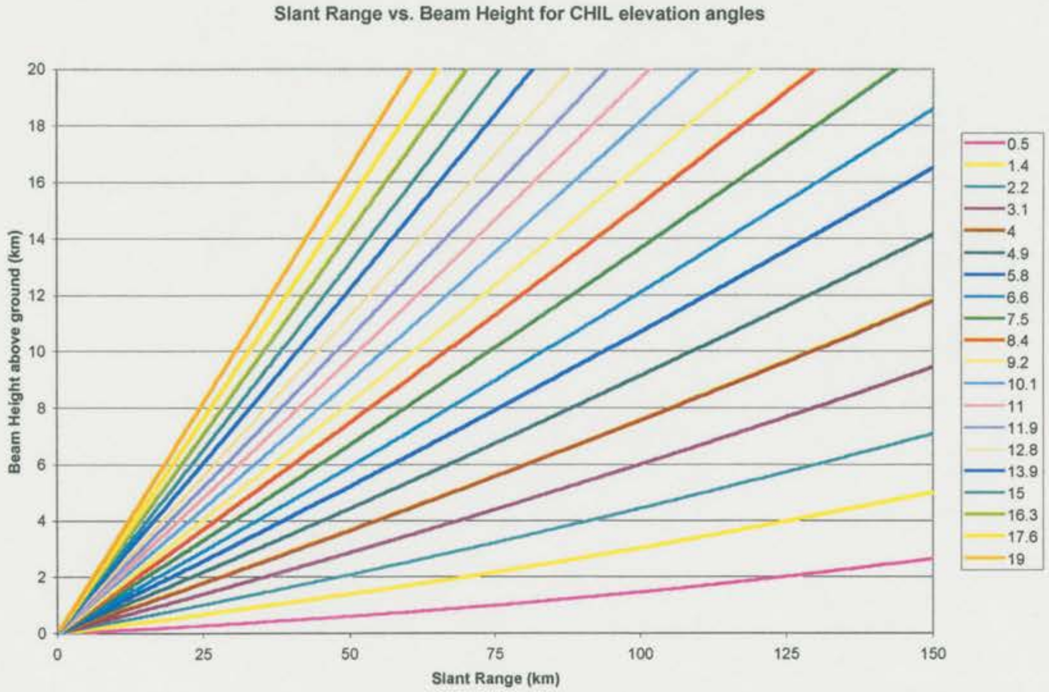

Figure 1.4: Beam height versus slant range for several common elevation angles for the CSU-CHILL radar. Range and beam height are in km.

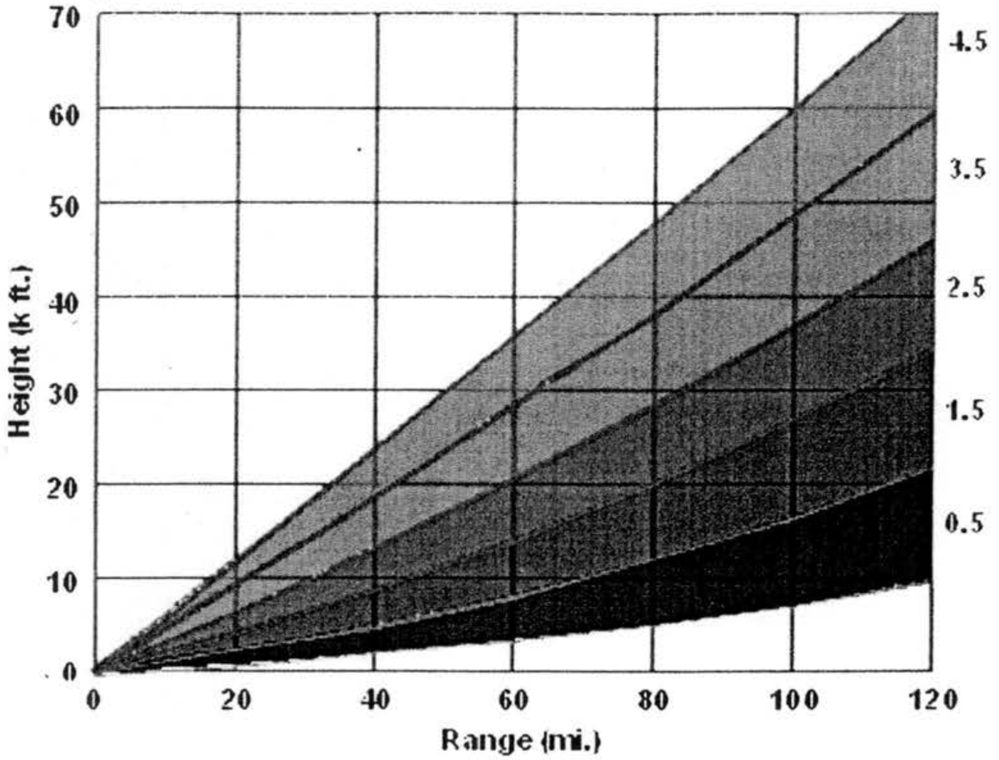

Figure 1.5: WSR-88D scanning strategy for Volume Coverage Patterns 31 and 32, clear-air mode. Scan includes 5 elevation angles up to 4.5° with a 10 minute repetition cycle. Range is in miles (1 km = 0.621 miles) and height is in kilo feet (1 kft = 0.3048 km).
(URL: http://www.srh.noaa.gov/radar/radinfo/vcp31.html, 2004)

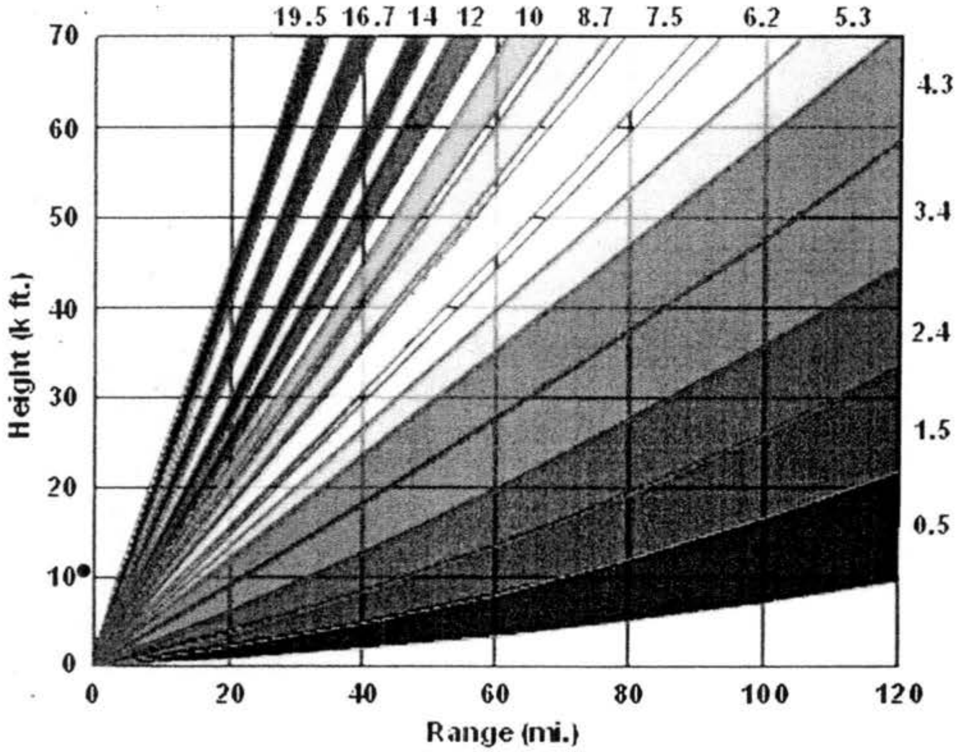

Figure 1.6: WSR-88D scanning strategy for Volume Coverage Pattern 11, severe weather precipitation mode. Scan includes 14 elevation angles up to 19.5° in a 5 minute repetition cycle. Note the gaps in the coverage at the high elevation angles. Range is in miles (1 km = 0.621 miles) and height is in kilo feet (1 kft = 0.3048 km). (URL: http://www.srh.noaa.gov/radar/radinfo/vcp11.html, 2004)

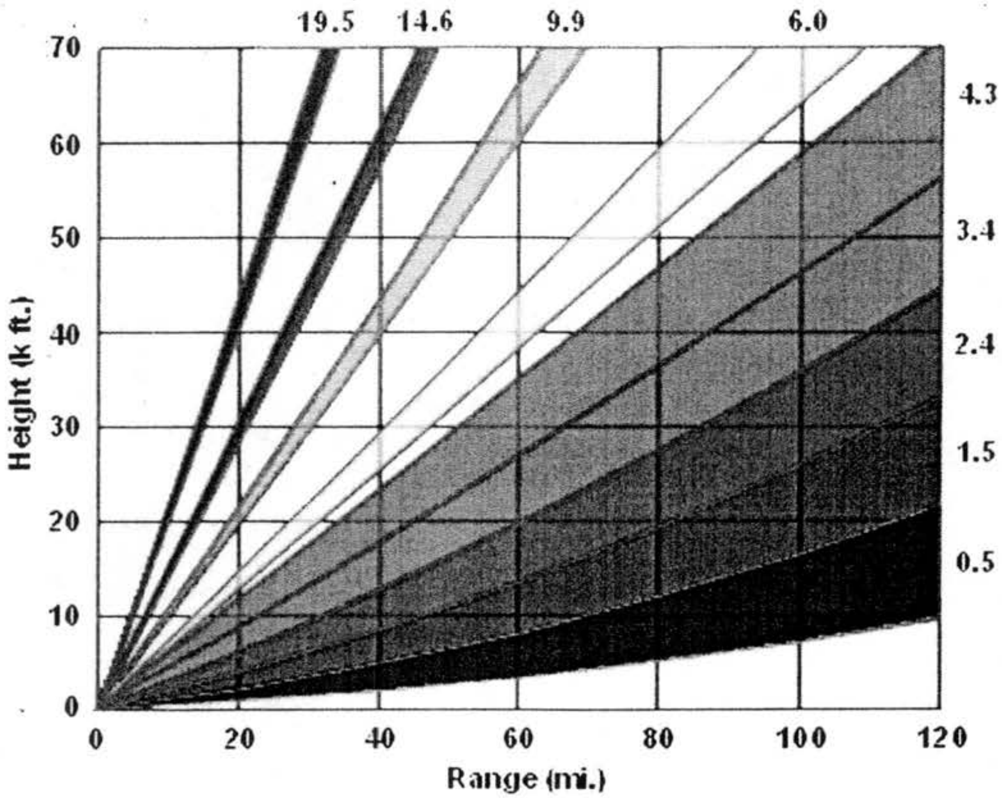

Figure 1.7: WSR-88D scanning strategy for Volume Coverage Pattern 21, precipitation mode. Scan includes 9 elevation angles up to 19.5° in a 6 minute repetition cycle. Note the large gaps in the coverage at the high elevation angles. Range is in miles (1 km = 0.621 miles) and height is in kilo feet (1 kft = 0.3048 km). (URL: http://www.srh.noaa.gov/radar/radinfo/vcp21.html, 2004)

Table 1.1 Technical specifications for the PAWNEE radar (from http://chill.colostate.edu).

General

Wavelength	10.99 cm
3 dB beamwidth	1.6°
Peak transmit power (kW)	380 typ.
Pulse duration	1 μs
Pulse repetition frequency	500-1299 Hz, 990 Hz typ.
Noise Power (SNR=1)	-109 dBm
Polarization	V
Pulses per integration cycle	40-2048, 128 typ.

Location

Latitude	40.871 N
Longitude	-104.715 W
Horn elevation	1688 m MSL

Table 1.2: Technical specifications for the CSU-CHILL radar (from http://chill.colostate.edu).

Antenna

Shape	Parabolic
Diameter	8.5 m
Feed type	Scalar
Gain	43 dB(includes waveguide loss)
3 dB Beamwidth	1.1 deg
Maximum sidelobe	-27 dB
Inter-channel isolation	-45 dB
ICPR (two-way)	-34 dB

Transmitters

Wavelength	11.01 cm
Peak Power	800-1000 kW
Final PA Type	VA-87B/C (Klystron)
PRT Range	800-25000 μs
Pulse Width	0.3-1.0 μs
Available Polarizations	Horizontal, Vertical, slant 45°/135°, left/right circular

Receivers/ Digital Signal Processing

Noise Figure	-3.4 dB
Noise Power @SNR=1	-114.0 dBm
Dynamic range	-96 dB
Bandwidth	750 KHz typ. programmable filter
Output Range Resolution	50.75, 150 m
Maximum Range gates	Estimated to be >3000

Table 1.2 (cont.)

Location

Latitude	40.44625 N
Longitude	-104.6371 W
Horn Elevation	1432 m MSL

Table 1.3: Technical Specifications for the NWS WSR-88D radars.

General

Wavelength	10.0-11.1 cm
Frequency	2.8-3.0 GHz
Peak Power	750 kW
Antenna diameter	8.5 m
3 dB beamwidth	0.95°
Rotation Rate	36° s^{-1}, typ.
PRF	318-1304 s^{-1}
Pulse Length	1.57 and 4.7 μs
Gain	45 dB

KFTG Location

Latitude	39.7867 N
Longitude	-104.5458 W
Horn Elevation	1675 m MSL

KCYS Location

Latitude	41.1519 N
Longitude	-104.8061 W
Horn Elevation	1867 m MSL

CHAPTER 2

Theory and Methods

2.1 Doppler Radar Variables

Radars have been used since World War II to observe weather. Present day radars operate at various wavelengths to study clouds, precipitation, particle types, and turbulent air motions in the planetary boundary layer (Houze, 1993). This study uses data from four S-band (~10 cm) Doppler radars, one with polarimetric capabilities, to determine rain rates remotely, infer bulk hydrometeor types, and synthesize 3D wind fields using a dual-Doppler network. This chapter will discuss the radar variables and the theory behind multiple Doppler analysis, hydrometeor identification retrieval, and rain rate estimation.

2.1.1 Reflectivity, Z

Reflectivity is a measure of the amount of transmitted power backscattered by a radar sample volume. If the size of the target is sufficiently small compared to the wavelength of incident electromagnetic radiation, the scattering is dominated by Rayleigh processes. Under Rayleigh conditions, the equivalent reflectivity factor depends on the target diameter to the sixth power, as shown in Eqn. 2.1:

$$Z = \int_0^\infty N(D,r)D^6 dD \qquad [\mathrm{mm}^6\ \mathrm{m}^{-3}] \tag{2.1}$$

where D is the diameter of the particles, and N(D,r) is the number density of targets at range r with diameter D. Because of the 6th power dependence, relatively few large particles can dominate the returned power.

The Rayleigh approximation is valid when α <0.22, where α is calculated from Eqn. 2.2:

$$\alpha = \frac{2\pi a}{\lambda} \tag{2.2}$$

where a is the particle radius, and λ is radar wavelength. For S-band (~10-11 cm), the Rayleigh approximation can be used for liquid particles with diameters smaller than 7 mm. This encompasses nearly all meteorological particles except large hail.

Departure from the Rayleigh regime, defined as the Mie scattering, is characterized by more enhanced scattering and absorption, which decreases the backscattering cross-section. The general equation for the power returned to the radar in a 'no loss' system is a function of the range (r) squared, the radar constant (C), and the dielectric factor (K) as well as the equivalent reflectivity (Eqn. 2.3):

$$P_r = \frac{|K|^2 C Z_e}{r^2}. \tag{2.3}$$

The radar constant contains constants as well as terms that depend on the engineering of the radar system, such as the gain, half-power antenna beam width, transmitted power, pulse length and radar wavelength. The value of $|K|^2$ is assumed to be that of pure water, which is 0.93; for any other type of targets, a correction must be applied. For example, a pure ice target would have a $|K|^2$ value of 0.197 because ice is much less dense and has a smaller degree of polarizability compared to water. Chandrasekar *et al.* (1991) present the following correction for the reflectivity:

$$dBZ_{ice} = 7.2dB + dBZ_e. \qquad (2.4)$$

Reflectivity in the form of Eqns. 2.1 and 2.3 is in linear units, mm^6 m^{-3}. Since reflectivity of meteorological echo can span many orders of magnitude, a logarithmic scale is often used, defined by Eqn. 2.5:

$$Z(dBZ) = 10\log_{10} Z \qquad \text{[dBZ]} \qquad (2.5)$$

where the new unit is dBZ (Doviak and Zrnić, 1993). In the logarithmic based scale, reflectivities can range from 0 dBZ in cumulous congestous clouds to greater than 60 dBZ in regions of heavy rain and hail (Doviak and Zrnić, 1993).

Although reflectivity has been used for decades to help determine hydrometeor type, specifically to identify hail, Dye and Martner (1978) demonstrated that reflectivity factor alone could not discriminate hail in Northern Colorado thunderstorms. New techniques use polarimetric variables in addition to reflectivity in order to remove some ambiguity introduced by assumptions about the dielectric factor and drop size distribution. These new techniques will be discussed in section 2.4.1.

2.1.2 Radial Velocity, V_r

Pulsed Doppler radars can detect very small modulations of the radar frequency from returned electromagnetic pulses, called the Doppler shift. The Doppler shift frequency, f, is related to the radial velocity, v_r, by the wavelength, λ, (Eqn. 2.6):

$$f = \frac{2v_r}{\lambda} \qquad (2.6)$$

The radial velocity is a measure of the mean (power-weighted) velocity of particles in a given volume. Only radial motion towards (inbound) or away (outbound) from the radar can be measured. Radial velocity is measured in units of ms^{-1}. A full description of Doppler radar techniques is presented in Doviak and Zrnić (1993) and Bringi and Chandrasekar (2001).

Since the radial velocity is a measure of the frequency shift relative to the radar frequency, an ambiguity arises in measuring the radial velocity. The maximum unambiguous velocity measurable by a radar is called the Nyquist velocity. For example, a target moving at a speed such that the frequency is shifted by $\lambda/2$ between two consecutive radar pulses could represent either an outbound or an inbound velocity. The result is that all velocities measured by the radar will fall into an interval, called the Nyquist interval, which is a function of the pulse repetition frequency, or PRF (Rinehart, 1997). This relationship is shown in Eqn. 2.7

$$v_{\max} = \pm \frac{PRF \bullet \lambda}{4}. \qquad [\mathrm{m\ s^{-1}}] \qquad (2.7)$$

Any velocities greater than the Nyquist velocity are said to be "folded". This folding must be accounted for in the processing of the data, which will be discussed in section 3.2.3.

2.2 *Polarimetric Variables*

A polarimetric radar, such as CSU-CHILL (http://www.chill.colostate.edu), is able to transmit and receive different polarizations of electromagnetic waves. Figure 2.1 illustrates a vertically and horizontally polarized electromagnetic wave. The following discussion of the polarimetric variables assumes horizontal and vertical orientation, though CSU-CHILL is also able to transmit circular and slant 45 polarization states as well. CSU-CHILL has the ability to transmit the horizontal and vertical pulses alternately or simultaneously. In most cases, the alternate transmission mode is used, allowing for the retrieval of the cross-polar signal, or the signal returned in the polarization orthogonal to that which was transmitted. The co-polar signal is when the received and transmitted signals have the same polarization. In the following discussions, the subscripts h and v will refer to the horizontal and vertical polarizations, and the first subscript will describe the polarization of the transmitted wave, while the second indicates the polarization of the received wave. For example, Z_{hv} means h is transmitted and v is received.

2.2.1 *Difference Reflectivity, Z_{dp}*

Difference reflectivity is the difference between the vertical reflectivity, Z_v, and the horizontal reflectivity, Z_h (Eqn. 2.8):

$$Z_{dp} = 10\log_{10}(Z_{hh} - Z_{vv}). \qquad \text{[dB]} \qquad (2.8)$$

If ice particles are assumed to be isotropic scatterers, the power returned in the horizontal and vertical polarizations will be approximately the same (i.e.: Z_{hh}=Z_{vv}). Thus, difference reflectivity is useful in determining the ratio of ice scatterers to raindrops in mixed phase regions. The reflectivity will be the sum of the reflectivity due to raindrops and the reflectivity due to ice (Eqn. 2.9):

$$Z_h = Z_h^{ice} + Z_h^{rain};\ Z_v = Z_v^{ice} + Z_v^{rain} \qquad [\mathrm{mm^6\ m^{-3}}] \qquad (2.9)$$

Considering the random orientation, spherical nature, and low dielectric for the ice hydrometeors, the component of reflectivity due to ice should be the same in both the horizontal and vertical. However a raindrop, which tends to flatten into an oblate spheroid shape as it falls, will return a larger signal along the major axis. The result is that Z_{dp} is only sensitive to oblate raindrops and any difference reflectivity greater than zero is presumed to be from rain.

In situations where only rain is present, Z_{dp} and Z_h^{rain} are physically highly correlated despite wide variations in the drop size distribution. Additionally, the statistical coefficient between Z_h and Z_{dp} tends toward unity. These high correlations lead to a clustering of data along a straight line, termed the 'rain line' (Bringi and Chandrasekar, 2001). The equation for this line is Eqn. 2.10

$$Z_{dp} = a(10\log_{10} Z_h^{rain}) + b. \qquad (2.10)$$

Carey and Rutledge (1996) used data from a multi-cell thunderstorm in Colorado on 21 May 1993 to empirically determine the coefficients of the rain line, leading to Eqn. 2.11

$$Z_{dp} = 1.10 Z_h - 9.36. \qquad \text{[dB]} \qquad (2.11)$$

The rain line is illustrated using the Carey and Rutledge (1996) data in Fig. 2.2. Deviations of data points from the rain line are assumed to be associated with mixed-phase regions and can be used to determine the ice fraction in a resolution volume (Bringi and Chandrasekar, 2001). Although the rain line can vary depending on the drop size distribution, the findings of Carey and Rutledge (1996) were similar to results of Conway and Zrnić (1993) who studied a severe Colorado hailstorm and theoretical studies done by Golestani *et al.* (1989). This is a powerful method of eliminating ice contamination in rainfall estimates; this will be discussed further in section 2.4.2.

2.2.2 *Differential Reflectivity, Z_{dr}*

Differential reflectivity is the logarithmic ratio of the co-polar powers, that is the ratio of horizontal received power to the vertical received power given horizontally and vertically transmitted waves. Z_{dr} is represented by Eqn. 2.12:

$$Z_{dr} = 10\log\left(\frac{Z_{hh}}{Z_{vv}}\right) \qquad \text{[dB]} \qquad (2.12)$$

Differential reflectivity has units of dB.

Differential reflectivity is indicative of the mean axis-ratio of hydrometeors. Spherical particles, such as small rain drops, will have nearly the same Z_{hh} and Z_{vv} values, yielding a Z_{dr} value near zero. Large raindrops become oblate as they fall, due to the combined effects of gravity, surface tension and aerodynamic forces (Pruppacher and Beard, 1970; Beard and Chuang, 1987), reducing the vertical co-polar power from that of the horizontal co-polar power. This results in Z_{dr} values above zero, ranging from 0-5 dB (Houze, 1993). Wind tunnel studies done at the Cloud Physics Group at UCLA provided Z_{dr} values for a range of particle sizes and axis ratios. These results are shown in Fig. 2.3.

Z_{dr} is also sensitive to the dielectric constant and therefore the polarizability of the target. Thus, for two particles with the same axis ratio but different composition such as ice and water, the Z_{dr} can be significantly lower for large ice particles due to its reduced dielectric constant. This concept is illustrated in Fig. 2.4 from Bringi and Chandrasekar (2001). Large hailstones have Z_{dr} values near zero due to their nearly spherical shapes, or their tendency to tumble as they fall. Their low dielectric response to incident radiation is also a significant factor (Aydin *et al.*, 1984). These characteristics about the shape and density of particles can be exploited to help determine the hydrometeor type (see discussion in section 2.4.1), as well as identifying the radar brightband.

2.2.3 *Linear Depolarization Ratio, L_{dr}*

The linear depolarization ratio is the ratio of cross-polar return to the co-polar return. That is, when a horizontally polarized wave is transmitted, the vertically polarized return signal is measured and compared to the horizontal return. Equation 2.13 shows this relationship:

$$L_{dr,hv} = 10\log_{10}\left(\frac{Z_{hv}}{Z_{hh}}\right) \qquad [\mathrm{dB}] \qquad (2.13)$$

A cross-polar signal results when a spheroid-like hydrometeor is not aligned with its major or minor axis parallel or perpendicular to the incident electric field. Misalignment occurs due to the wobbling of oblate spheroids as they fall, yielding an assortment of canting angles. L_{dr} increases with increasing dielectric strength, more irregular shapes, and increasing axis ratio. Symmetric particles or particles aligned with the electric field will result in no cross-pole return, and L_{dr} will approach negative infinity. Doviak and Zrnić (1993) present the following values for different types of hydrometeors: snowflakes ~-32 dB, oblate dry hail or graupel –20 dB, and rain –30 dB (Fig. 2.5) Values greater than –20 dB are expected to be wet aggregates or wet, tumbling ice particles such as hail. It should also be noted that surface wetting increases depolarization for a given shape and orientation.

L_{dr} provides information about the orientation, shape and phase of hydrometeors. This information aids in the determination of hydrometeor type, as will be discussed in section 2.4.1. However, it should be noted that L_{dr} is susceptible to more noise contamination than some of the other variables since the cross-polar power returned is close to two orders of magnitude below the co-polar signal (Doviak and Zrnić, 1993).

2.2.4 *Correlation Coefficient, ρ_{hv}*

The correlation coefficient, ρ_{hv}, is the correlation of the co-polar received power in the horizontal polarization to the co-polar power received in the vertical polarization (Eqn. 2.14).

$$\rho_{hv} = \frac{\left|\left\langle S_{vv} S_{hh} \right\rangle\right|}{\left(\left\langle \left|S_{hh}\right|^2 \right\rangle \left\langle \left|S_{vv}\right|^2 \right\rangle\right)^{1/2}} \qquad (2.14)$$

where $|\langle S_{hh}S_{vv}\rangle|$ is the magnitude of the average of the co-polar powers and similarly, $\langle |S_{hh}|^2\rangle$ and $\langle |S_{vv}|^2\rangle$ are the average squares of the magnitude of the co-polar power. The correlation coefficient is discussed in terms of zero lag time, meaning the horizontal and vertical pulses are assumed to be transmitted at the same time. Phase shift differentials resulting from scattering, canting angles, irregular shapes, eccentricity, and mixtures of hydrometeor types can all influence the correlation coefficient (Doviak and Zrnić, 1993). The correlation coefficient is mainly an indicator of the variability of hydrometeor types within a radar volume. For rain, ρ_{hv} is near unity; it is depressed for rain/hail mixtures, and large oblate tumbling hail. Depressed values for metrological echoes rarely fall below 0.8. As will be discussed in section 3.2.2, ρ_{hv} can be used to discriminate between meteorological and non-meteorological echo.

2.2.5 *Differential Propagation Phase, Φ_{dp} and Specific Differential Phase, K_{dp}*

As a transmitted electromagnetic wave propagates through a medium containing oriented, non-spherical particles (such as raindrops), the resulting electric field will be a combination of the transmitted wave and the forward scattered wave. Thus the electric field at a point P from the radar will have a different phase angle than the transmitted wave. This change in phase angle is referred to as the propagation phase shift. The contribution from forward scattering will depend on the polarization of the transmitted wave. The resulting differential between horizontal and vertical polarizations is called the differential phase shift, ϕ_{dp} (Jameson, 1984). The total differential phase in degrees, Ψ_{dp}, is represented as the addition of the propagation effects and the 'backscatter differential phase', δ (Eqn. 2.15).

$$\Psi_{dp} = \phi_{dp} + \delta \qquad \text{[deg]} \qquad (2.15)$$

In Rayleigh conditions, δ is zero. At S-band wavelengths, raindrops fall under Rayleigh conditions, and therefore the total differential phase is solely due to propagation effects (i.e.: $\Psi_{dp}=\phi_{dp}$). Oblate particles, such as large raindrops, will result in a positive phase shift, while prolate particles, such as vertically oriented ice crystals aligned in an electric field, will result in a negative phase shift. It is also important to note that isotropic hydrometeors such as hail will not affect the differential because the phase will be shifted equally in the horizontal and vertical planes.

Taking a range derivative of the differential phase assuming Rayleigh conditions, the specific differential phase, K_{dp}, for a volume can be calculated (Eqn. 2.16).

$$K_{dp} = \frac{1}{2}\frac{\delta\phi_{dp}}{\delta r} = \frac{\left|\phi_{dp}(r_2) - \phi_{dp}(r_1)\right|}{2(r_2 - r_1)} \qquad [\text{deg km}^{-1}] \qquad (2.16)$$

where r is the range to the target from the radar, and the factor of two accounts for the two-way propagation distance. K_{dp} is measured in units of deg km^{-1}.

Jameson (1984) points out that the propagation phase shift is proportional to both the mass weighted mean axis ratio, R, (resulting in a large differential phase shift as the drop axis ratio deviates from unity) and the liquid water content, W (Eqn. 2.17):

$$\phi_{dp} = \frac{108}{\pi^2} W\lambda C(1-R) \qquad \text{[deg]} \qquad (2.17)$$

where C is a wavelength-dependant constant, λ is the wavelength of the radar, and R is given by:

$$R = \frac{\int D^3 r N(D) dD}{\int D^3 N(D) dD}. \qquad (2.18)$$

K_{dp} will increase with mass and oblateness, but decrease with increasing radar wavelength. This is a powerful result because it suggests that given a phase shift in a volume and a mass weighted mean axis ratio, the liquid water content can be estimated without assumptions about the drop size distribution (Jameson, 1984). Since K_{dp} is only affected by anisotropic particles such as oblate raindrops, even in mixed phase regions, it can be used to estimate rainfall, and is especially useful in cases of high rain rates (Chandrasekar *et al.*, 1990). The applications of K_{dp} in rainfall estimation will be discussed further in section 2.4.2.

Due to the statistical fluctuations of scatterers within a volume, measurement of Ψ_{dp} is generally noisy. In order to calculate a meaningful K_{dp}, the high frequency fluctuations are filtered out through a low pass filter, and a regression (a higher order polynomial) is fit to Ψ_{dp}, resulting in a regression curve representing ϕ_{dp} (Bringi and Chandrasekar, 2001). Since specific differential phase is a calculated variable and not a measured variable, some uncertainties are introduced by method of calculation, specifically the filtering, which may remove real fluctuations caused by Mie scatterers such as hail. Filtering can also degrade the spatial resolution and amplitude of the retrieved rainfall. Nonetheless, K_{dp} is a powerful variable, and as will be discussed in 3.2.2, ϕ_{dp} can be used to differentiate meteorological targets from clutter.

2.3 Multiple Doppler Analysis

2.3.1 Dual-Doppler Networks

Dual-Doppler radar coverage is a function of the coverage area and spatial resolution. Dual-Doppler winds can be retrieved if the beam-crossing angle between the two radars is sufficiently large (> 30° in practice). At smaller beam-crossing angles, both radars measure a radial velocity that is nearly equal in magnitude but opposite in direction, which provides no information about the wind component perpendicular to the radial. Because of this argument, wind vectors along and surrounding the baseline between the two radars cannot be retrieved. The beam-crossing angle, or the angle between intersecting beams, is related to the error variance of the u and v wind components as well as the two individual radars (Lhermitte and Miller, 1970). This relationship is shown in Eqn. 2.19.

$$\frac{\sigma_u^2 + \sigma_v^2}{\sigma_1^2 + \sigma_2^2} = \csc^2\beta \equiv b \tag{2.19}$$

where σ is the error variance and the subscript represents the u and v components of the velocity (retrieved by the dual-Doppler solution) and the individual error variance for radars 1 and 2, and β is the beam-crossing angle. Assuming a constant radar error variance, increasing the beam-crossing angle will decrease the error variance of the winds (Davies-Jones, 1979). The dual-Doppler area in which all beam-crossing angles are greater than β is described by two circles centered at (0,+/-dcotβ) with radii dcsc(β) (Fig. 2.6), assuming the radars are located at (+/-d,0). The spatial resolution and minimum beam height must also be considered when determining the feasibility of combining two radars in a dual-Doppler network. If the baseline is too long, then the spatial resolution will be degraded, and at the far edges of the Doppler lobes the radar beams will be well above ground (see Figs. 1.3-1.7 for slant range vs. beam height for each radar). However, longer baselines result in larger spatial coverage. As Davies-Jones (1979) notes, the type of phenomenon being studied should dictate the restrictions on aerial coverage and spatial resolution.

Applying the abovementioned considerations for dual-Doppler networks, the four radars located along the Colorado and Wyoming front range allow for three dual-Doppler pairs: KCYS and PAWNEE, PAWNEE and CSU-CHILL, and KFTG and CSU-CHILL. For the purposes if this study, the minimum beam-crossing angle was set at 30°. The area enclosed by beam-crossing angles excluding 30° for each dual-Doppler network is shown in Fig. 1.2. Table 2.1 describes the areal coverage, baseline, distance to farthest point from each radar and spatial resolution at 100 km for each dual-Doppler pair.

PAWNEE and CSU-CHILL have been strategically placed as to maximize the dual-Doppler coverage area. The baseline between the two is 47.677 km, and they are aligned north to south in order to be perpendicular to the average mean flow, maximizing the amount of time a storm spends in the dual-Doppler coverage area. A fourth pair, CSU-CHILL and KCYS, could be considered for a dual-Doppler analysis, but the baseline is nearly 80 km, and the spatial resolution at the farthest points would be almost 2.8 km.

2.3.2 Retrieval of winds from two Doppler radars

The method for determining the three dimensional wind field from a pair of Doppler radars is described in Armijo (1968) and O'Brien (1970). For two radars observing a point P(x,y,z), the radial components of velocity are (assuming radar 1 is located at the origin and radar 2 is located along the y-axis):

$$V_1(x,y,z) = \frac{1}{R_1}\left[xu + yv + z(w + V_t)\right] \tag{2.20a}$$

$$V_2(x,y,z) = \frac{1}{R_2}\left[(x - x_2)u + yv + z(w + V_t)\right] \tag{2.20b}$$

where R is the distance from the radar to the point, and V_t is the terminal fall speed of the precipitation particle. The equation of continuity (Eqn. 2.21) can be used to supplement these two equations, providing a system of three equations (2.20a, 2.20b, and 2.21) with four unknowns (u, v, w, and V_t).

$$\frac{\delta u}{\delta x} + \frac{\delta v}{\delta y} + \frac{\delta w}{\delta z} = kw \tag{2.21}$$

where k is –δ(ln p)/δz (Armijo, 1969). Standard V_t-Z relationships can be used to estimate the V_t for a volume, reducing the system to one with three equations and three unknowns. Solving Eqn. 2.20 for u and v results in Eqns. 2.22a, b.

$$u = \frac{1}{x_2}(R_1V_1 - R_2V_2) \tag{2.22a}$$

$$v = \frac{1}{yx_2}\left[(x_2 - x)R_1V_1 + xR_2V_2\right] - \frac{z}{y}(w + V_t) \tag{2.22b}$$

If 2.22a and 2.22b are substituted into Eqn. 2.21, the result is a linear, inhomogeneous, hyperbolic partial differential equation which can be solved using the method of characteristics or an iterative method assuming w=0 initially.

O'Brien (1970) describes three methods for determining the vertical velocity, w: upward, downward, and variational. These stem from the method of integration of the continuity equation, whether it be ground up (upward), top down to surface (downward), or top down with a redistribution of the error (variational). Downward integration minimizes the residual errors at the surface due to the exponential decrease in density with height (Bohne and Srivastiva, 1975). The downward method was used for the purposes of this thesis.

2.4 Derived Radar Products

2.4.1 Bulk Hydrometeor Identification using Fuzzy Logic

As described in section 2.2, the microphysical characteristics of hydrometeors lead to differences in the scattering and propagation of polarized waves which are manifested in the polarimetric variables. Thus, the polarimetric radar observables yield information about the particle size, particle shape, phase, bulk density, and particle orientation of hydrometeors in a bulk sense. It is most useful to combine the radar observables to determine a 'most probable' hydrometeor type since there is some overlap in the characteristics each variable describes. As Liu and Chandrasekar (2000) suggest, a decision tree could be used, but it is not preferable because the measurement set for different hydrometeor types is not mutually exclusive, and does not allow for measurement errors. Liu and Chandrasekar (2000) describe a fuzzy logic system which allows for decisions to be made based on overlapping and "noise contaminated" data.

Fuzzy logic is a process of four steps: 1) fuzzification, 2) inference, 3) aggregation, and 4) defuzzification. During fuzzification, the measured value is converted into a fuzzy set with a truth value for each hydrometeor type, which ranges from 0 to 1. One specific input value can belong to several fuzzy sets with different truth values. A membership beta function describes the relationship of the measured value to the fuzzy set. The inference step combines the truth value for each variable to determine a net truth value for each hydrometeor type. The maximum truth value is determined during the aggregation phase, and defuzzification refers to the conversion of that truth value into a single hydrometeor type that is best described by the fuzzy output set (Liu and Chandrasekar, 2000).

Zrnić *et al.* (2001) note that since some variables may be more reliable than others, a weighting scheme can be employed to curb the effects of bogus and noisy data. For example, since L_{dr} tends to be noisy, it is weighted less than reflectivity. The fuzzy logic hydrometeor identification algorithm used in this study uses a hybrid weighted sum method given by Eqn. 2.23.

$$u_j = \sum_{i=1}^{n} W_{i,j} * \beta_{i,j}(x_i) \tag{2.23}$$

where u is the truth value for hydrometeor type j, W is the weighting function for each radar variable (subscript i) and hydrometeor type (j), β is the membership beta function, or truth value, for the radar variable and hydrometeor set.

Vivekanandan *et al.* (1999) suggest that the fuzzy logic method for bulk identification of hydrometeors is preferable in real-time to statistical decision trees or neural networks because only simple linear algebraic operations are involved, making the algorithm quick. Additionally, the effects of measurement error do not significantly impact the outcome due to the soft boundaries of the membership beta functions and the weighting functions.

The present study uses one dimensional membership beta functions for eleven hydrometeor types: drizzle (Drz), rain (R), wet snow (WS), dry snow (DS), low density (or 'dry') graupel (DG), high density (or 'wet') graupel (WG), small hail (SH), small hail mixed with rain (Sh+r), large hail (LH), large hail mixed with rain (Lh+r), and vertical ice (VI). It also allows for an unclassified category (UC) in the instance when none of the hydrometeor types score a significant truth value. The input variables are Z_h, Z_{dr}, K_{dp}, L_{dr}, $\rho_{hv}(0)$, and temperature. The membership beta functions are shown in Appendix A Figs. A.1-A.11. The boundaries and shapes of these functions are based on Straka *et al.* (2000), Zrnić *et al.* (2001), Carey and Rutledge (1998), Liu and Chandrasekar (2000), Lopez and Aubagnac (1997), and Lim (2001), and have been adapted to their current form based on input and observations from several sources in the community (K. Wiens, personal communication, 2004). The thresholds determined in the above studies are listed in Appendix A, Tables A1.-A.11.

2.4.2 *Rainfall Estimation*

The rain rate, R, at a given point from the radar can be related to the reflectivity, Z, by the general equation:

$$Z = aR^b \tag{2.24}$$

where a and b are constants. The constants a and b are functions of the drop size distribution (DSD). Since rain rate is proportional to the 3.67^{th} moment of DSD and reflectivity to the 6^{th} moment of DSD, it is evident that Z-R relationships are very sensitive to the variability of DSD. Battan (1979) shows a table of Z-R relationships calculated in different types of precipitation in different locations, all with slightly different parameters for the DSD. The Z-R relationship used by the National Weather Service is:

$$Z = 300R^{1.4}. \quad [\mathrm{R\ mm\ h^{-1}}] \quad [\mathrm{Z\ mm^6\ m^{-3}}] \quad (2.25)$$

Standard Z-R relationships are also problematic due to their sensitivity to calibration, attenuation, beam-blockage, and the presence of hail. The National Weather Service truncates Z at 53 dBZ in order to eliminate contamination from hail. This limits the rain rates that can be calculated by the WSR-88D radars.

Although there are techniques for determining the DSD for specific storms after the fact, real-time calculations must make assumptions about the typical DSDs in a given area. Petersen *et al.* (1999) illustrated the limitations of always using the same DSD and Z-R relationship. They showed that the storm that produced nearly 10" of rain in a 6 hr period during the Fort Collins flash flood of 1997 was more accurately characterized by tropical rather than mid-latitude DSDs. The assumption of a mid-latitude DSD led to a 100% underestimation of the total rainfall by the Denver WSR-88D. This is a problem of particular interest to the National Weather Service, who are responsible for flash flood detection and forecasting.

Techniques have been developed for rain rate and rainfall estimation using polarimetric information. Specifically, the specific differential phase is proportional to the amount of rainwater content and the mass-weighted mean diameter and can therefore be used to differentiate between the liquid and ice portions of a radar volume. A relationship between R and K_{dp} is given by Bringi and Chandrasekar (2001):

$$R(K_{dp}) = 129\left(\frac{K_{dp}}{f}\right)^{b_2} \qquad [\text{mm h}^{-1}] \qquad (2.26)$$

where f is the frequency of the radar in GHz. Assuming the Beard-Chuang equilibrium shape model and the CSU-CHILL frequency, the equation becomes

$$R(K_{dp}) = 53.8(K_{dp})^{0.85}. \qquad [\text{mm h}^{-1}] \qquad (2.27)$$

The differential reflectivity can also be used to account for the particle sizes present in a volume, and can be used along with reflectivity to find a rain rate using Eqn. 2.28 from Bringi and Chandrasekar (2001).

$$R(Z_h, Z_{dr}) = c_1 Z_h^{a_1} 10^{0.1 b_1 Z_{dr}}. \qquad [\text{mm h}^{-1}] \qquad (2.28)$$

In the case of the CSU-CHILL radar wavelength the equation becomes:

$$R(Z_h, Z_{dr}) = 6.70 \times 10^{-3} Z_h^{0.927} 10^{(-0.3433 * Z_{dr})} \qquad [\text{mm h}^{-1}] \qquad (2.29)$$

K_{dp} and Z_{dr} can be used together to calculate a rain rate in the form of Eqn. 2.30:

$$R(K_{dp}, Z_{dr}) = c K_{dp}^{a} 10^{(0.1 b_1 Z_{dr})}. \qquad [\text{mm h}^{-1}] \qquad (2.30)$$

Adding in the constants for the CSU-CHILL radar wavelength it becomes:

$$R(K_{dp}, Z_{dr}) = 87.6 K_{dp}^{0.934} 10^{(-0.169 * Z_{dr})}. \qquad [\text{mm h}^{-1}] \qquad (2.31)$$

Although K_{dp} is less sensitive to DSD, power calibration, clutter, attenuation and hail, it tends to be noisy, especially when reflectivity values are less than 30dBZ, and has reduced spatial resolution. It is therefore not appropriate in every situation. Z_{dr}, on the other hand, has better spatial resolution, but is sensitive to power calibration, hail contamination, attenuation, and clutter. Therefore, it is also not applicable in every situation.

Following the technique described in Chandrasekar *et al.* (1993), Cifelli *et al.* (2003) have developed a 'blended algorithm' which uses a decision tree to determine the best estimate of rainfall based on measurement thresholds. The flow chart showing the decision tree for this algorithm is shown in Fig. 2.7.

The ice fraction is determined by using Z_{dp} and the rain line determined by Carey and Rutledge (1996). If the ice fraction is greater than 0.1 the algorithm tries to use K_{dp} methods to determine rain rate since it is insensitive to the amount of ice in a volume. If the reflectivity is less than 38 dBZ and K_{dp} is smaller than 0.2, it is possible that K_{dp} will be noisy, so a simple Z-R relation is used, but using only the reflectivity due to rain as calculated from Z_{dp}. If the ice fraction is sufficiently small such that the volume is not contaminated by hail, the algorithm tries to use $R(K_{dp}, Z_{dr})$ relations. Again K_{dp}, Z_{dr}, and Z_h are thresholded to limit the use of possible bogus data.

Although this technique is still subject to assumptions about Z_{dp}-Z relationships, studies by Cifelli *et al.* (2003) and Petersen et al. (1999) have demonstrated that this method for calculating the rain rate, and subsequently the total cumulative rainfall, does at least as well as, if not better than, standard Z-R relationships. Additionally they have verified the output against rain gauge measurements.

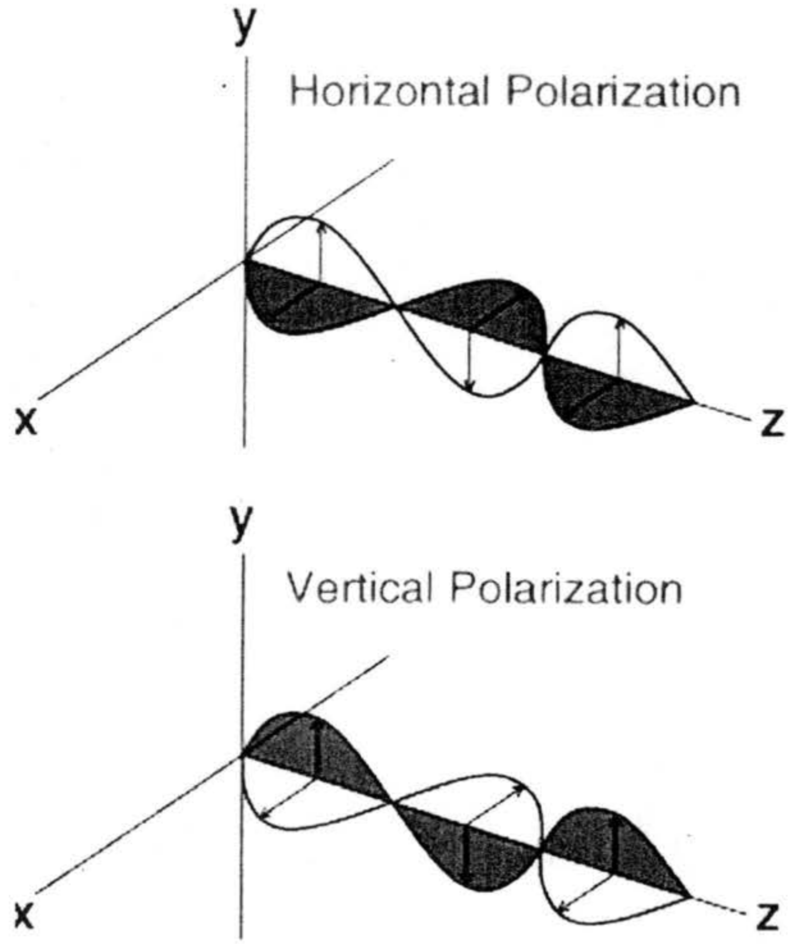

Figure 2.1: Illustration of horizontal (top) and vertical (bottom) polarized electromagnetic waves. The shaded regions represent the oscillating electric fields of the wave as it propagates along the z-axis. (URL: http://cimms.ou.edu/~schuur/radar.html, 2004).

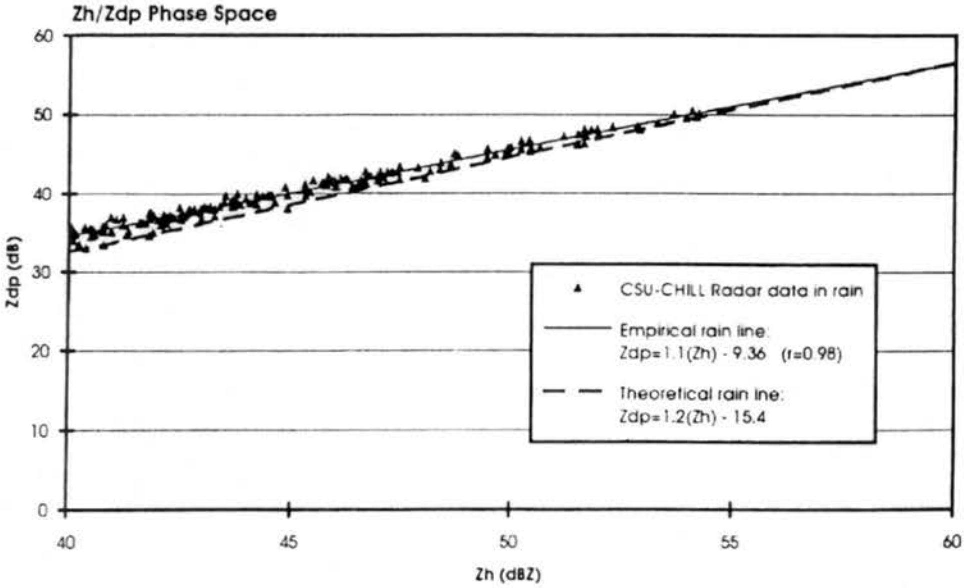

Figure 2.2: Scatter plot of Z_{dp} vs. Z_h for CSU-CHILL data in a rain event from 21 May 1993. The solid line is the least-squares best fit line to the radar data. The dashed line depicts the best fit for theoretical data from Golestani et al. (1989) (from Carey and Rutledge, 1996).

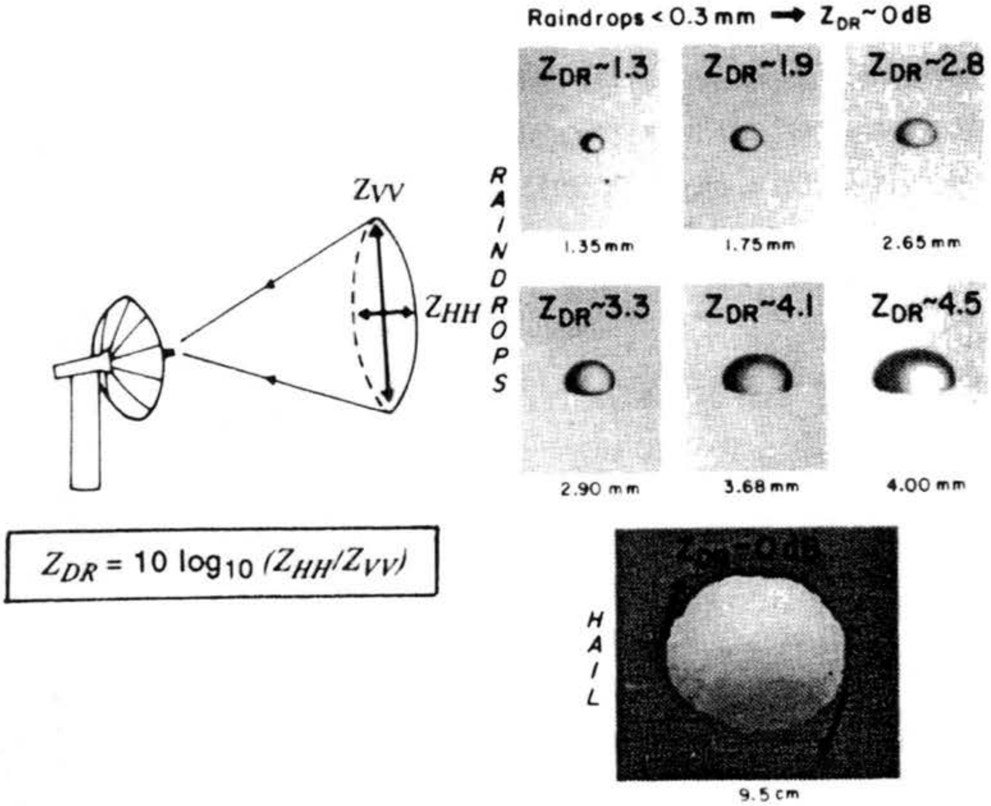

Figure 2.3: Z_{dr} values for different particle sizes. From Houze (1993).

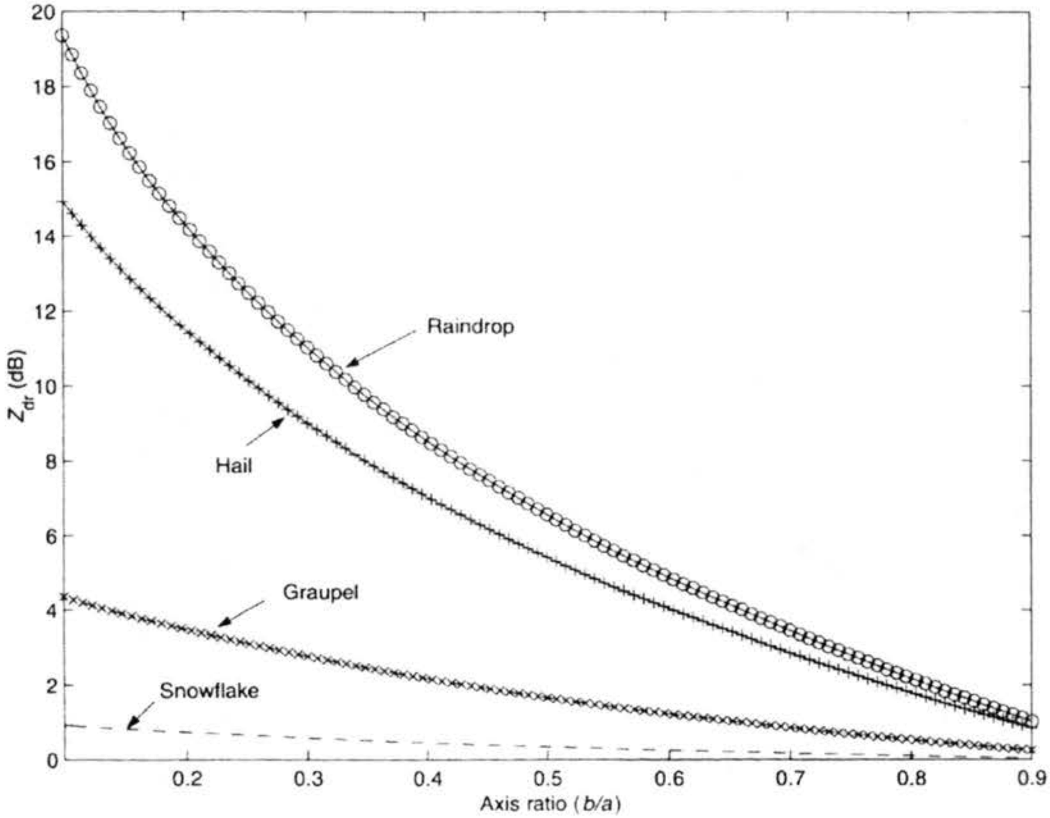

Figure 2.4: Differential reflectivity, Z_{dr}, vs. axis ratio, b/a, for a given particle type (density) (from Bringi and Chandrasekar, 2001).

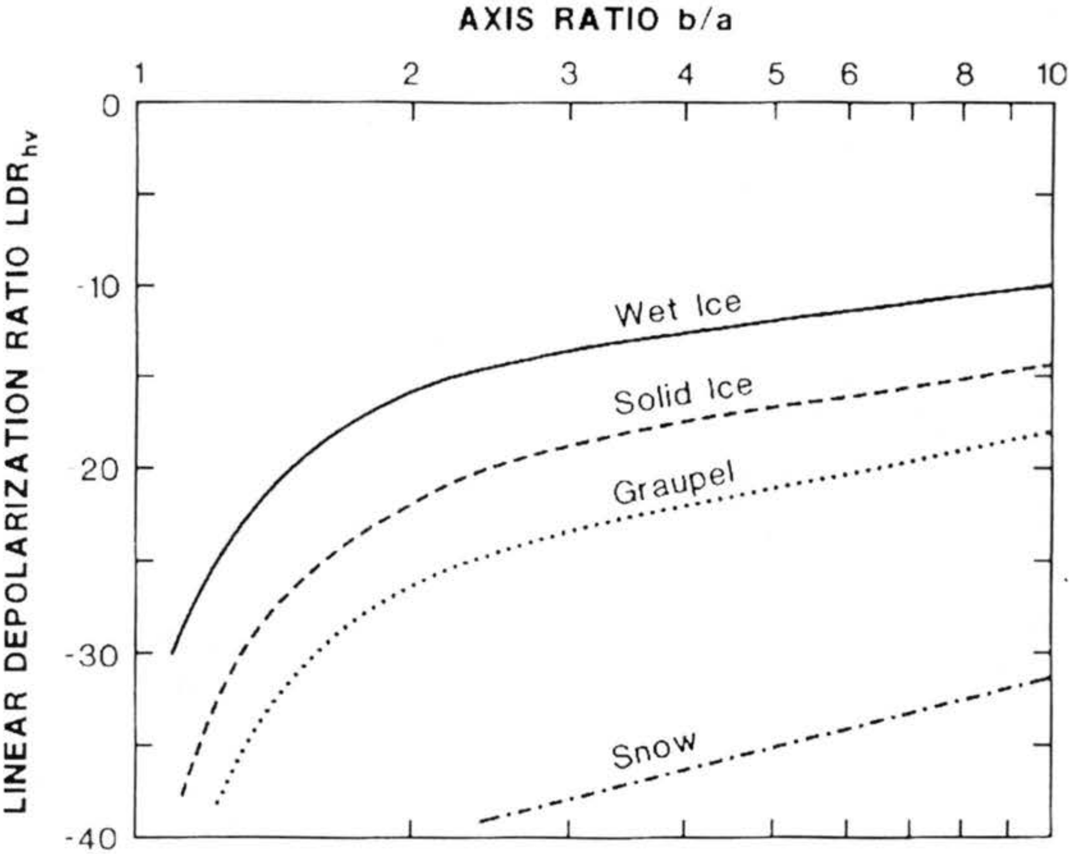

Figure 2.5: Linear depolarization ratio, L_{dr}, as a function of axis ratio, b/a, for several randomly tumbling oblate spheroids (from Doviak and Zrnić, 1993).

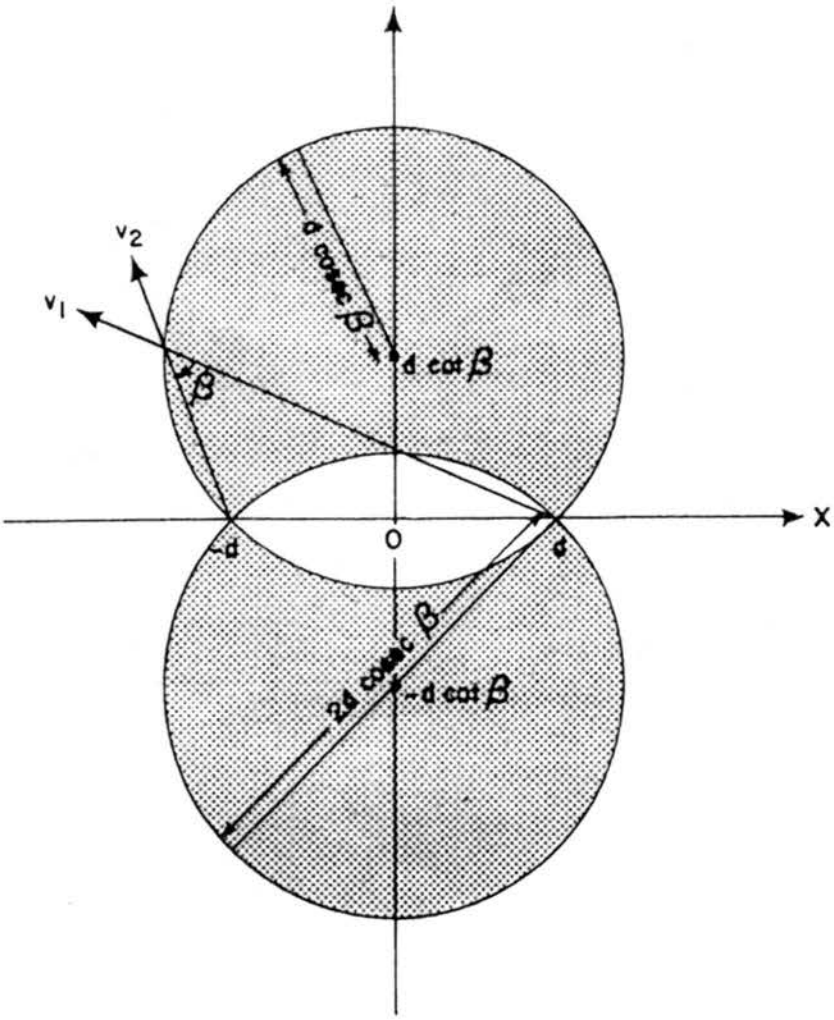

Figure 2.6: Dual-Doppler area in which the beam-crossing angle is between β and π−β. Radars are located at (+/-d, 0) (from Davies-Jones, 1979).

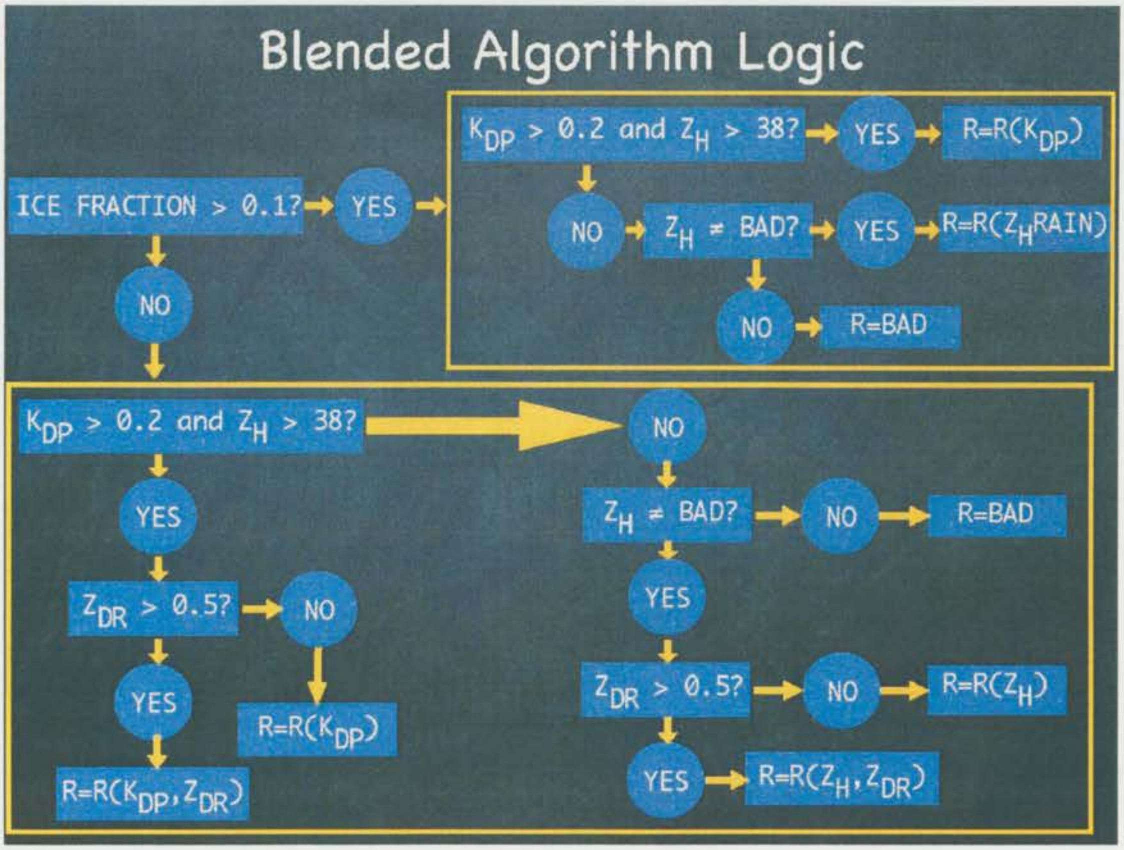

Figure 2.7: Decision tree for rain rate estimation using the CSU-CHILL blended algorithm (from Cifelli et al., 2003).

Table 2.1: Dual-Doppler network specifications assuming a minimum beam-crossing angle of 30°.

Radar pair	**Baseline**	**Farthest Point**	**Resolution at the farthest point**	**30° coverage area**
KFTG-CHILL	73.736 km	147.48 km	2.5 km	53,429 km^2
CHILL-PAWNEE	47.677 km	95.35 km	1.6 km	22,338 km^2
KCYS-PAWNEE	32.151 km	64.30 km	1.1 km	10,158 km^2

CHAPTER 3

Data and Algorithm Description

3.1 Data

Level II archive formatted data from the National Weather Service WSR-88D radars was retrieved using Unidata's Local Data Manager (LDM) in association with the Collaborative Radar Acquisition Field Test (CRAFT). The LDM is a collection of cooperating systems which select, capture, manage, and distribute meteorological data products in real-time (http://my.unidata.ucar.edu/content/software/ldm/archive). The CRAFT network is a collaboration between the Center for Analysis and Prediction of Storms (CAPS) program at the University of Oklahoma, Oklahoma State Regents for Higher Education, Unidata, and the University of Washington in order to gather NEXRAD data in real-time. Though the data are available almost immediately after a volume scan is completed, there are latency issues with the large size of the files and the number of nodes between the source of the data and the destination computer. At present it takes several minutes to download each file. As will be discussed in section 4.1, the LDM is the bottleneck in getting real-time dual-Doppler winds at the CHILL radar facility, since by the time a file is completely downloaded at the destination computer it is approximately 9-13 minutes after the volume scan started, depending on the VCP of the radar.

Sounding data for Denver (KDNR) is acquired as a text file from the Upper Air Data page on Unisys' weather webpage (http://weather.unisys.com/upper_air). Soundings are obtained twice per day, once at 0 UTC and once at 12 UTC. The file is downloaded to the computer workstation at the CSU-CHILL radar facility as soon as it is available from the website, which can be over an hour after the launch time. In the event that data are not available from Unisys, sounding data from the University of Wyoming is used (http://weather.uwyo.edu/upperair/sounding.html).

During the design and testing phase, the PAWNEE radar was unavailable for real-time data collection. It was not operational due to technical problems; additionally there are inadequate resources to transfer the data in real-time to the CHILL radar facility. However, this problem is being reviewed at the time of this writing and hopefully a method of rapid file transfer will be implemented in the next year. For the purposes of the software algorithm development, archive data from the PAWNEE radar was used in lieu of real-time data. When PAWNEE is operational again and a method of data transfer is in place, data should be able to be fully integrated with the algorithm.

Data from the CSU-CHILL radar were available immediately after the completion of a volume scan. Data are in the CHILL raw field data format.

3.2 Data Processing

3.2.1 Linux Workstation

A new Linux workstation was purchased solely for the purpose of running the analysis program, displaying the output, and storing the associated data. The computer is a Hewlett-Packard with dual 2.8 GHzXeon processors. A dual-processor system was selected in order to expedite the processing of data while simultaneously displaying interactive data. Three 250 GB SATA hard disks were purchased to accommodate the nearly 400 MB per hour of data that is generated from all four radars in precipitation-type modes. The workstation has 3 GB of 800 MHz DDR RAM to also increase the performance. This workstation will reside at the CSU-CHILL radar facility as a dedicated machine to analyze, display, and store real-time data from the four radars described in this thesis.

3.2.2 Processing raw files

Files are first converted to Universal Format (UF), which organizes data in the natural coordinates of the radar (azimuth angle relative to north, elevation angle, and slant range). The WSR-88D level II files are converted to UF using the xltrsii data translator available as part of the SOLOii package developed at the National Center for Atmospheric Research (NCAR). This translator accounts for the different gate spacing for the reflectivity and radial velocity data due to the separate surveillance and Doppler scans at the lowest elevation angles. This is done by reinterpolating the velocity data such that the gate size is the same as the reflectivity gate spacing and storing them into the same sweep structure. This single sweep structure is necessary for use with the NCAR REORDER software package. Level II archive data has already been through thresholding and cleanup steps to eliminate clutter and second-trip echo.

CHILL files are first converted to universal format using a translator written by Dave Brunkow, senior engineer at the CSU-CHILL facility. The polarimetric capabilities of the CHILL radar allow for additional editing of the data to remove contamination from anomalous propagation (AP). As described in Ryzhkov and Zrnić (1998) (henceforth referred to as RZ98), the correlation coefficient can be used to distinguish between ground clutter and meteorological targets. Additionally, the standard deviation of the differential phase can be used to filter out non-meteorological echo. Anomalous propagation is especially a problem when calculating rain rates and rainfall accumulations. Bringi and Chandrasekar (2001) express the variance of the differential phase as Eqn. 3.1:

$$\mathrm{var}(\hat{\Psi}_{dp}) = \frac{1}{4}[\mathrm{var}(\Psi_1) + \mathrm{var}(\Psi_2) - 2\,\mathrm{cov}(\Psi_1, \Psi_2)] \tag{3.1}$$

where

$$\mathrm{var}(\Psi_1) = \mathrm{var}(\Psi_2) = \frac{1 - |\rho[1]|^2 |\rho_{hh,vv}[0]|^2}{2N^2 |\rho[1]|^2 |\rho_{hh,vv}[0]|^2} \sum_{n=-(N-1)}^{N-1} (N - |n|)\rho[2n]^2 \tag{3.2}$$

and

$$\mathrm{cov}(\Psi_1, \Psi_2) = \frac{|\rho_{hh,vv}[0]|^2 - |\rho[1]^2|^2}{2N^2 |\rho[1]|^2 |\rho_{hh,vv}[0]|^2} \sum_{n=-(N-1)}^{N-1} (N - |n|)\rho[2n+1]^2 . \tag{3.3}$$

Substituting Eqns. 3.2 and 3.3 into Eqn. 3.1, it is clear that the standard deviation of the phase is closely related to the correlation coefficient as well as the number of samples. RZ98 determined the thresholds for the Cimarron polarimetric radar should be set to 0.7 for ρ_{hv} and 10-12° for SD(ϕ_{dp}). Although they found good results for the case they studied, they recognize that these thresholds may remove large hail and bright band signals because in these situations ρ_{hv} can fall below 0.7, and the standard deviation of the phase can be higher than 12°.

A sensitivity study was performed to determine the optimal thresholds for the CSU-CHILL radar. Two cases of intense rainfall near the mountains were chosen as the case studies; the first is from a rain event that occurred on 27 August 2002 between 2028 UTC and 0324 UTC on 28 August 2002, and the second is from an event on 18 June 2003 between 0000-0643 UTC. The data were processed using varying thresholds for both the standard deviation of the phase and the correlation coefficient. Values of $SD(\phi_{dp})$ were chosen to be 13°, 18° and 36°, where 36° essentially corresponds to no filter. Four values for ρ_{hv} were chosen to be 0.75, 0.85, 0.8 and 0.9. These values were selected based on standard observed ranges from the CSU-CHILL radar. In order to isolate the effects of the desired variable, only one threshold was allowed to change in each run. For example, ρ_{hv} was held constant at 0.8 while the $SD(\phi_{dp})$ was allowed to vary between 13°, 18° and 36°, and $SD(\phi_{dp})$ was held at 18° while ρ_{hv} was changed. The results were first analyzed by looking at the fraction of total precipitation and fraction of ice to determine if a significant amount of echo was being eliminated. These results are plotted in Figs. 3.1 (28 August 2002) and 3.2 (18 June 2003). In comparing the thresholds, it is obvious that increasing the ρ_{hv} threshold decreases the amount of echo retained in a given volume scan. Lowering the $SD(\phi_{dp})$ threshold to 13° decreases the fraction of ice in the grid volume as well as reduces the fraction of ice relative to the amount of precipitation in the grid volume.

The data were also run through the hydrometeor identification algorithm, which was organized into number of counts for each particle type. These plots are shown in Figs. 3.3 and 3.4 for 28 August 2002 and 18 June 2003, respectively. In general, turning off the $SD(\phi_{dp})$ filter (36°) resulted in noisy classification of the particle types. This is particularly evident in the large hail, wet snow, small hail and rain categories. Additionally, the low SD(ϕ_{dp}) threshold of 13° tended to significantly reduce the number of counts in all hail and graupel types. All the ρ_{hv} runs tended to group together for the most part, with the exception of drizzle, rain, dry graupel and dry snow. A high ρ_{hv} filter removed large numbers of drizzle and dry snow points, while at the same time increasing the number of dry graupel and rain points.

Lastly, the gridded volumes were run through the rainfall algorithm to plot the total accumulated rainfall. These results are illustrated in Figs. 3.5 and 3.6. From these figures it is clear that the standard deviation of the phase suppresses some of the clutter caused by the mountains (from y=-50 to y=-110, and x=-60 to x=-30 in the 18 June 2003 case, Fig. 3.6). The effect of ρ_{hv} is much less apparent, but some of the miscellaneous patches outside the main echo are removed by increasing the ρ_{hv} threshold (28 August 2002 case, Fig. 3.5).

There are several conclusions that can be drawn from the sensitivity study. In general terms, although the two variables are related, the correlation coefficient seems to have less of an impact on the clutter removal than changing the standard deviation of the phase. RZ98 found that changing ρ_{hv} by 0.1 resulted in a change in ϕ_{dp} by almost 3 times. For the most part, the ρ_{hv} values of 0.7, 0.8, 0.85 and 0.9 produced similar results, though setting the threshold too high at 0.9 seems to eliminate some precipitation, in the form of drizzle. Changing the standard deviation of ϕ_{dp} yields more noticeable results. When the threshold is high, too much return from non-meteorological echo gets though, and the number of particles identified as hail is artificially inflated. Imposing a stricter threshold of 13° leads to depressed counts of hail, and consequently the suppression of real hail signals. However, there are many non-linear effects resulting from the coupling of the variables in the hydrometeor identification algorithm. The thresholds of ρ_{hv}=0.8 and SD(ϕ_{dp})=18° were decided upon to compromise between removing clutter and eliminating real echo, such as hail and drizzle.

As a demonstration of these threshold values, Fig. 3.7 shows the reflectivity, differential reflectivity (labeled 'DR'), K_{dp} (labeled 'KD') and linear depolarization ratio (labeled 'LD') for one time during the 28 August 2002 case without any polarimetric thresholds imposed on the data. Figure 3.8 shows the same time and variables with the ρ_{hv}=0.8 and SD(ϕ_{dp})=18° thresholds. In this example, the clutter between the radar and the storm was greatly reduced. It should be noted, however, that this is still a subjective method of studying the influences of various thresholds.

3.2.3 Gridding to Cartesian Coordinates

The data were gridded using the REORDER software package developed at NCAR. The software uses a customized grid input file which allows the user to chose the grid definitions based on the storm. However, all data were interpolated to the Cartesian grid using the Cressman weighting scheme (Cressman, 1959). Users can either specify a variable or fixed radius of influence, depending on the location of the storm. A variable radius uses a delta-azimuth and delta-elevation rather than the fixed delta-x, delta-y and delta-z radius of influence, but it can cause excessive smoothing at high altitudes, especially when the storm is far from the radar. Additionally, the volumes are gridded in altitude coordinates above mean sea level (MSL).

3.2.4 Dual-Doppler Synthesis

Determining the storm advection is an integral part of performing a dual-Doppler synthesis, because the storm can evolve even throughout the duration of a volume scan. Therefore, it is important to advect the volume scans to a common time in order to perform the dual-Doppler synthesis. In order to minimize the advection at any one grid point (and the error that could accumulate from that), two volumes are selected for dual-Doppler synthesis only if their volume start times are within three minutes of one another.

Determining the advection direction and speed is a much trickier task. In post analysis, a radar scientist can manually ascertain the speed and direction by looping through volumes throughout the lifetime of an individual storm. In real-time processing, this information must be gathered quickly and for entire grid-domains. This algorithm uses a local sounding to find the 700 mb 'steering winds'. If a sounding is not available or the scientist notices the mean flow is not represented by the 700 mb winds, the user can manually set default values for the wind speed and direction. Errors in the derived wind field may be introduced when the 700 mb winds or user specified advection parameters are not representative of the true storm motion.

The radial velocities were first locally unfolded using the UNFOLD option in REORDER, then globally unfolded using the NCAR Custom Editing and Display of Reduced Information in Cartesian space (CEDRIC) program (Mohr and Miller, 1983). The two radial velocities are then synthesized using CEDRIC to determine the u, v, and w components of the wind field. As discussed in section 2.3.2, the solution of the 3D wind field requires knowledge of the particle fall speed, V_t. Standard V_t-Z relationships are used above and below the melting level, which is either input by the user or determined from the local sounding. The vertical wind is determined using a downward integration method.

The dual-Doppler winds are greatly influenced by the scanning strategy of the WSR-88D radars. When the 88Ds are in precipitation mode (see Figs. 1.6 and 1.7), the high elevation angles are sparse, leading to large gaps at high altitudes, and not many winds result from the synthesis.

3.3 Algorithm

Due to its string manipulation capabilities, Perl was chosen as the language for the processing algorithm. The software can be used in two modes, real-time or post-processing. In real-time mode, it looks for new files to process and runs through all the processing described in section 3.2. In post-processing mode the user can choose one or more of the processes to run. A simple flow-chart diagram of the real-time algorithm processing is illustrated in Fig. 3.9.

It was readily apparent that CSU-CHILL files would be the quickest available, so the algorithm looks for and processes those first. If a CHILL file is available, the file type is determined. Then it is run through the program to eliminate clutter via thresholding of the polarimetric variables ρ_{hv} and $SD(\phi_{dp})$ and calculate K_{dp}. Once this is complete, the volume is gridded to Cartesian coordinates using REORDER. The program then determines if a sounding matches the grid volume time within 12 hours, and if so, uses the sounding temperature profile in the hydrometeor identification. If no sounding is available, the user can specify a melting level and the generated temperature profile will be fixed at 10 °C below the melting level, 0 °C at the melting level, and –10°C above the melting level. The CSU blended rainfall algorithm is run to find the rain rate, and if the newest volume time is within 2 hours of the previous volume time, it is added to the accumulation. If not, then a new rainfall accumulation is started. The final output is in netCDF format, which is sent to the visualization program (discussed in section 3.4) as soon as the processing is complete.

The algorithm then proceeds through the other three radars, checking for new files. If a new files exists and it is not in universal format (UF), it is converted to UF via the translation software. If it is a WSR-88D file, a check is performed to determine if the radar was in precipitation mode or clear-air mode. If it was in clear-air mode, the file is archived but nothing else is done to it. If it is in precipitation mode, then it is matched against processed files for dual-Doppler pairs. If a matching file for the dual-Doppler pair exists within 3 minutes, the algorithm checks against sounding files to determine if the advection can be extracted from the sounding or if default values should be used. If a sounding exists within 12 hours, the 700 mb winds are used for the advection speed and direction; if not user input values are used. The matching files are gridded to a common grid using REORDER, then the velocities are globally unfolded using CEDRIC, and finally the 3D wind field is derived from the two radial velocities using CEDRIC. The final step is to run a comparison rain rate and rainfall algorithm. Once this process is complete, the files are sent to the visualization software and archived in the appropriate directory. If a dual-Doppler synthesis is not possible, the radar volume is gridded to Cartesian coordinates and run through the rainfall and rain rate algorithms before being sent to the visualization software. In addition to the visualization software, images can be published to the web for display in real-time. In real-time mode, this process is repeated after waiting 30 seconds.

3.4 Display Tool

Research Systems Inc. (RSI)'s IDL was chosen as the programming language for the visualization software. The visualization software can operate in real-time mode where it continually looks for new files. The display window consists of four panels which can be configured by the user. The user can choose the radar, variable, and height in each panel as well as activate overlays such as county lines, roads and dual-Doppler winds and multiple contour variables (Fig. 3.10). The panel configuration can be changed to include vertical cross sections (Fig. 3.11) and zoom in on a storm (Fig. 3.12). Additionally, the user can save images for archival or post-processing.

Although the display offers similar radar products to software packages that have been available in the past, it is unique in several ways. First of all, the user can display data from multiple radars simultaneously, as well as determine the grid size, resolution, and origin for the processing of the data. This functionality could be useful in situations where one specific storm is the focus of the real-time studies. A high resolution grid domain restricted around the storm could provide detailed information about that specific cell without requiring the processing time involved with gridding the entire radar domain. However, since the original files are archived, scientists can process them at a future time on a different grid. Secondly, the display software allows the user the flexibility to change the window configuration, display data from several different radars with contouring and overlays, and zoom in and out of the grid. Users can also change the color scale and display range for each variable. The print function permits the user to save particularly interesting images for analysis at a later time. Finally, as will be discussed in the next chapter, real-time processing takes less time (13-15 minutes) than the 15-20 minutes described by Chong et al. (2000) for a finer resolution grid (141 km x 141 km x 11 km at 1 km x 1 km grid resolution compared to Chong et al. (2000) 147 km x 147 km x 11 km grid with 3 km x 3 km grid resolution). The flexibility available in this algorithm results in a unique tool for the processing and display of data from multiple Doppler radars.

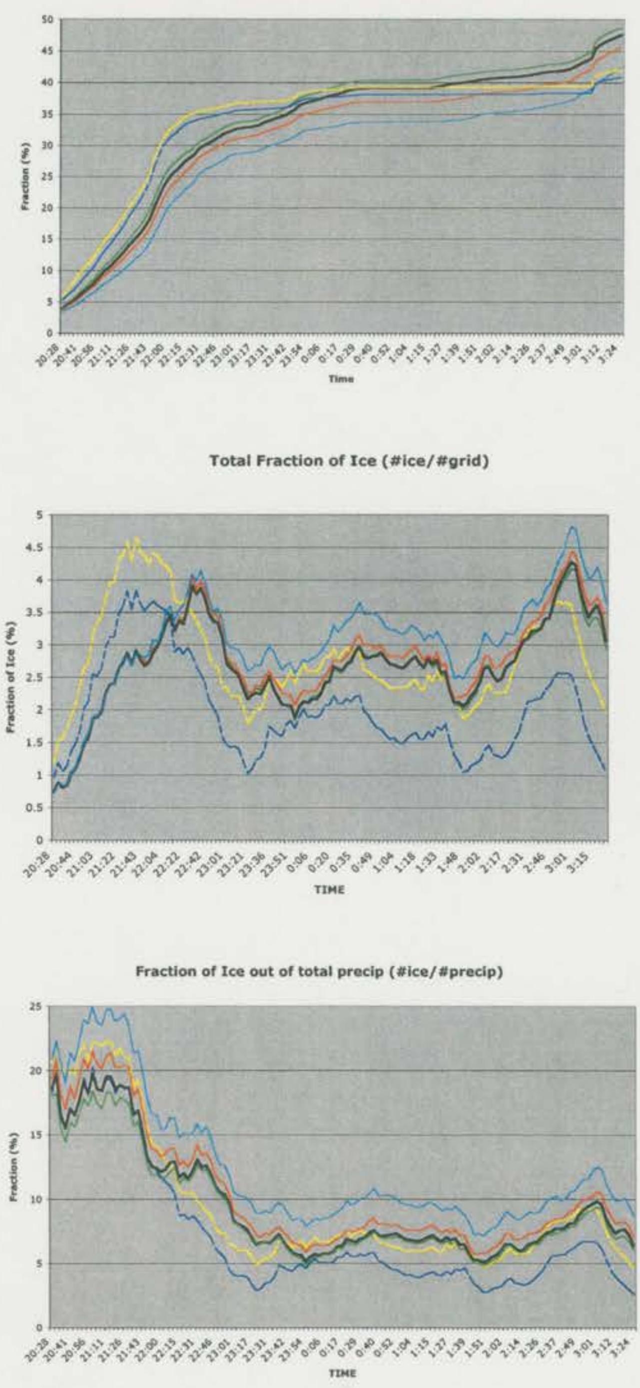

Figure 3.1: Results of the sensitivity study for 28 August, 2002. The thick black line indicates the 'control' run in which ρ_{hv} =0.8 and SD(ϕ_{dp})=18°. The dashed lines represent runs in which ρ_{hv} was held at 0.8 and SD(ϕ_{dp}) was changed to 36° (yellow) and 13° (dark blue). Solid lines are runs where SD(ϕ_{dp}) was left at 18° and ρ_{hv} was changed to 0.75 (green), 0.85 (red), and 0.9 (light blue).

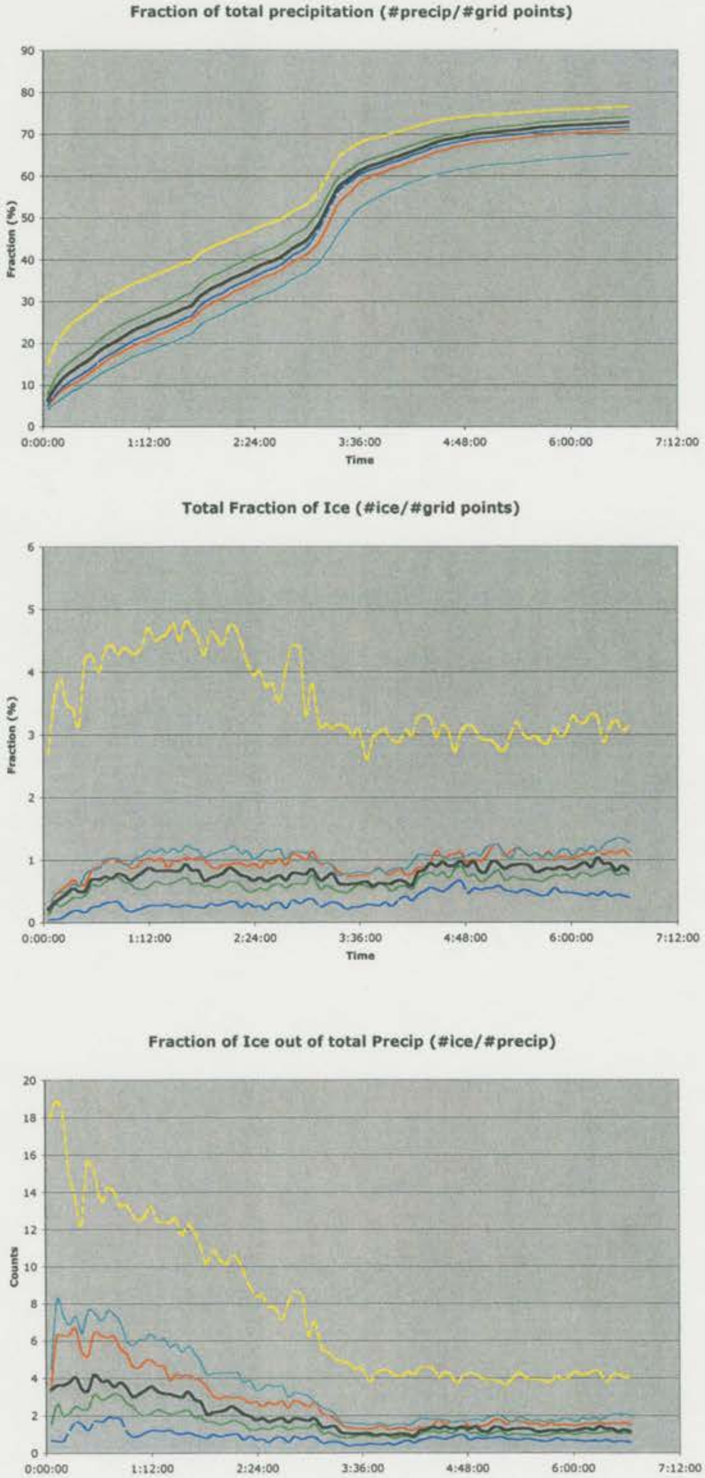

Figure 3.2: Same as Fig. 3.1, except results from 18 June 2003.

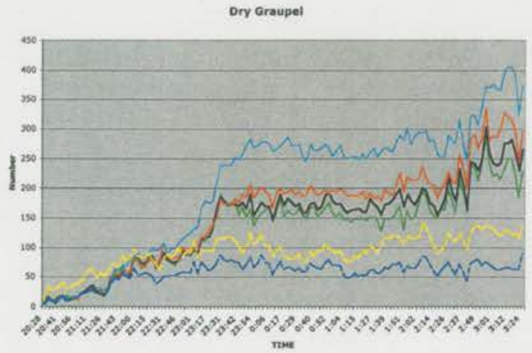
Dry Graupel
Number
TIME

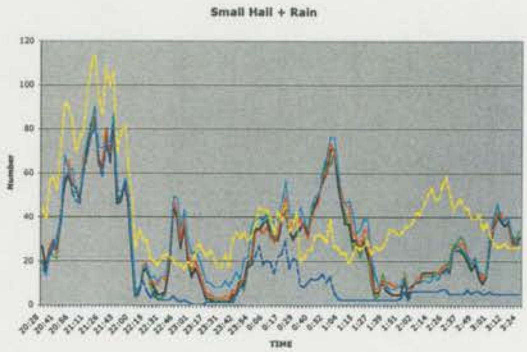
Small Hail + Rain
Number
TIME


Wet Graupel
Number
TIME

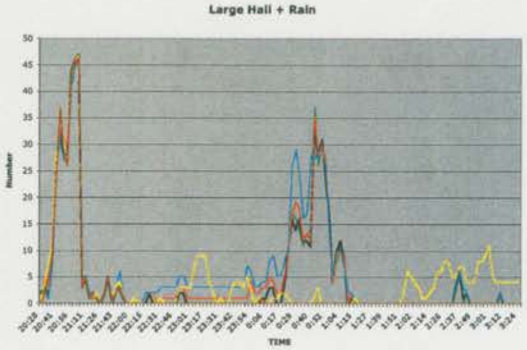
Large Hail + Rain
Number
TIME

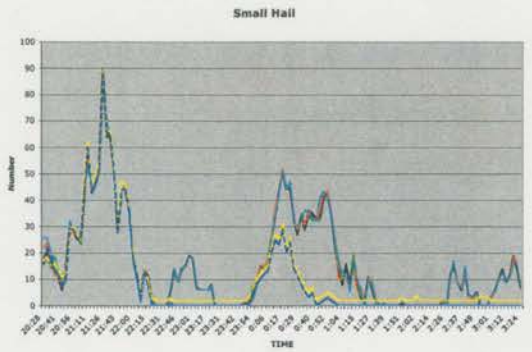
Small Hail
Number
TIME

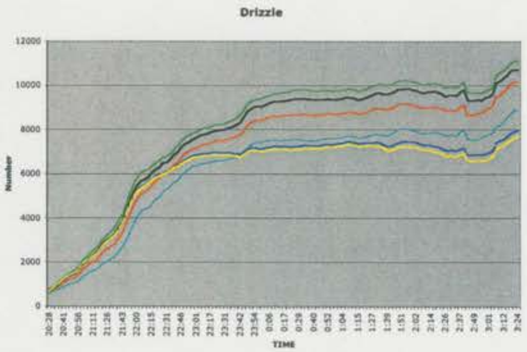
Drizzle
Number
TIME

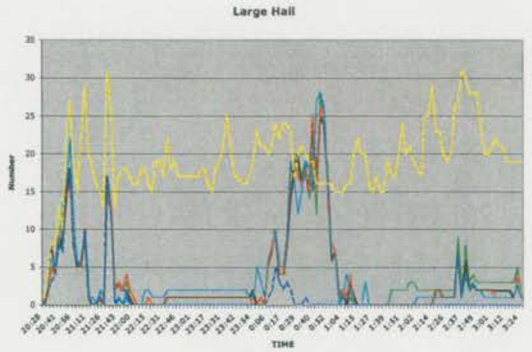
Large Hail
Number
TIME

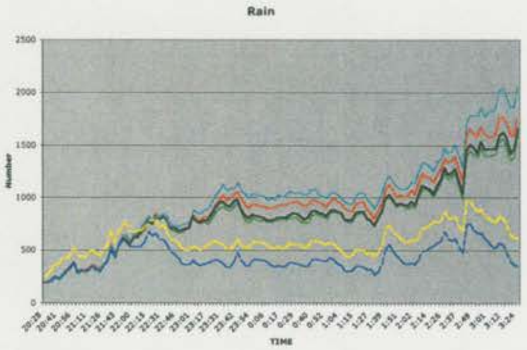
Rain
Number
TIME

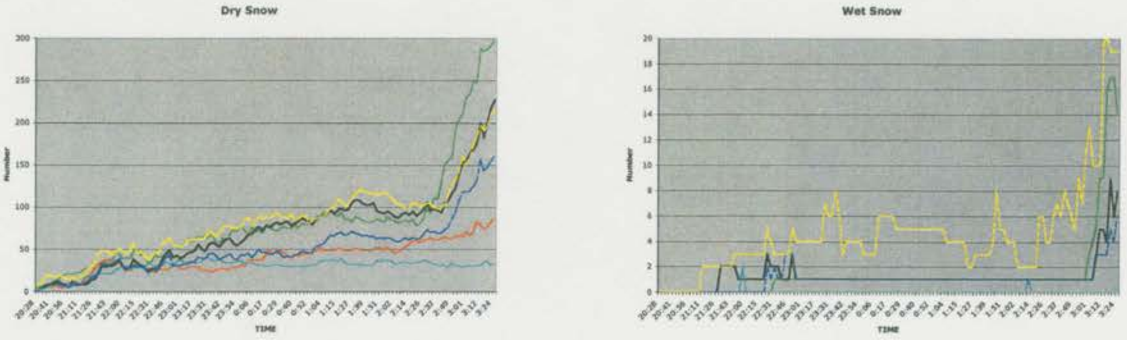

Figure 3.3. Number of counts for each hydrometeor classification type for the sensitivity study on 28 August 2002. The thick black line indicates the 'control' run in which ρ_{hv} =0.8 and SD(ϕ_{dp})=18°. The dashed lines represent runs in which ρ_{hv} was held at 0.8 and SD(ϕ_{dp}) was changed to 36° (yellow) and 13° (dark blue). Solid lines are runs where SD(ϕ_{dp}) was left at 18° and ρ_{hv} was changed to 0.75 (green), 0.85 (red), and 0.9 (light blue).

Dry Graupel

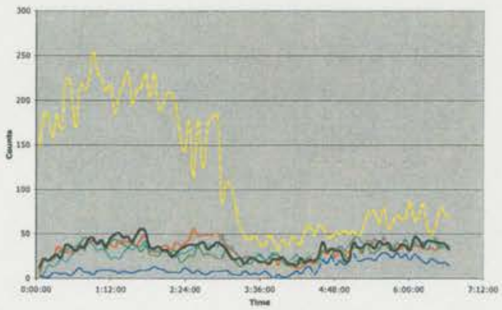

Wet Graupel

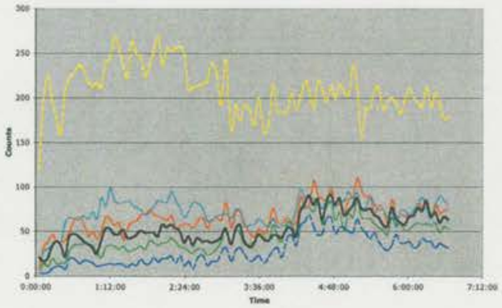

Small Hail

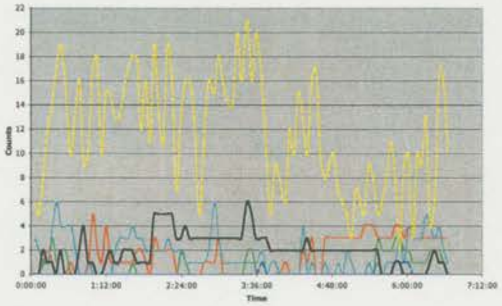

Large Hail

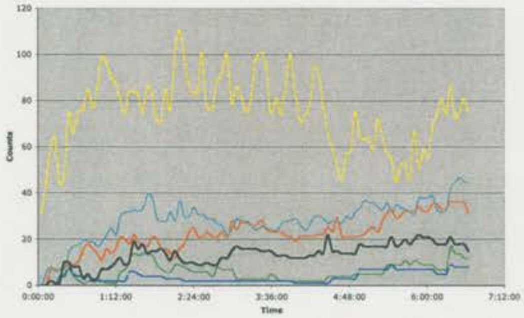

Small Hail + Rain

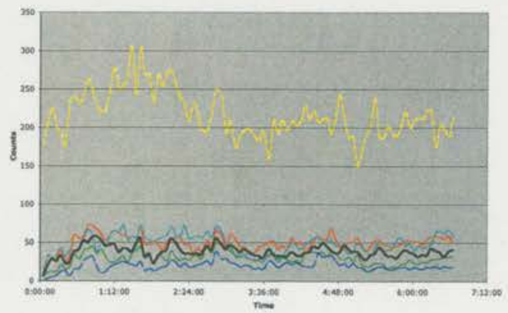

Large Hail + Rain

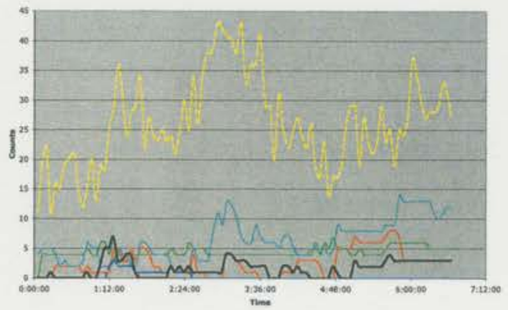

Drizzle

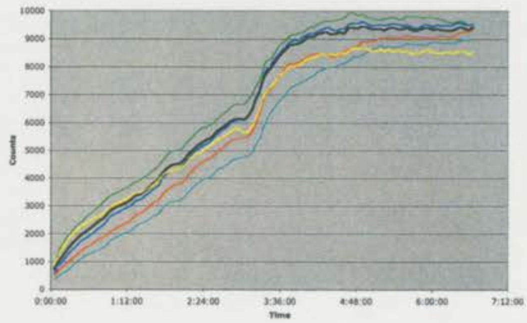

Rain

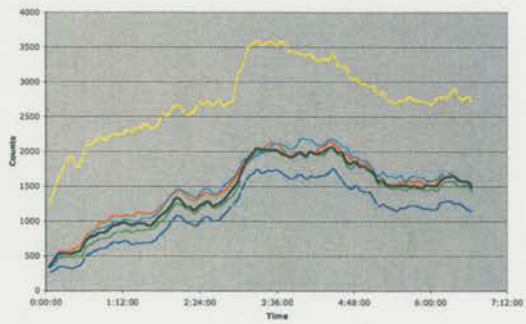

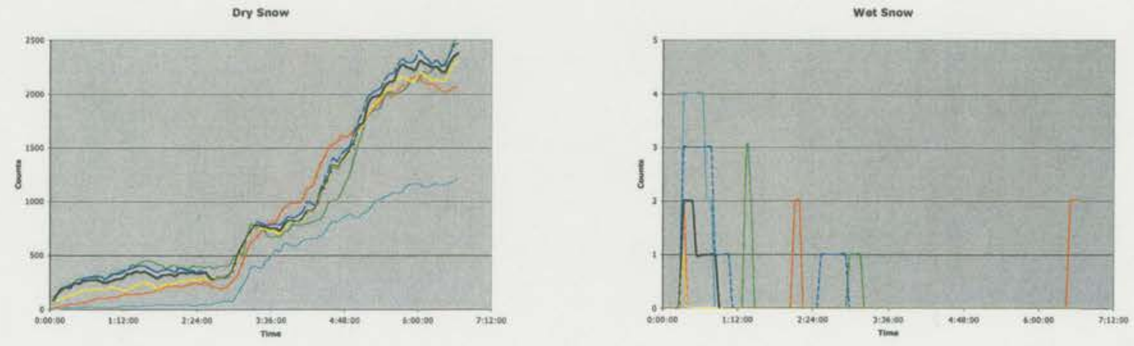

Figure 3.4: Same as Fig. 3.3, except classifications are from 18 June 2003.

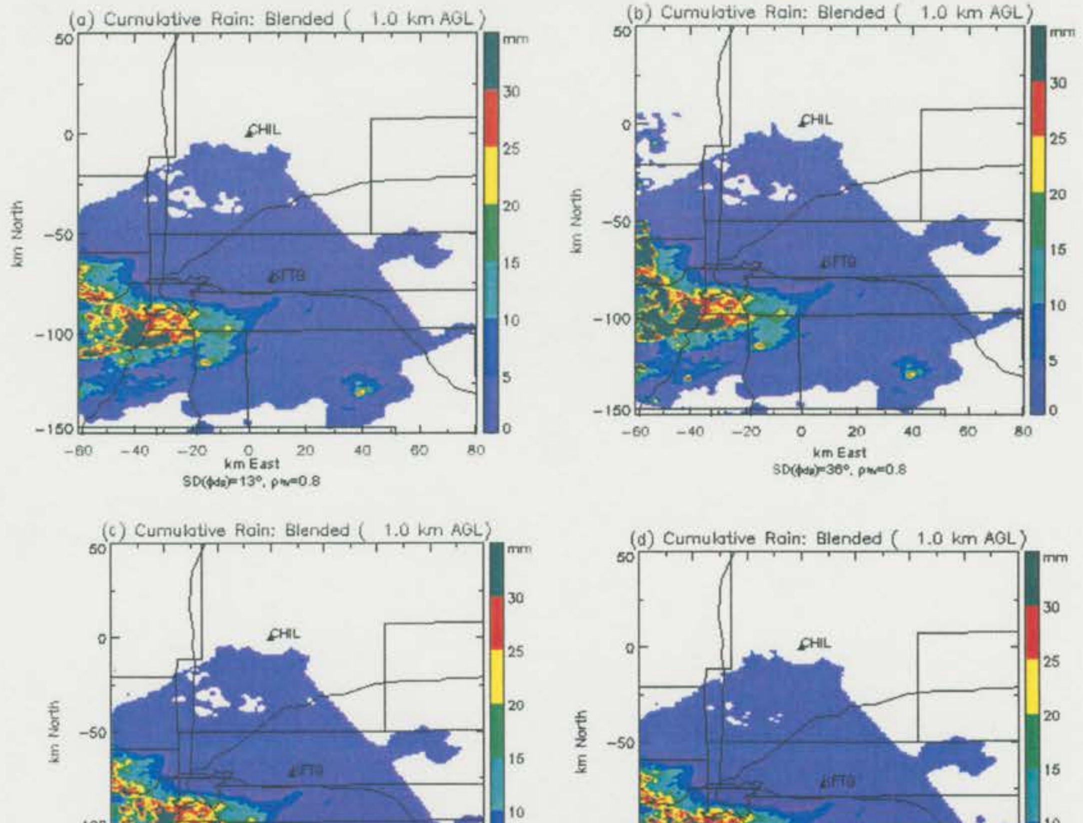

Figure 3.5: Total accumulated rainfall from 28 August 2002 with polarimetric thresholds a) SD(ϕ_{dp})=13°, ρ_{hv}=0.8 b) SD(ϕ_{dp})=36°, ρ_{hv} =0.8 c) SD(ϕ_{dp})=18°, ρ_{hv}=0.8 d) SD(ϕ_{dp})=18°, ρ_{hv}=0.75 e) SD(ϕ_{dp})=18°, ρ_{hv}=0.85, f) SD(ϕ_{dp})=18°, ρ_{hv}=0.9.

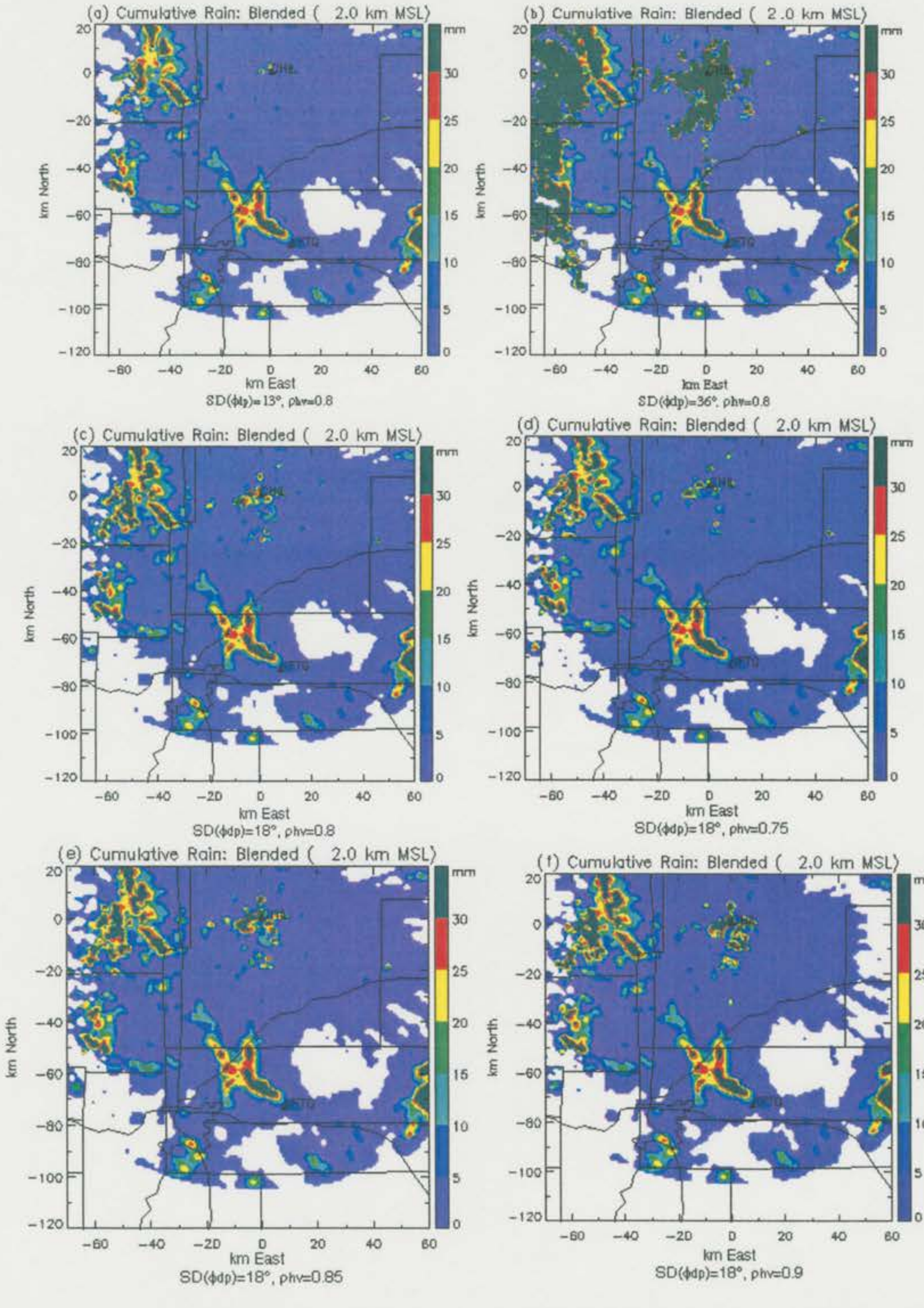

Figure 3.6: Total accumulated rainfall from 18 June 2003 with polarimetric thresholds a) SD(ϕ_{dp})=13°, ρ_{hv}=0.8 b) SD(ϕ_{dp})=36°, ρ_{hv} =0.8 c) SD(ϕ_{dp})=18°, ρ_{hv}=0.8 d) SD(ϕ_{dp})=18°, ρ_{hv}=0.75 e) SD(ϕ_{dp})=18°, ρ_{hv}=0.85, f) SD(ϕ_{dp})=18°, ρ_{hv}=0.9.

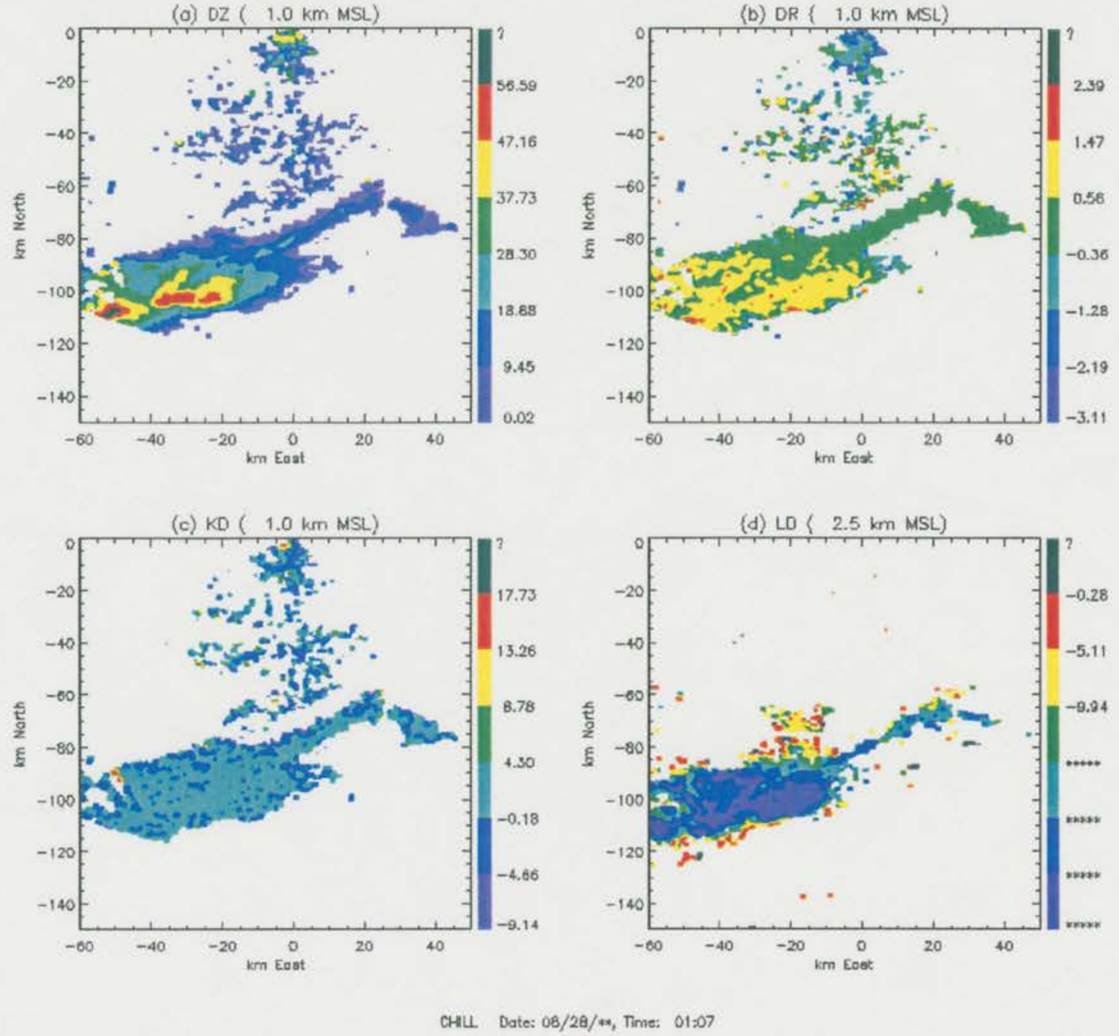

Figure 3.7: a) Reflectivity, b) differential reflectivity (DR), c) specific differential phase (KD), and d) linear depolarization ratio (LD) for 28 August 2002 at 0107 UTC. The data were not thresholded using polarimetric information.

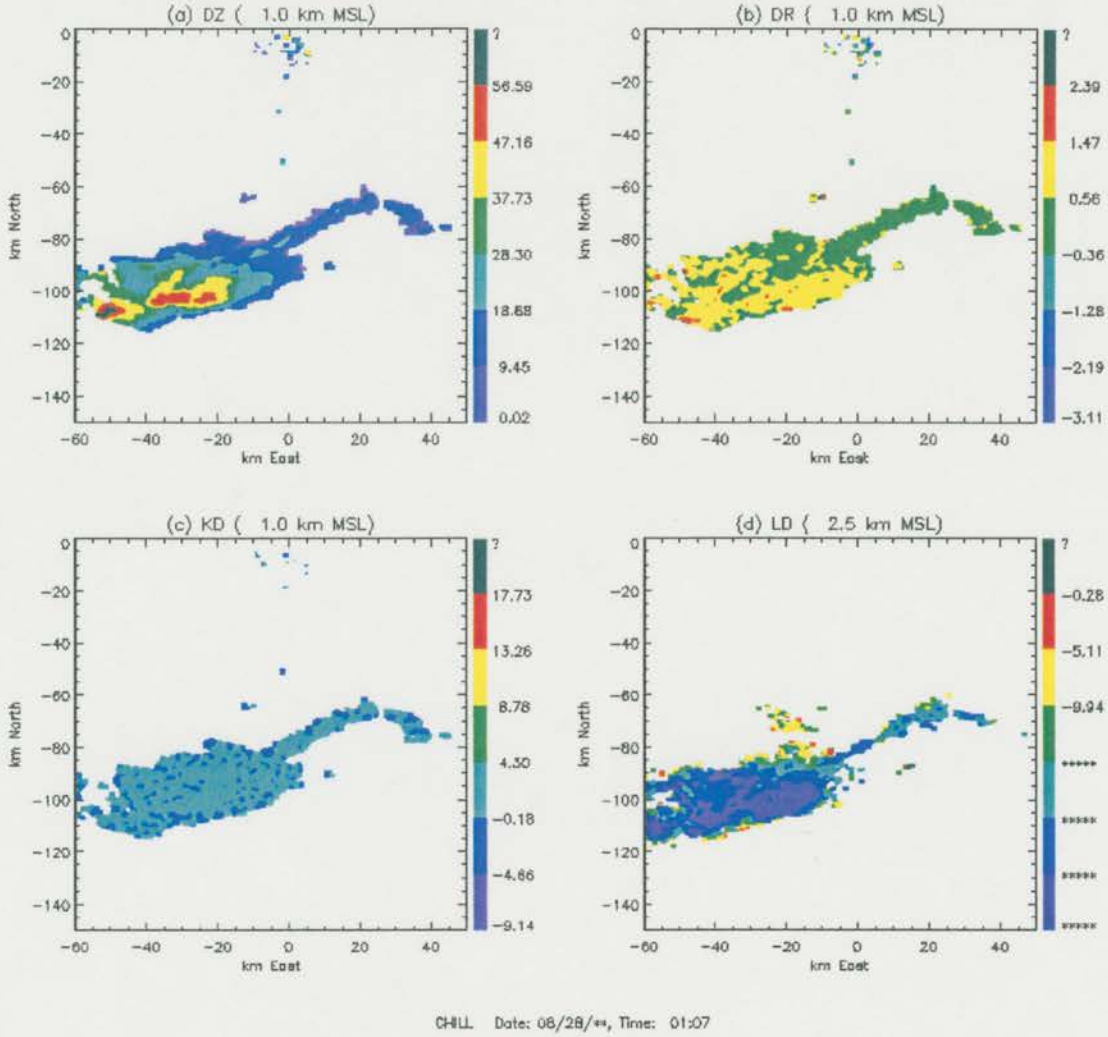

Figure 3.8: a) Reflectivity, b) differential reflectivity (DR), c) specific differential phase (KD), and d) linear depolarization ratio (LD) for 28 August 2002 at 0107 UTC. The data were thresholded using ρ_{hv}=0.8 and SD(ϕ_{dp})=18°.

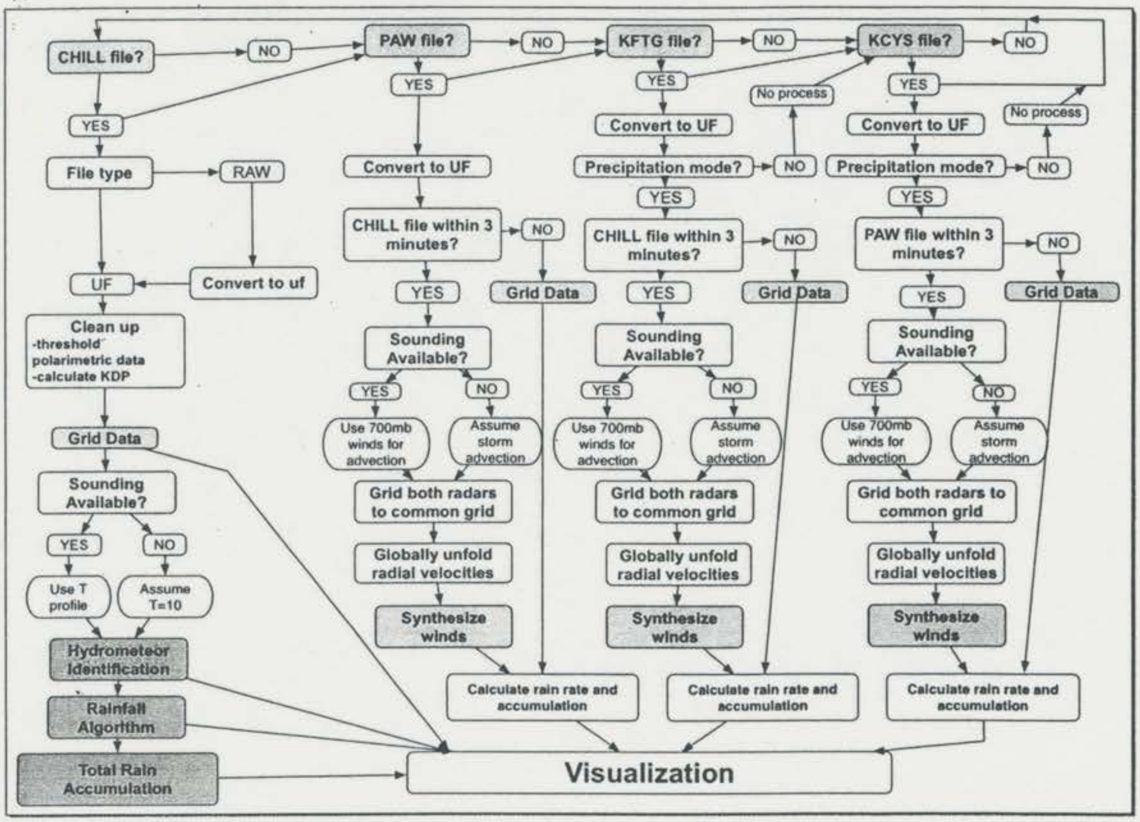

Figure 3.9: Flow chart of the integrated display and analysis tool for multi-variable radar data processing in real-time.

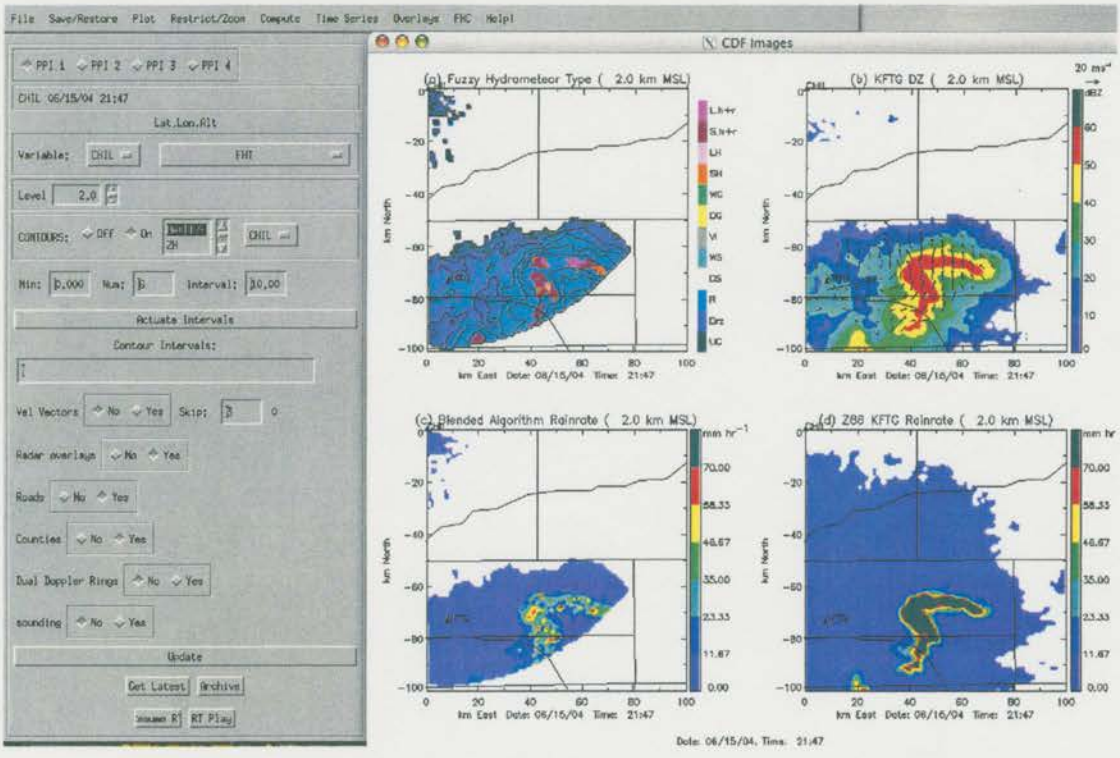

Figure 3.10: An example of the User Interface for the real-time display tool. The control panel to the left illustrates the standard options available for configuration of the images in real-time. In the CDF Image panel, a) shows the hydrometeor identification classification with CHILL reflectivity contours, b) shows KFTG reflectivity with dual-Doppler winds overlaid, c) shows the rain rate calculated from the CHILL blended algorithm, and d) shows the rain rate calculated using the Z-R relation on KFTG data at 2.0 km MSL on 15 June 2004 at 2147 UTC.

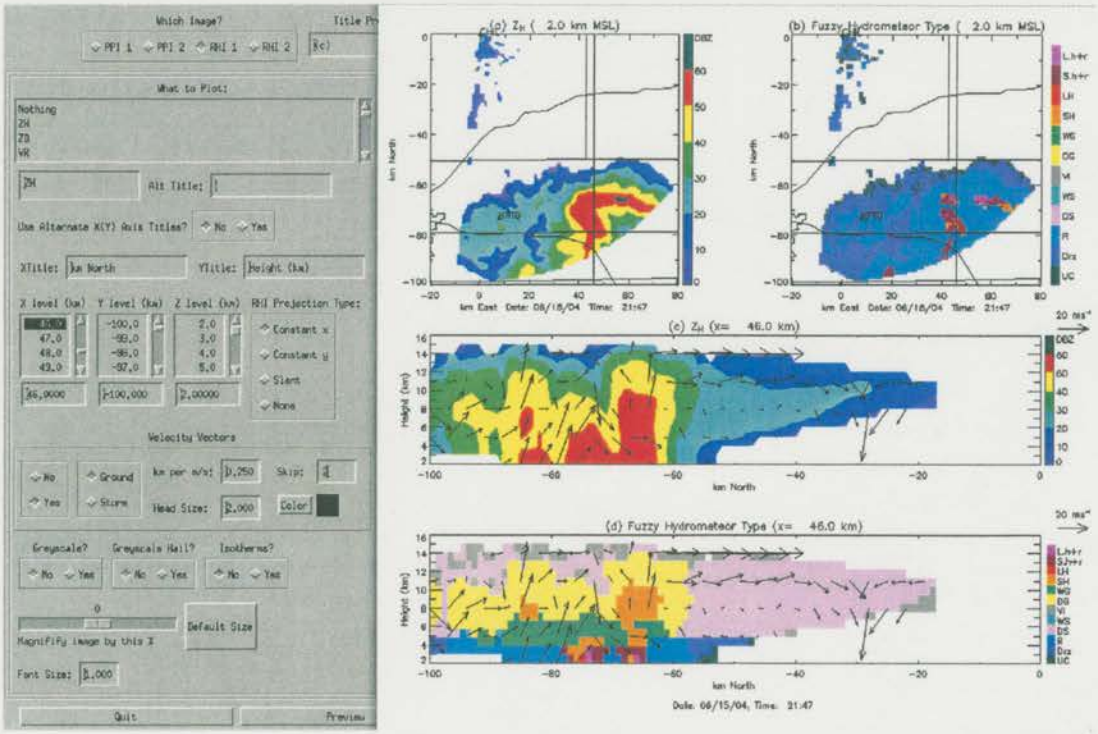

Figure 3.11: An example of the User Interface for the real-time display tool. The control panel to the right illustrates the expanded options for configuring images. Here, the user has selected to view two vertical cross-sections as well as two Constant Altitude Planned Position Indicator (CAPPI) plots. Data is from 15 June 2004 at 2147 UTC. a) Reflectivity and b) Hydrometeor type from CHILL data at 2.0 km MSL. c) Reflectivity and d) Hydrometeor identification vertical cross sections at x=46.0 km from CHILL with dual-Doppler winds from a synthesis with KFTG.

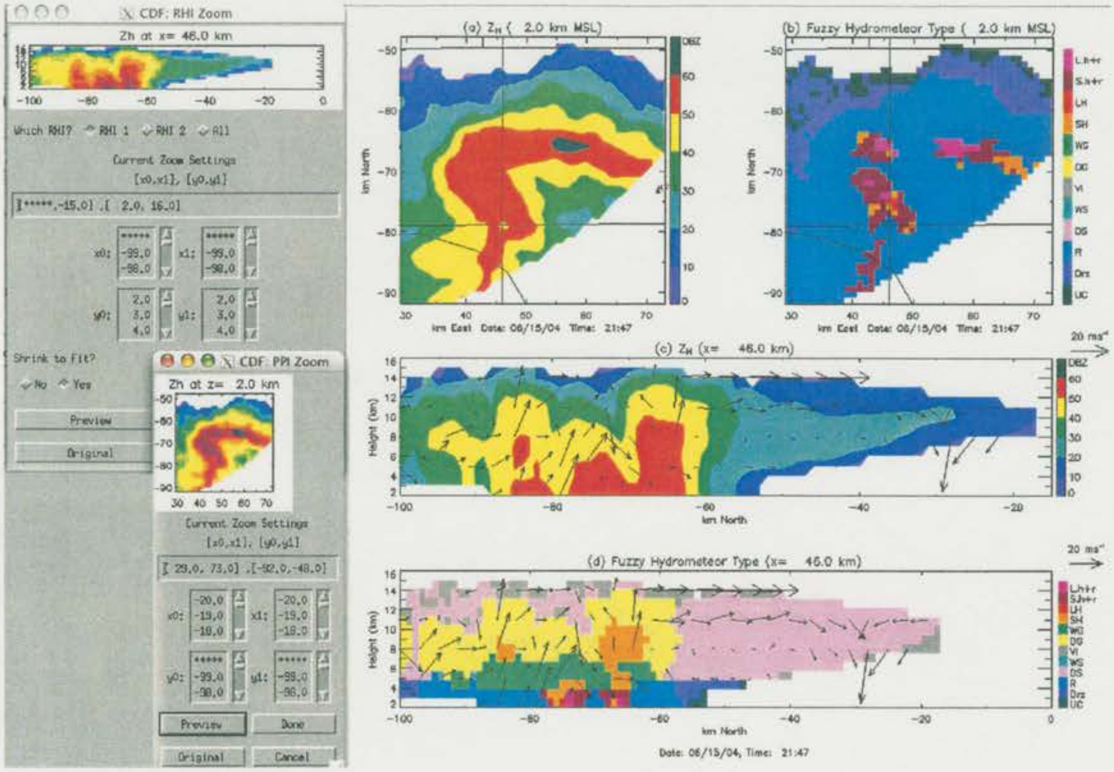

Figure 3.12: An example of the User Interface for the real-time display tool. This illustrates the functionality and the control panel for the zoom function. The images are exactly the same as Fig. 3.11 except both the CAPPIs and RHIs have been zoomed in.

CHAPTER 4

Results

4.1 Real-time Operations

The software algorithm and display tool were tested in real-time at the CSU-CHILL (henceforth referred to as CHILL) radar facility in Greeley, CO beginning 09 June 2004. At the time, CHILL was participating in the Global Precipitation Measurement Mission (GPM) pilot project (http://radarmet.atmos.colostate.edu/gpm). Although the field project did not include aircraft, it did incorporate several disdrometers, wind profilers, and the National Oceanic and Atmospheric Administration (NOAA) - Environmental Technology Lab's (ETL) X-band radar. The coincidence of the GPM project with the software testing period provided an opportunity to utilize the software during a field campaign, but the scientific goals of the GPM project also restricted the data that could be collected by CHILL.

The GPM pilot project had several scientific objectives, including dual-wavelength radar drop size distribution and rain rate estimate intercomparison, rain rate and drop size distribution characterization in the context of various rainfall regimes, and demonstration of profiler technologies to diagnose the vertical structure of precipitation (Rutledge *et al.*, 2004). In order to meet these goals, the scanning strategy for CHILL included 40° azimuth sector scans to the south over the X-band radar located near Erie, CO, the profiler in Platteville, CO, and the Boulder Atmospheric Observatory (BAO) platform operated by NOAA-ETL located near Erie, CO (Fig. 4.1). Scan volumes included three low-level elevation tilts (0.5°, 1.0°, and 1.5°) intermixed with selected Range Height Indicator (RHI) scans. Depending on the rainfall regime, the scan sequence would either repeat either every 2-3 minutes or every 6-8 minutes. For these scans, the range resolution was set to either 75 m or 150 m, respectively, and the effective range was limited to 100 km. The area between 0-20 km from CHILL in range was masked out for clutter reduction. The location of the 40° sector scan limited comparisons between KCYS and CHILL, but provided ample data for analysis with KFTG. Although KFTG and CHILL were not coordinating scans, the relatively short CHILL volume scans allowed for many dual-Doppler wind synthesis opportunities. There were two problems associated with the wind-synthesis in this configuration: 1) the 40° sector scan encompassed the baseline between KFTG and CHILL where winds are not retrievable due to the less than 30° beam-crossing angle and 2) the three low-level elevation angles in the CHILL scans limited the retrieval of vertical winds because the boundary conditions were not sampled. However, CHILL was able to occasionally perform 360° full volume scans with elevation angles ranging from 0.5° to 19°, and coordinate the volumes with KFTG or KCYS. For example, between 2053 UTC and 2120 UTC on 19 June 2004 CHILL performed 360° scans at the three elevation angles to allow for the comparison of data between KFTG, KCYS and CHILL. On 15 June 2004, CHILL coordinated scans in both time and volume coverage pattern with KFTG between 2142 UTC and 2207 UTC, which provided excellent dual-Doppler coverage of a storm in the eastern dual-Doppler lobe. Finally, on 25 June 2004 scans were coordinated with KCYS to capture a cell near the Colorado-Wyoming border from 2308 – 2343 UTC.

In the following discussion and cases, the grid resolution was set to 1 km x 1 km x 1 km within a xyz-domain specified by the user (usually 141 km x 141 km x 14 km) with the grid origin for all radars centered on CHILL. A 1 x 1 x 1 xyz radius of influence was used in the Cressman weighting scheme.

One of the important questions that needed to be answered during real-time testing was 'how real is real-time?' The workstation described in section 3.2.1 was not available until mid-July when the CHILL radar was no longer collecting regular data; therefore all the times cited below are using an older, slower system. The new workstation will hopefully improve computational time for the processed data, but it has not been tested at the time of this writing. Data from CHILL were displayed on the user's screen approximately 90 seconds to three minutes after the completion of a volume scan, depending mostly on the number of points specified in the Cartesian grid interpolation. Data from the KCYS and KFTG WSR-88Ds were available for processing about 9-11 minutes after the beginning of a precipitation-type volume scan, and the processed data showed up on the screen an average of 2-3 minutes after they were available. Thus, the scientist was viewing NEXRAD data that was 11-14 minutes old, but CHILL data that was only 3 minutes old. Dual-Doppler winds appeared on the display approximately 13-15 minutes after the beginning of the oldest of the two synthesized volume scans. While these times are not 'real-time' in the sense that they are instantaneously available after the completion of a volume scan, they are comparable to the 'real-time' demonstrated during the MAP campaign described in Chapter 1.

Additionally, as will be discussed below in section 4.2, the utility of these real-time winds was demonstrated despite being 10-15 minutes behind 'real-time'.

It was evident during the testing that the component contributing the most to the lag time was the LDM. It took an average of 5-8 minutes to download the complete volume scan from one of the WSR-88D radars, and when a file from both radars was available, the time would increase to almost 10 minutes to download both files. The greatest time component from a computational algorithm was associated with the interpolation from radar coordinates to Cartesian coordinates (REORDER). The speed of this algorithm is highly dependent on the number of grid points input by the user. This computational time is expected to improve with the processing power of the new workstation.

In addition to the interactive display tool available at the CSU-CHILL radar facility, images were generated in real-time and uploaded to the CHILL website (http://chill.colostate.edu/image_2004/index.html) beginning 29 June 2004. An example of the web image is shown in Fig. 4.2. The top panels show the hydrometeor identification results and the total rain accumulation using the blended algorithm at 1.0 km above ground level (AGL; in this case, approximately 2.5 km MSL). The bottom images provide a comparison between rain rate calculations from KFTG (standard midlatitude Z-R relationship, Eqn. 2.25) and the CHILL blended algorithm method described in section 2.4.2. These images were available approximately 10-13 minutes after the beginning of the WSR-88D volume time.

4.2 *Case Studies*

4.2.1 *Case 1: 09 June 2004*

On the afternoon of 09 June 2004, convection broke out around 2000 UTC (1400 LT). Several severe storms near the Denver metro area spawned tornados, large hail, and damaging winds. These storms were observed by the KFTG and CHILL radars from approximately 2100 UTC through 00 UTC on 10 June 2004. The storms moved to the northeast though the domain, and core reflectivities reached above 60 dBZ. The storm swath, calculated using the highest reflectivity at each xy-grid point over the three hour time period, is illustrated in Fig. 4.3. Two distinct cells moved through the area, one to the west, beginning in Jefferson County and moving through Denver and into Adams County, and the other to the east of Denver moving through Arapahoe County and northeast through Adams County.

The 12 UTC Denver sounding (see Fig. 4.3 for the sounding station location) on 09 June 2004 shows two low-level inversions topped by a deep moist adiabatic layer. Consequently, CAPE was very small. Southerly winds prevailed at lower levels (Fig. 4.4). The 700 mb winds, which were used in the calculation of storm advection, were 7.7 ms^{-1} from the SSW. Surface observations at Denver indicate that by 1943 UTC temperatures had reached mid-70's with dew points in the mid-50's and winds blowing from ESE at 7.7 ms^{-1}.

Scientists at CHILL were able to use the software described in this thesis to observe many aspects of these storms as they evolved. For example, supplemental data provided by the WSR-88D KFTG radar filled in vertical and horizontal information where CHILL was limited by three elevation angle sector scans. This allowed the scientist to observe aspects of the upper storm structure and spatial variability while still meeting the requirements for the GPM pilot project scanning strategy for the CHILL radar. This is illustrated in Fig. 4.5, which shows a Constant Altitude Planned Position Indicator (CAPPI) at 2.5 km MSL of the horizontal and vertical reflectivities from both the KFTG and CHILL radars at 2128 UTC. In this case, the limited scope of the CHILL scan cuts off the southern edge of a cell located at x=-37 and y=-90. The bottom panels of Fig. 4.5 show a vertical cross section of KFTG reflectivity at x=-37, revealing the > 50 dBZ core reaching to 10.5 km MSL.

At 2215 UTC, the dual-Doppler derived winds indicated a mesocyclone associated with the storm to the east of Denver. At the same time, the hydrometeor identification revealed large regions of large hail mixed with rain, as well as areas of small hail mixed with rain (Fig. 4.6). This particular example shows an excellent application of the new software. Additionally, the region containing rain rates greater than 70 mm hr^{-1} was greatly reduced using the CHILL polarimetric data rather than the standard midlatitude Z-R from KFTG. The Boulder forecast office reported a tornado, marked on Fig. 4.6 with a 'T', and 0.75" hail, marked on Fig. 4.6 with an 'H', at 2215 UTC.

The dual-Doppler derived winds also provided insight into the characteristics of the western storm. Winds from a synthesis at 2219 UTC show a convergence line out in front of the storm, possibly co-located with the path the storm took as it moved off to the north (Fig. 4.7). At 2108 UTC, data showed a large area of discrepancy between the NEXRAD Z-R rain rates associated with the storm and the rain rates calculated using the polarimetric data from CHILL (Fig. 4.8). Hydrometeor identification at the same time indicated the presence of large and small hail, which could possibly contaminate the Z-R based rain rate estimate. The Storm Prediction Center reported two incidences of large hail at this time, marked with an 'H' on Fig. 4.8. The eastern hail report corresponded with 2.25" diameter hail, while the western point 1.75". These two hail reports are closely located to regions identified by the fuzzy logic algorithm as containing hail. Finally, by 2353 UTC, the 3 hr total rain accumulation calculated from CHILL indicated much lower accumulations than those derived from the NEXRAD Z-R relation, particularly associated with the western cell (Fig. 4.9).

To examine this discrepancy, the Denver rain gauge network associated with the Urban Drainage and Flood Control District (UDFCD) was used to validate the derived accumulations and rain rates. The total accumulations measured by the tipping bucket rain gauges in the Denver-metro area are shown in Fig. 4.10. Four rain gauges with a variety of total rain accumulation values were selected for comparisons with the radar data. Figure 4.10 shows the locations, indicated by an orange circle, of these four gauges within the radar domain.

As an example of the methodology for this study, gauge #1420 will be investigated. This gauge was located near the center of the storm at 2109 UTC (see Fig. 4.8), corresponding to an area identified as hail by the hydrometeor identification algorithm and in a region of large rain rate differences between the CHILL and KFTG techniques. The radar data from the closest 1 km by 1 km grid box over the gauge latitude and longitude were extracted and plotted as a time series for comparison with the rain gauge trace. This is illustrated in Fig. 4.11. The KFTG Z-R rain rate at 2110 UTC was over 100 mm hr^{-1}, while the CHILL rain rate indicated 25 mm hr^{-1} and the tipping bucket measured approximately 20 mm hr^{-1}. Fig. 4.12 shows a trace of the CHILL data over the gauge point. Reflectivities were high, Z_{dr} and K_{dp} were low, and the ice fraction was relatively high (Fig. 4.12a,b,c,f). The CHILL blended algorithm was using an R-K_{dp} (Eqn. 2.27) relation to discriminate between the ice and the liquid water in the volume (Fig. 4.12d). Fig. 4.12e indicates that at that same time, hydrometeor classification identified small hail over the gauge which may have contaminated the NEXRAD rain rate by dominating the reflectivity measurement. The total rain accumulation from the NEXRAD Z-R was 25.14 mm, while the blended algorithm calculated 14.44 mm and the rain gauge measured 5.08 mm. Figure 4.13 shows the total ice fraction across the xy-domain at 2.5 km as a function of time. The pattern is variable, with the average ice fraction between 0.15 and 0.3.

Comparisons with the other three rain gauges revealed similar results. The rain traces and analysis over the other three gauges is presented in Appendix B, Figs. B.1-6. In all four cases, the CHILL blended algorithm did a better job estimating the measured rain rates and rain accumulations (Table 4.1). In three cases, both CHILL and KFTG significantly overestimated the total rainfall accumulation, with KFTG returning a greater accumulation than CHILL. This could be attributed to the precipitation ice dominating the returned radar signal, and therefore increasing the rain rate calculated by the Z-R relationship. The CHILL blended technique used mostly the $R(Z_h, Z_{dr})$ relationship (Eqn. 2.29) to calculate rain rates. This relationship is expected to give a better estimation of the rain rate compared to the standard Z-R relation, since Z_{dr} is proportional to D_o (median volume diameter) and therefore captures more parameters of the drop size distribution. The consistent overestimation by the radars could be attributed to smoothing due to the grid resolution of 1km compared to a localized gauge measurement. It could also be accounted for by considering the vertical distance between the gauge and the radar measurements. The radar measurements were calculated at 2.5 km MSL, while the gauges are situated at the surface (1.6 km MSL). Between the two measurements, winds could advect the precipitation or evaporation could occur, resulting in a decrease in the rain rate at the surface.

The differences between the rain gauge and the radar could also be attributed to rain gauge measurement errors. Tipping bucket rain gauges (such as those used by UDFCD) have several known measurement errors, including loss from evaporation, wind effects, calibration, and nonlinear "undercatchment" due to the mechanical design of the tipping bucket (Nemec, 1969; Humphrey *et al.,* 1997). Humphrey *et al.* (1997) found that the underestimation errors ranged from 3% to 29% and increased with increasing rainfall rate, especially in cases where rain rates exceeded 50 mm h^{-1}. Tipping buckets can also overestimate rain rates because of double tips resulting from either intense rain events or instruments that are not level (Parkin *et al.*, 1982; Groisman and Legates, 1994).

Perhaps a better method for comparing the rain gauge data to the radar data would be to take a 1 km by 1 km average of the rain rate calculated at each gate along the radar beam, rather than compare gauge data to one rain rate calculated at a single 1 km by 1 km grid point. This would result in a more accurate estimation of the rain rate over the gauge. Additionally, one could look at the root mean square of the error variance between the radar and gauge estimates to help normalize differences between events with large accumulations compared to small accumulations. Both of these analysis methods could improve the results of this validation.

4.2.2 Case 2: 27 June 2004

On 27 June 2004, local flooding occurred in communities located along the foothills to the west of Denver. During an approximately 1 hour period between 2100-2200 UTC (1500-1600 LT), some locations in Golden received over 2" (50.8 mm) of rain leading to significant damage of several houses. The intense rain was associated with a nearly stationary cold front backed up against the foothills. The winds reported at the Denver station at 2100 UTC were blowing out of the northeast at 7.7 ms^{-1} (see Fig. 4.14). The storm swath for the 3 hour period between 2100-2359 UTC is shown in Fig. 4.15.

The 12 UTC Denver sounding (see Fig. 4.15 for sounding station location) on this day (Fig. 4.16a) represents a relatively moist atmosphere, with a surface inversion and light winds at low levels. However, by 0 UTC on 28 June, 2 hours after the flood event ended, the Denver sounding was nearly saturated throughout all levels, with a small adiabatic layer near the surface (Fig. 4.16b). Reflectivities associated with the storm remained moderate, rarely exceeding 55 dBZ during the 3 hour period. These characteristics are in contrast to the convective nature of Case 1 described above.

CHILL performed complete volume scans including 7 to 9 elevation angles over a sector covering the foothills between 2052 UTC and 2359 UTC. This provided an opportunity for several dual-Doppler syntheses with KFTG over the lifetime of the storm, leading to insights about the vertical structure of the storm. For example, Fig. 4.17 shows two CAPPIs from CHILL data at 2.5 km MSL and two vertical cross-sections corresponding to x=-44.0 km from 2120 UTC. Shown in Fig. 4.17a is the CHILL reflectivity field overlaid with the dual-Doppler derived wind field. The winds indicate weak easterly flow turning more northerly to the north in the grid, suggesting confluence in that portion of the domain. The reflectivity shows several cells backed up against the foothills containing mostly rain and drizzle, with the possibility of small hail associated with the more intense regions (Fig. 4.17b). The vertical cross-sections (Fig. 4.17c,d) illustrate the hydrometeor type and reflectivity, as well as the vertical wind field. The winds show moderate updrafts (peak values to 19.5 ms^{-1}) associated with each reflectivity core, with inflow at low-levels and outflow at the mid and upper-levels. The reflectivity contours overlaid on the hydrometeor type reveal small hail possibly mixed with rain inside the most intense core located at y=-110 km from CHILL. Hydrometeor identification also reveals wet and dry graupel in the midlevels of the cores.

The total rain accumulations again reveal larger areas of greater rain accumulation using the standard midlatitude Z-R compared to the CHILL blended technique (Fig. 4.18). Applying the same methodology as Case I, the Denver rain gauge network was used to compare radar derived estimates to 'ground truth'. Total rainfall accumulations measured by the gauges are shown in Fig. 4.19. The four gauges selected for the study are boxed and labeled in orange.

Gauge #330 is located near the town of Golden where most of the flooding was reported. This particular gauge recorded the highest rainfall total of 52 mm (2.05") over the 4 hour period between 2000-2359 UTC. The rain rate traces over this point show good agreement between the KFTG Z-R and CHILL blended techniques, as well as with the rain gauge (Fig. 4.20). The overall distribution shows a long period of rain rates above 50 mm hr^{-1}, and while the rain gauge shows more variability, this could be a result of smoothing the radar data on a 1km grid. The rainfall totals for the radar algorithms show good correlation, with KFTG reporting 62.8 mm and CHILL 61.4 mm. The gauge measured less with 52 mm, but again this could be due to evaporation or winds between the radar measurement at 2.5 km MSL and the gauge at 1.8 km MSL. Fig. 4.21a-c reveals moderate reflectivities, Z_{dr}'s less than 1 dB, and K_{dp} values up to 2 °km^{-1}. The blended algorithm used the R(K_{dp}) method almost exclusively (Fig. 4.21d) to calculate rain rates for this case. The hydrometeor identification indicates possible wet graupel throughout most of the intense rainfall (Fig. 4.21e). Additionally, the fraction of ice at this grid point ranged from 0.2-0.6 during the most intense rain rate period (Fig. 4.21f). Analysis of the other three rain gauges resulted in better agreement between the Z-R and blended algorithms, as well as with gauge measurements, than Case 1, but frequent underestimations of the total rainfall with respect to the gauges (see Appendix B, Figs. B.7-12). CHILL estimates were slightly closer to the gauge value in two cases and KFTG Z-R was closer in the other two (see Table 4.2). Again, a 1 km by 1 km average rain rate calculated at each range gate may yield more insightful results.

The fraction of ice (inferred from the Z_{dp} method described in section 2.2.1) over the xy-grid domain indicates ice fractions steadily increasing from 0.4 at the beginning times to 0.6 near the end of the storms life (Fig. 4.22). Although it may seem surprising that the NEXRAD Z-R performed so well with a larger ice fraction, the drop size distribution must also be considered. The DSD from this case could possibly have been more consistent with a typical midlatitude DSD upon which the NEXRAD Z-R is based. The DSD used in the Z-R calculation in the midlatitudes accounts for precipitation ice and the processes associated with drop formation in the midlatitudes. In a more convective case, such as the 09 June case, the DSD may change throughout the storm, and it may not resemble the DSD used to derive the midlatitude Z-R relation used by KFTG. Additionally, although the fraction of ice over the entire domain was less and more variable for the 09 June case, local maxima in ice fraction (Fig. 4.12f) indicate the possibility that large hailstones may have dominated the radar signal, increasing Z without equal contributions from liquid water droplets, resulting in a degraded performance of the Z-R relation in the convective case. Again, it should be noted that gauges cannot be considered absolute truth either, as tipping bucket-style rain gauges can have significant measurement errors, as described in section 4.2.1.

One final note about the CHILL blended algorithm performance is that the fraction of ice is calculated assuming a Z_{dp} determined by Carey and Rutledge (1996) for a supercell case. If, in the 27 June 2004 case, the rain line was significantly different, it could change the ice fraction and thus alter the method chosen by the algorithm to calculate the rain rate.

The software analysis and display developed for this thesis proved to be a useful tool during these severe weather events. The dual-Doppler winds indicated a probable mesocyclone and tornado that was verified by surface observations, as well as a convergence line possibly related to the storm track. The hydrometeor identification located regions of potential hail at the surface which were also verified by storm reports. The ability to compare the KFTG Z-R and the CSU-CHILL blended algorithms allowed for illustrations of where the Z-R relationship might be overestimating the rain rate due to contamination in the grid volume from precipitation ice. Lastly, the data from the KFTG

WSR-88D supplemented the CHILL data to provide scientists with a wider scope while still maintaining the research objectives of the GPM pilot project.

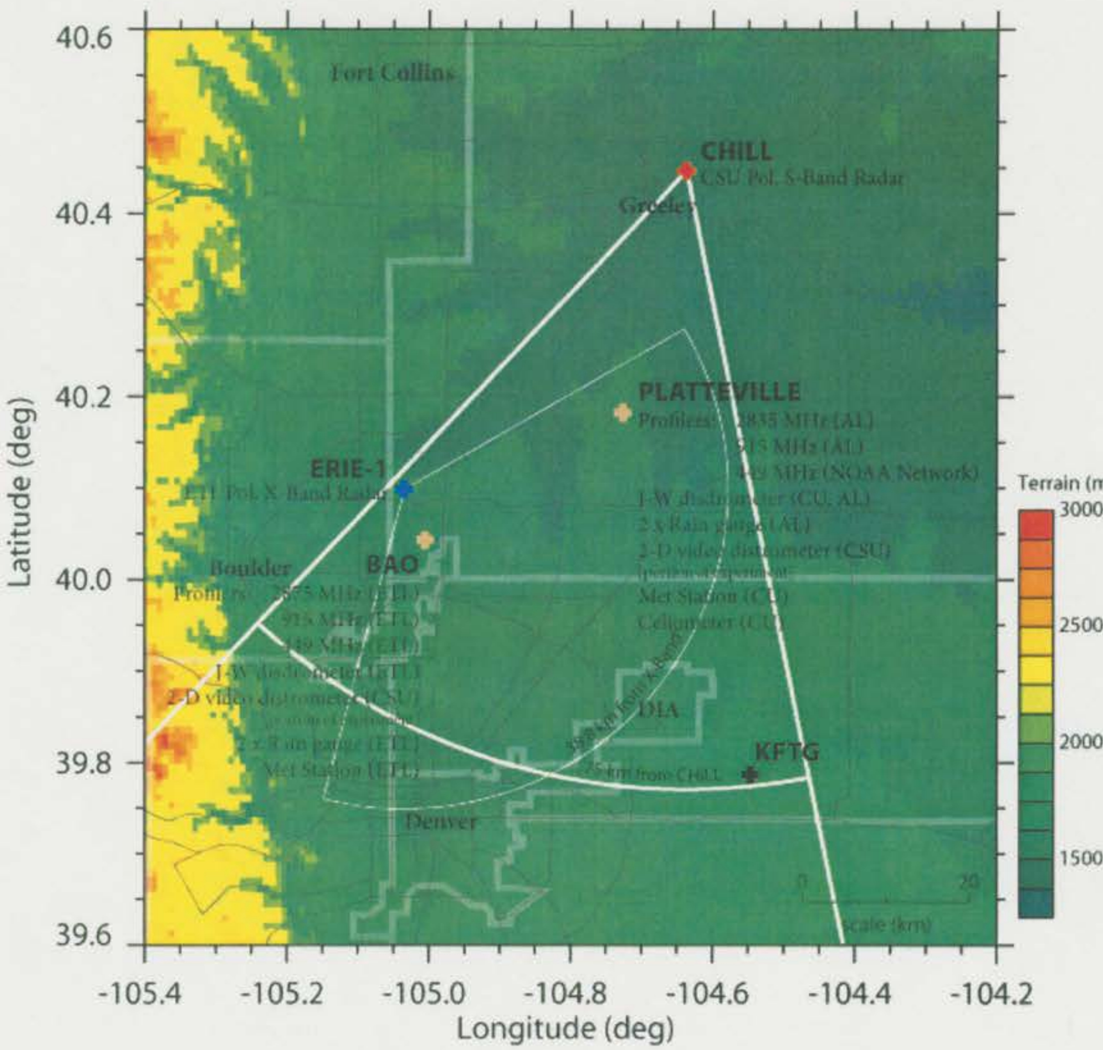

Figure 4.1: The 40° sector scanned by CSU-CHILL radar during the GPM pilot project during June and July 2004 (thick white line) and the corresponding locations of the other participating instruments, such as the Boulder Atmospheric Observatory (BAO) tower and the Platteville profiler. Colored shading denotes the topography in meters (from Rutledge *et al.*, 2004).

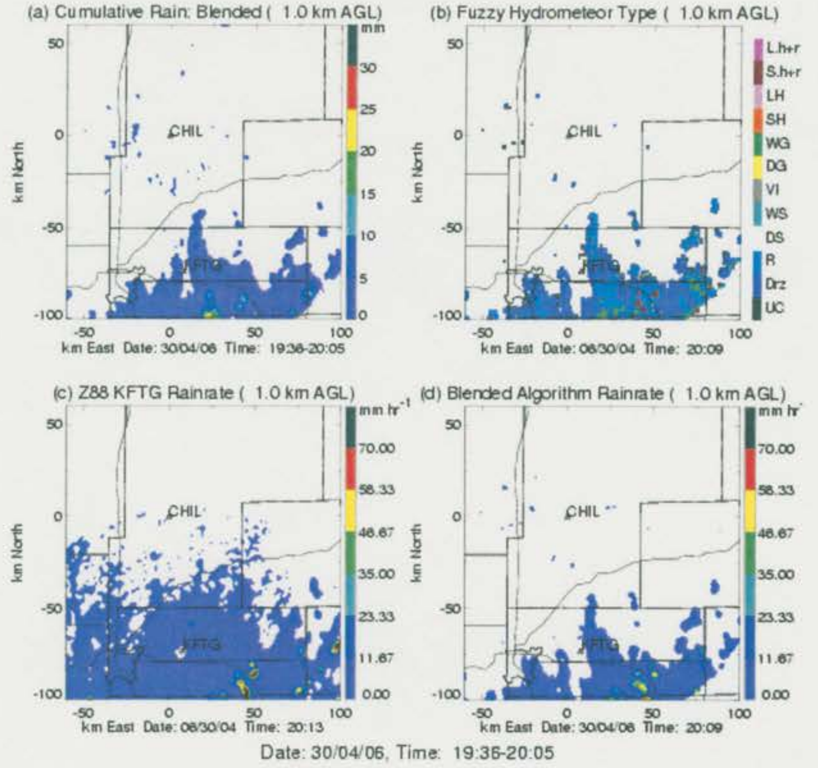

Figure 4.2: An example of images uploaded to the web in real-time on 30 June 2004. Panel shows a) the rainfall accumulation calculated using the CHILL blended polarimetric algorithm from 1936-2005 UTC, b) the hydrometeor type determined by the fuzzy logic algorithm at 2009 UTC, c) the rain rate at 2013 UTC as calculated from the NEXRAD Z-R relationship using KFTG reflectivity data, and d) rain rate determined by using the CHILL polarimetric blended technique at 2009 UTC. Grid origin is centered at the CHILL radar (labeled 'CHL'). Figures such as this were available on the CHILL website (http://chill.colostate.edu) approximately 10-15 minutes after the beginning of the WSR-88D volume scan.

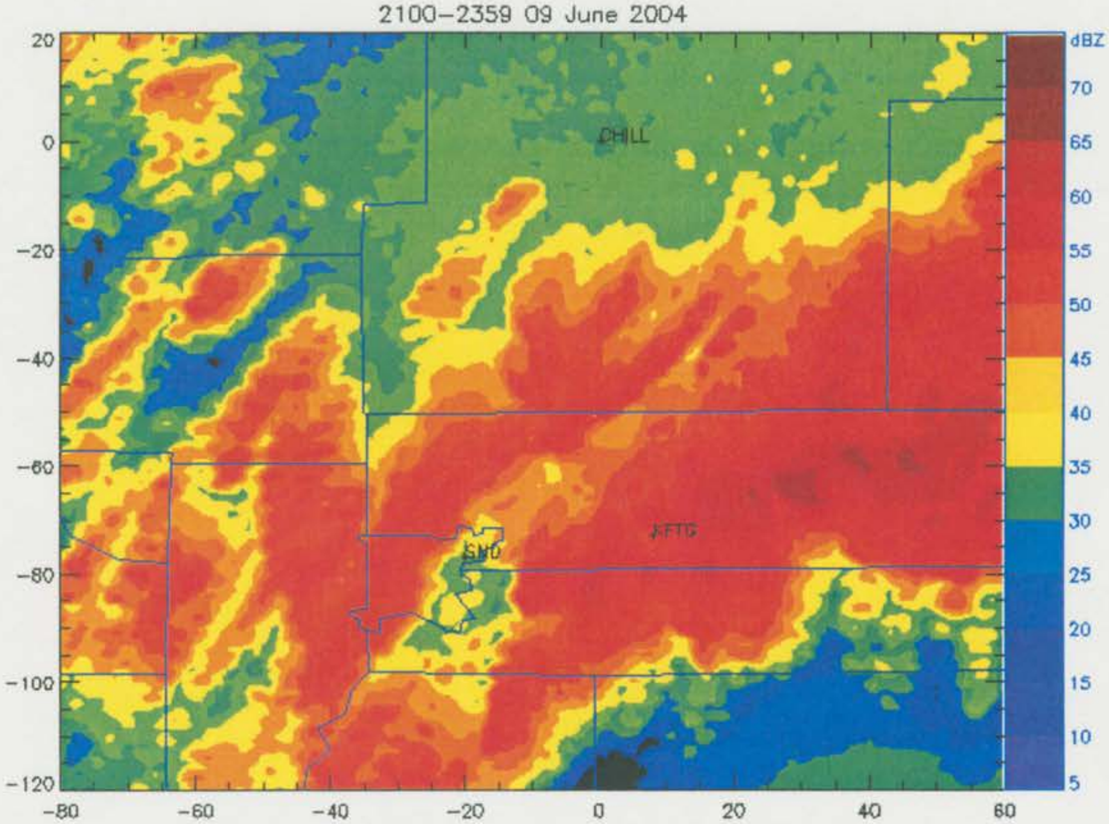

Figure 4.3: Storm swath for storms occurring between 2100 and 2359 UTC on 09 June 2004. The storm swath was calculated by taking the maximum reflectivity from all levels at each xy-grid point over the 3 hour time period. Grid origin is centered at the CHILL radar, and the 'SND' denotes the location of the Denver sounding station.

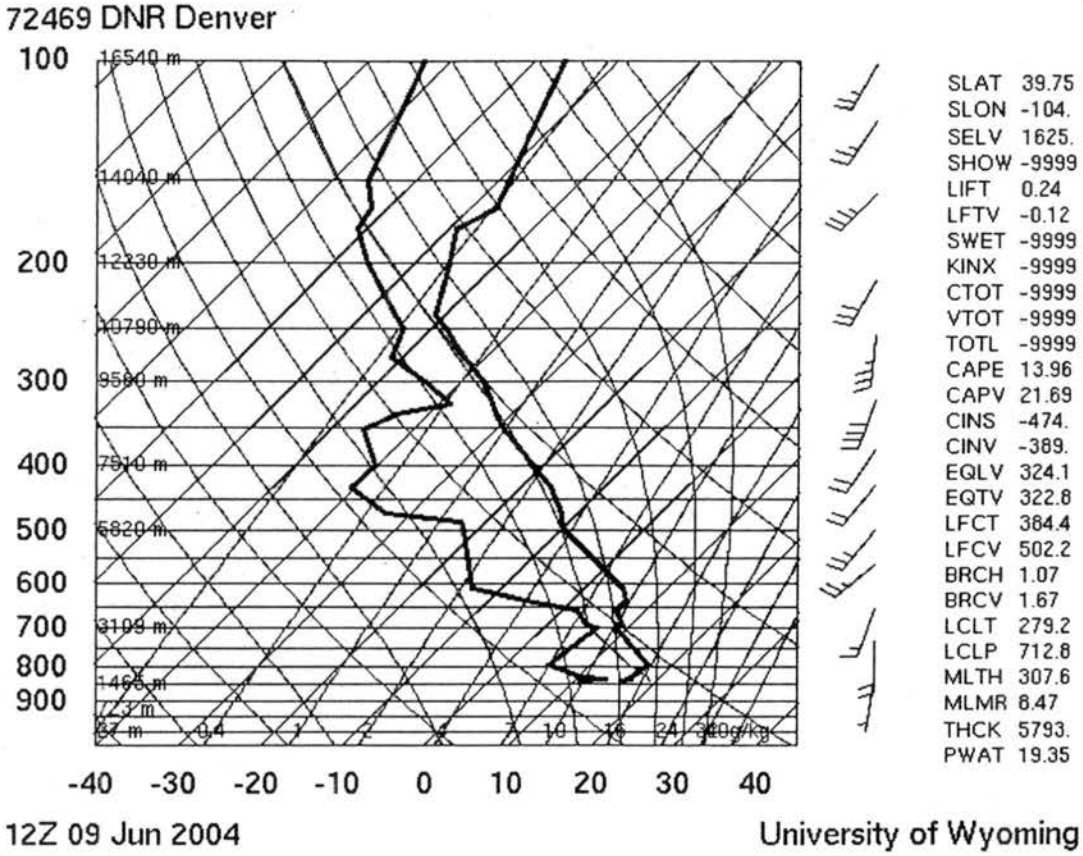

Figure 4.4: Denver Sounding from 12 UTC on 09 June 2004. (Image generated from http://weather.uwyo.edu/upperair/sounding.html).

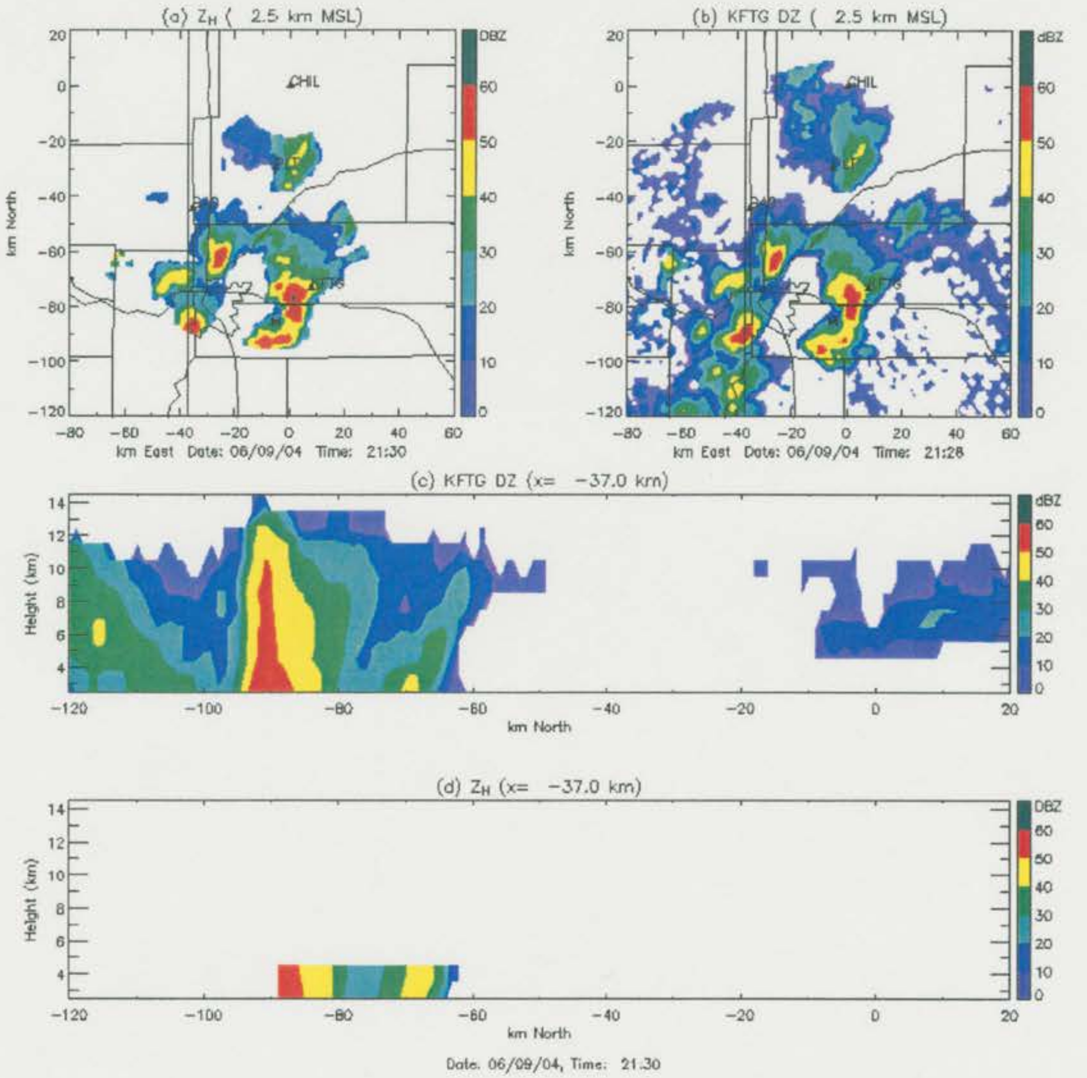

Figure 4.5: An example of how the KFTG WSR-88D enhanced the observations during the GPM pilot field project on 09 June 2004. The grid origin for all data is centered on the CHILL radar. A) Reflectivity (Z_h) from the CHILL radar at 2130 UTC, b) reflectivity (DZ) from the KFTG NEXRAD at 2128 UTC, c) a vertical cross section of KFTG reflectivity at x=-37.0 km (indicated with a black line on panels a and b), and d) vertical cross section of CHILL reflectivity at x=-37.0 km.

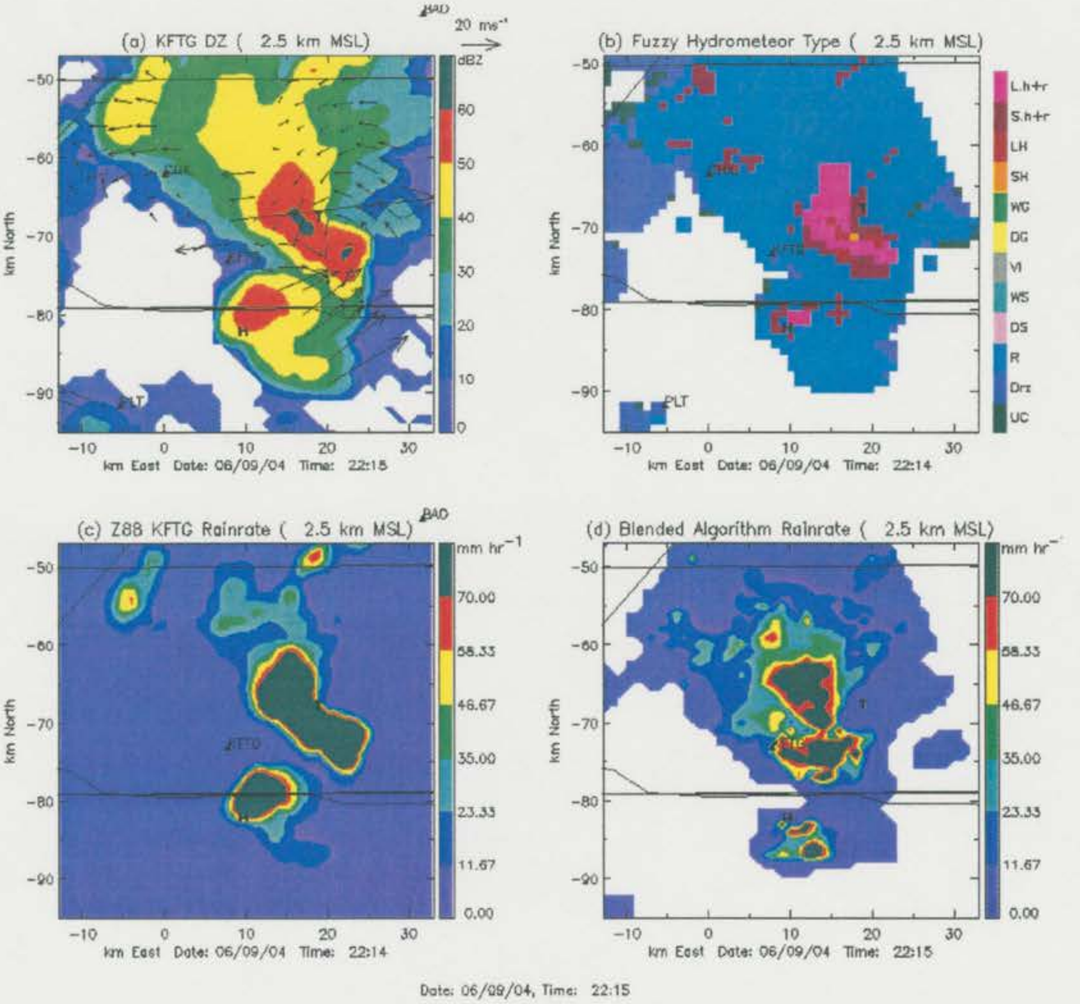

Figure 4.6: Display indicating a mesocyclone in the dual-Doppler winds associated with a tornado, large hail, and high rain rates at 2215 UTC on 09 June 2004. The 'T' denotes the location of a tornado spotted on the ground at 2215 UTC, and the 'H' denotes 1" diameter hail reported on the ground at 2111 UTC. Grid origin is centered on the CHILL radar. Panel illustrates a) reflectivity from KFTG with dual-Doppler winds overlaid, b) hydrometeor type identified by the fuzzy logic algorithm (note the nearly co-located hail observation with large hail identified by the algorithm), c) rain rate associated with the storm from the Z-R relationship using KFTG reflectivity data, and d) rain rate derived using CHILL polarimetric data. All plots are at 2.5 km MSL.

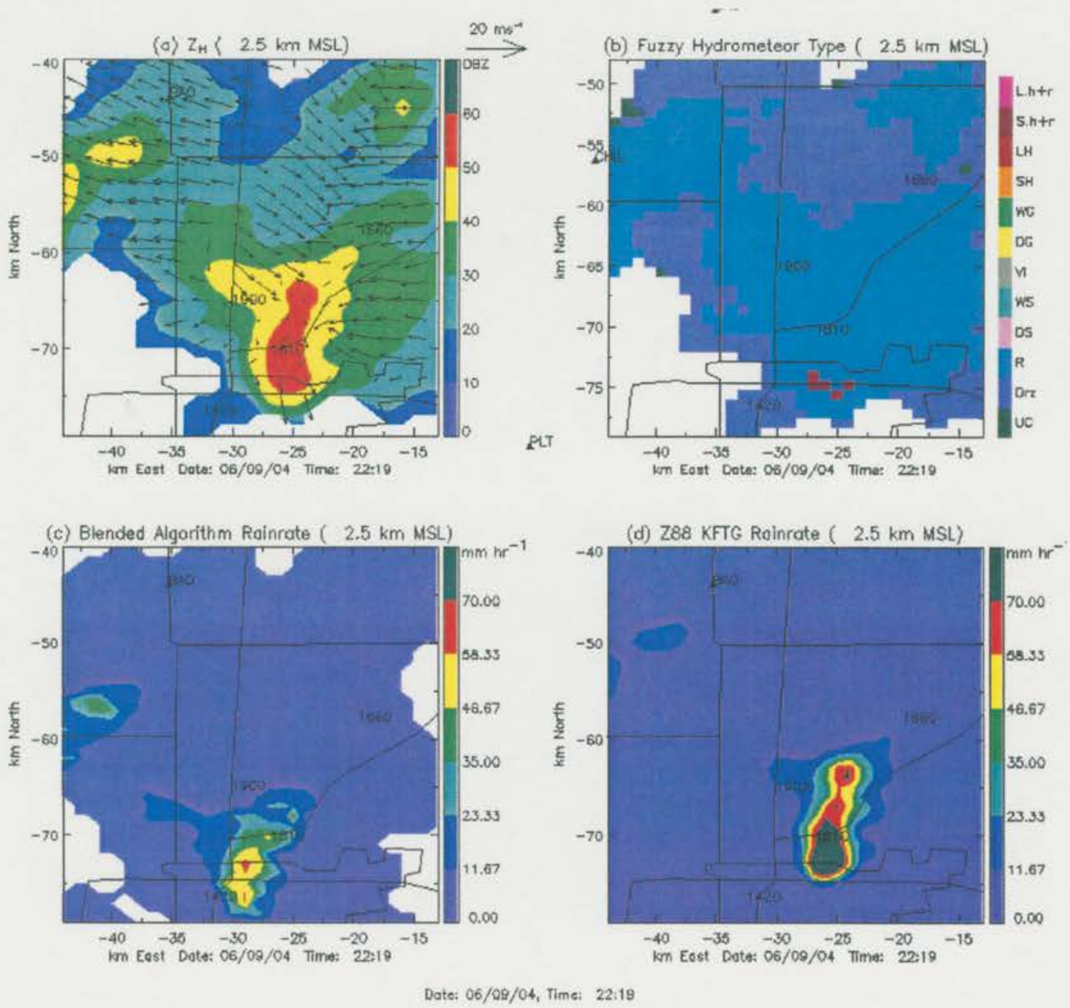

Figure 4.7: Display from 2219 UTC on 09 June showing a) reflectivity with dual-Doppler winds, b) Hydrometeor identification, c) CHILL polarimetric calculated rain rate, d) rain rate derived from the NEXRAD Z-R relation using KFTG reflectivity data. Note the convergence line in front of the storm shown by the dual-Doppler derived winds in a). All figures are at 2.5 km MSL. Black numbers denote the locations of that gauge in the Urban Drainage and Flood Control District.

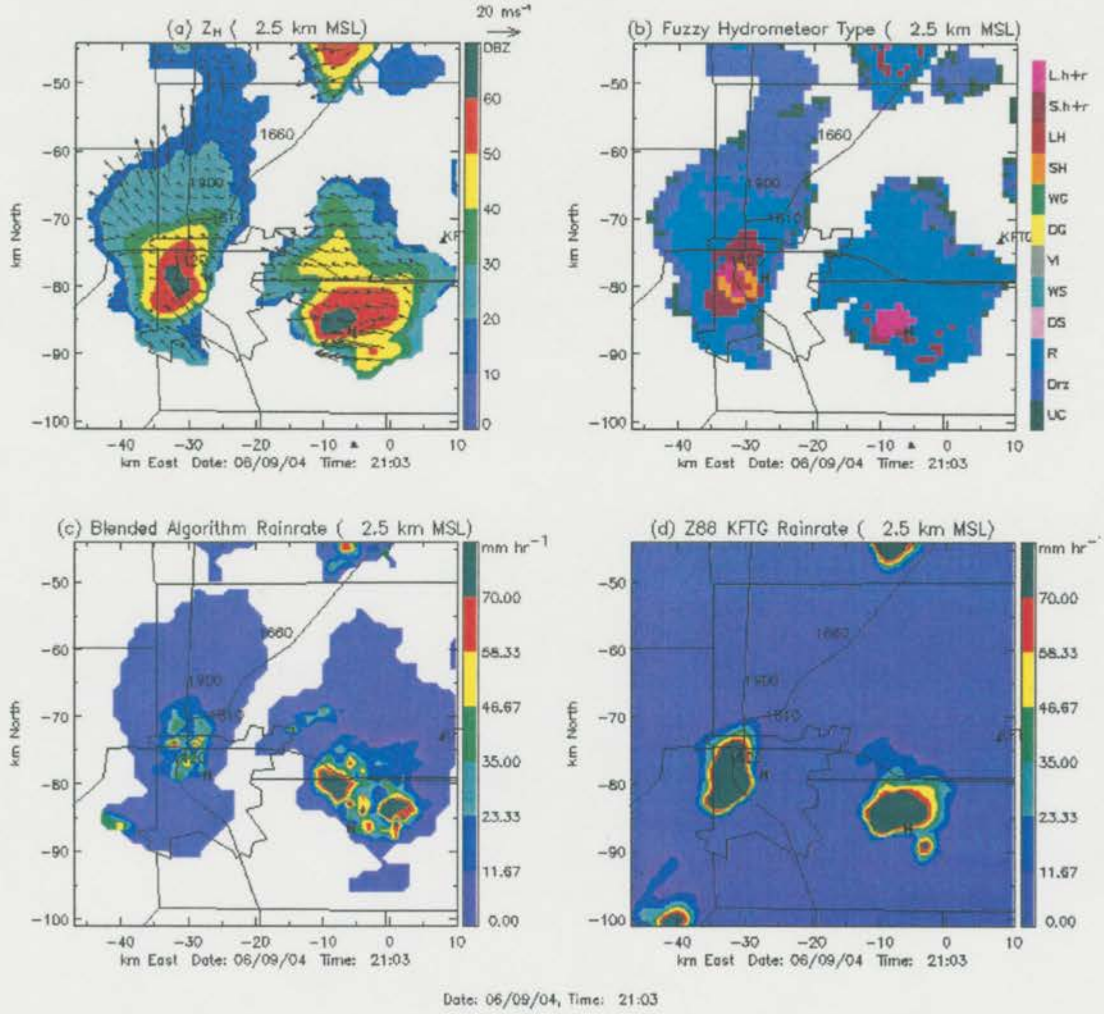

Figure 4.8: Data from 2109 UTC on 09 June, showing discrepancy between the Z-R and blended polarimetric techniques, and hail verification. The western 'H' is located where 1.75" diameter hail was reported at the surface at 2105 UTC, and the eastern 'H' is where 2.25" hail was reported at the surface at 2100 UTC. Black numbers represent the locations of the UDFCD gauges. Grid is centered on the CHILL radar. A) CHILL reflectivity with dual-Doppler winds, b) hydrometeor type (note the proximity of the radar hail locations to surface observations), c) rain rate from the CHILL polarimetric blended algorithm and d) rain rate from KFTG Z-R (note the differences between rates in panels c and d).

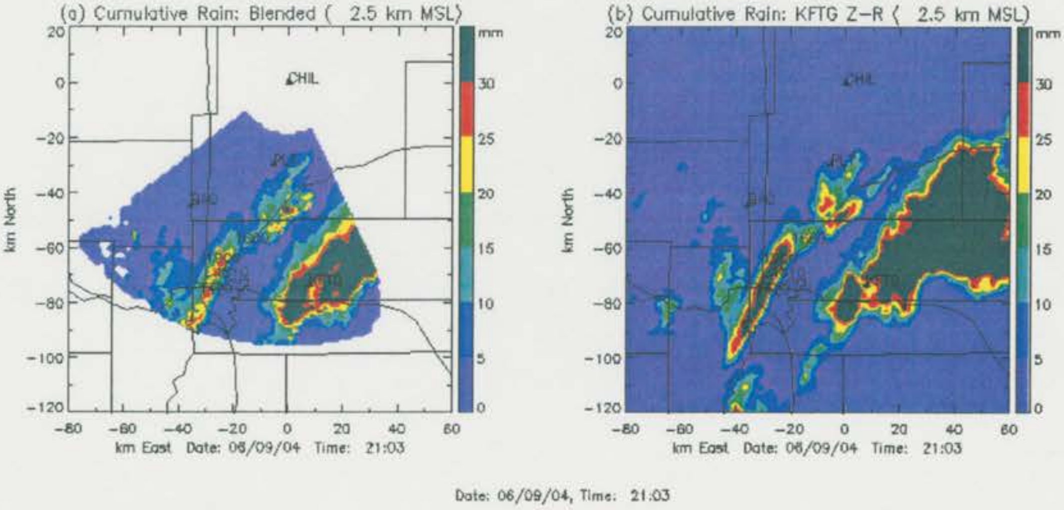

Figure 4.9: Total rain accumulation using the a) CSU blended algorithm and b) the NEXRAD Z-R accumulation between 2100 UTC and 2359 UTC on 09 June 2004. Notice the large accumulations of the Z-R technique relative to the CSU-blended technique, specifically for the western cell. Grid is centered on the CHILL radar.

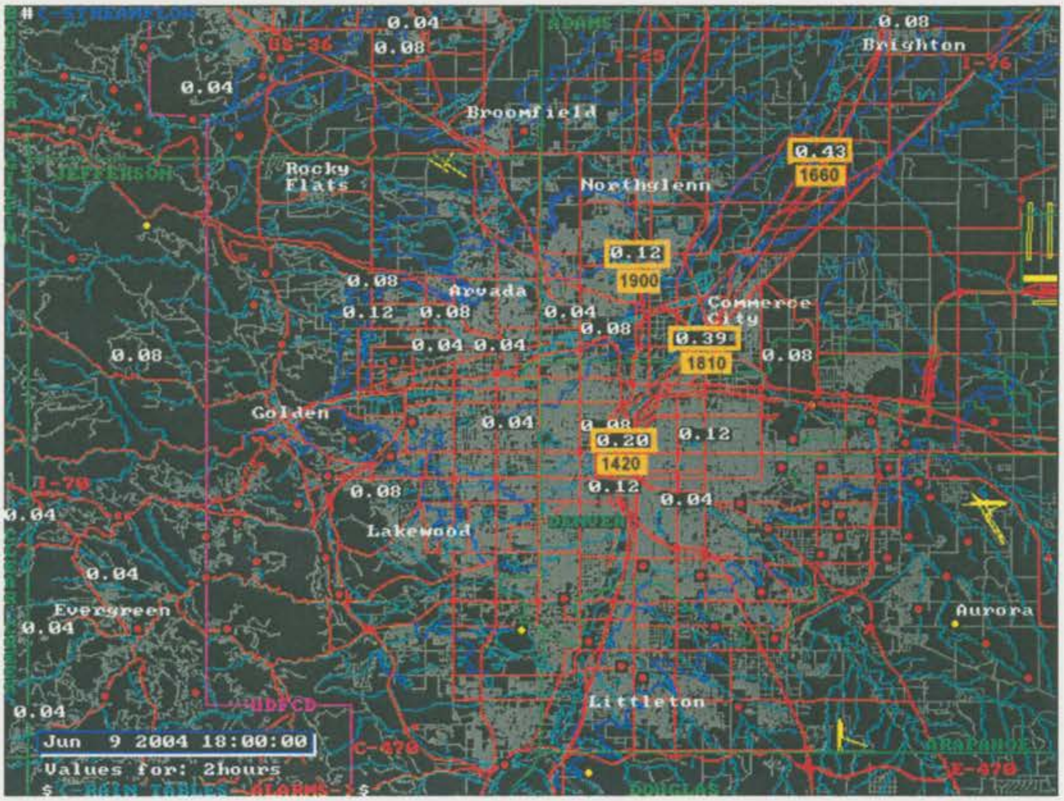

Figure 4.10: The Denver Urban Drainage and Flood Control District (UDFCD) network of rain gauges. Amounts are measured over the 2 hour period from 22-2359 UTC (16-18 LT) 09 June 2004 in inches. The four gauges highlighted in orange are those selected for this study.

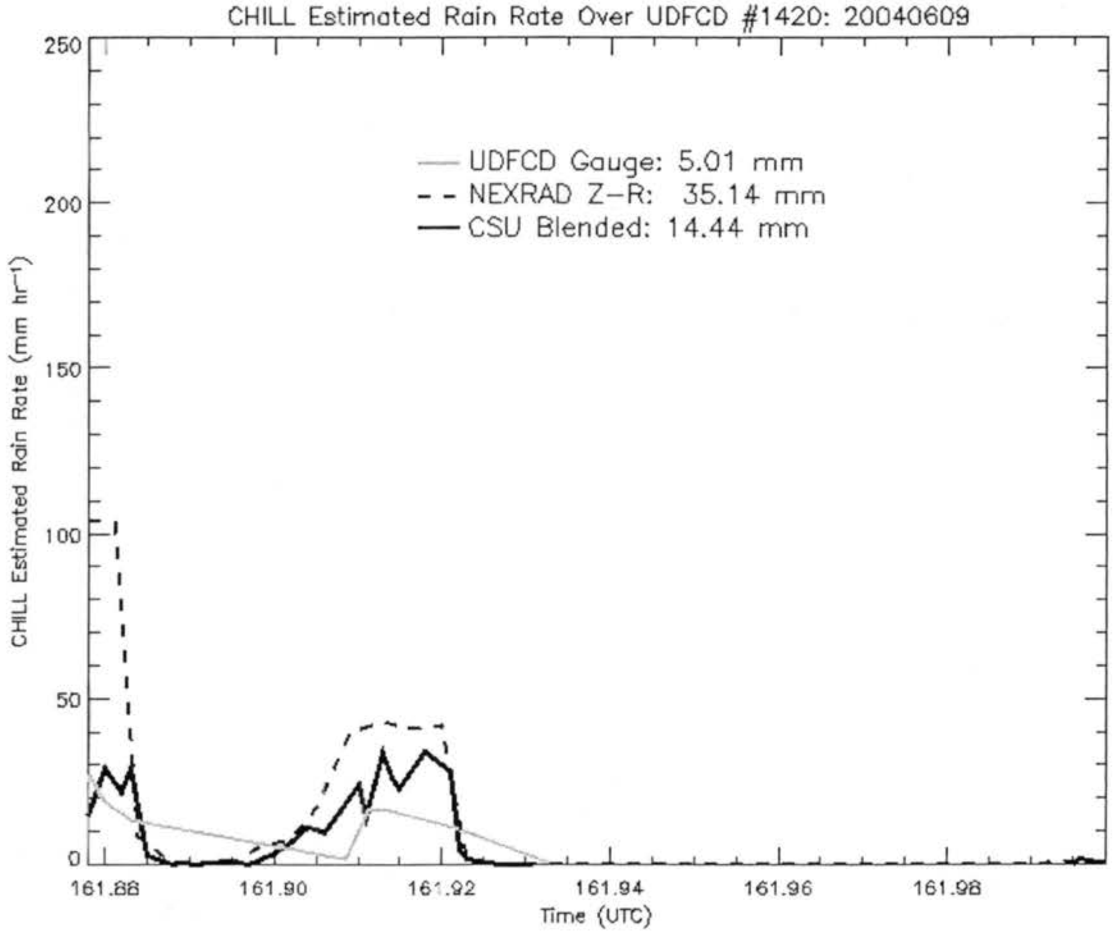

Figure 4.11 Rain rate trace over the UDFCD gauge #1420 on 09 June 2004. CSU blended algorithm is the black solid line, the NEXRAD Z-R relation is the dashed line, and the UDFCD gauge is the gray solid trace. Time is in fraction of a Julian day, beginning at 2100 UTC and ending at 2359 UTC.

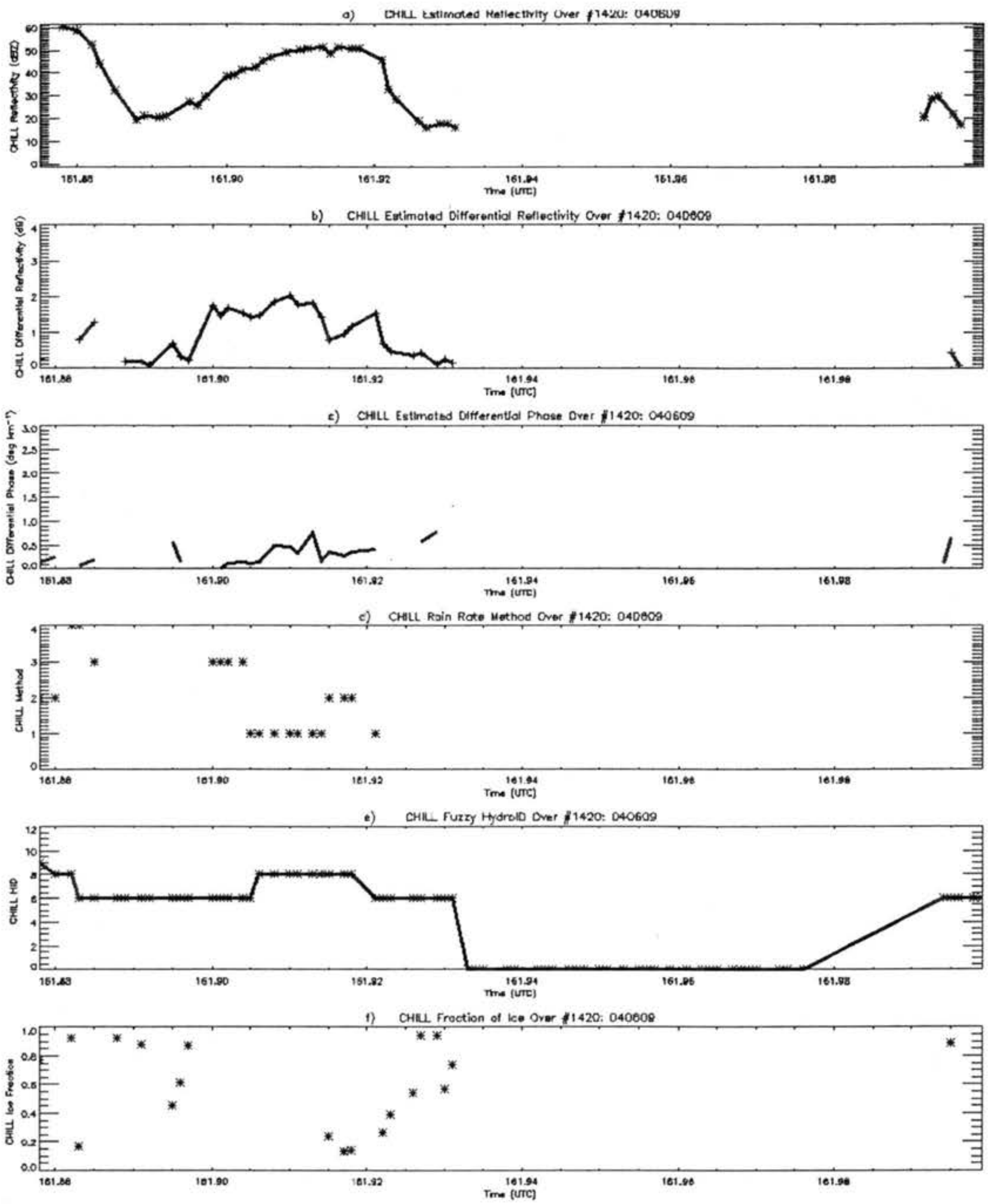

Figure 4.12 Time series of CHILL data on 09 June 2004 over UDFCD gauge #1420 for a) Reflectivity, b) differential reflectivity, c) differential phase, d) blended algorithm rain rate calculation method, e) fuzzy logic hydrometeor type, and f) fraction of ice. The methods correspond to 1=R(K_{dp}, Z_{dr}), 2=R(K_{dp}), 3=R(Z_h, Z_{dr}) and R(Z_h). Hydrometeor types correspond to 0=no data, 1=drizzle, 2=rain, 3=dry snow, 4=wet snow, 5=vertical ice, 6=dry graupel, 7=wet graupel, 8=small hail, 9=large hail, 10=small hail mixed with rain, and 11=large hail mixed with rain. Time is in fraction of a Julian day, beginning at 2100 UTC and ending at 2359 UTC.

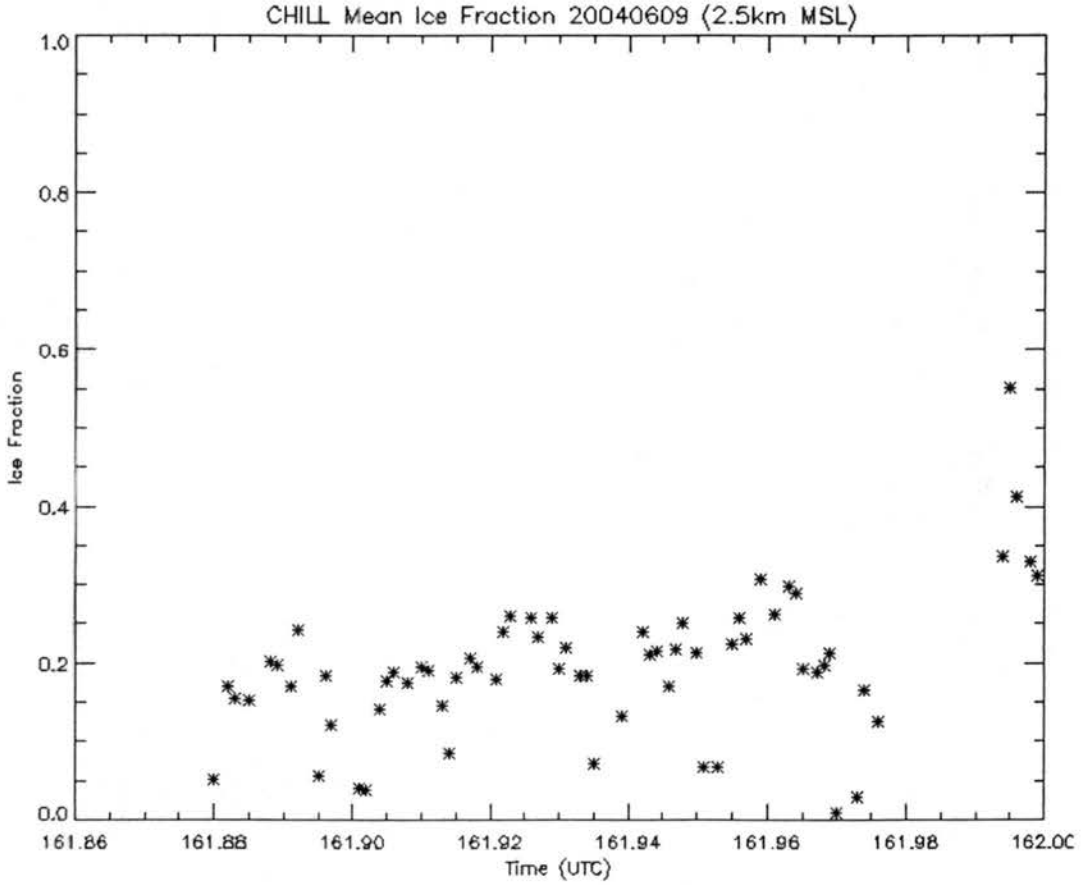

Figure 4.13: Total ice fraction in the xy-grid domain for 09 June 2004.

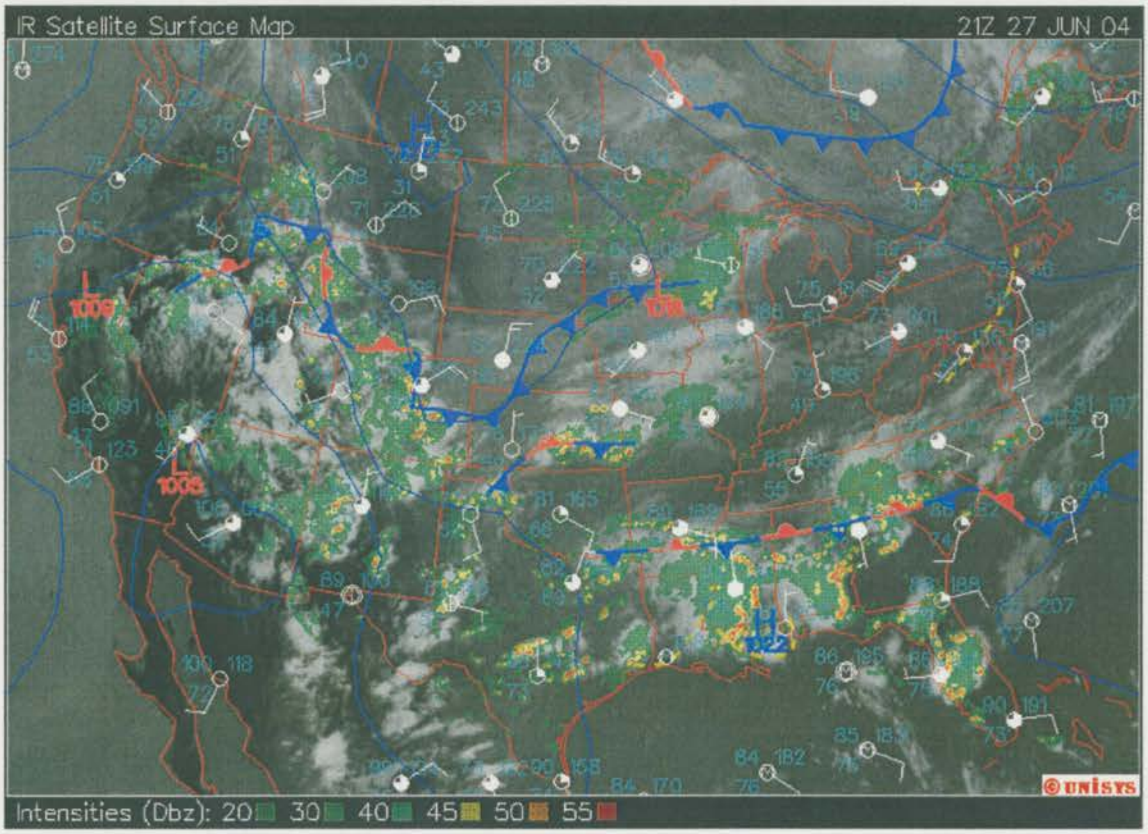

Figure 4.14: Infrared satellite, radar, and surface composite for 21 UTC on 27 June 2004. (Image from http://weather.unisys.com).

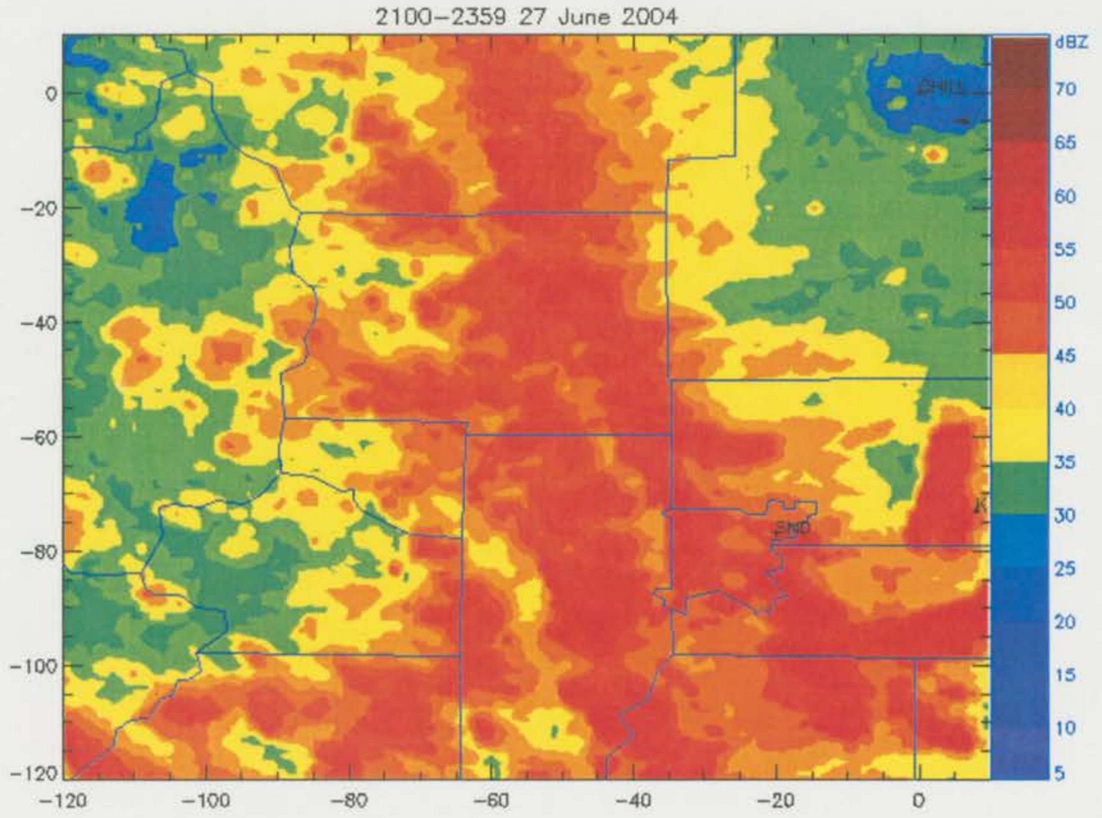

Figure 4.15: Storm swath for storms occurring between 2100 and 2359 UTC on 27 June 2004. The storm swath was calculated by taking the maximum reflectivity from all levels at each xy-grid point over the 3 hour time period. The grid is centered on the CHILL radar, and the 'SND' denotes the location of the Denver sounding station.

a)

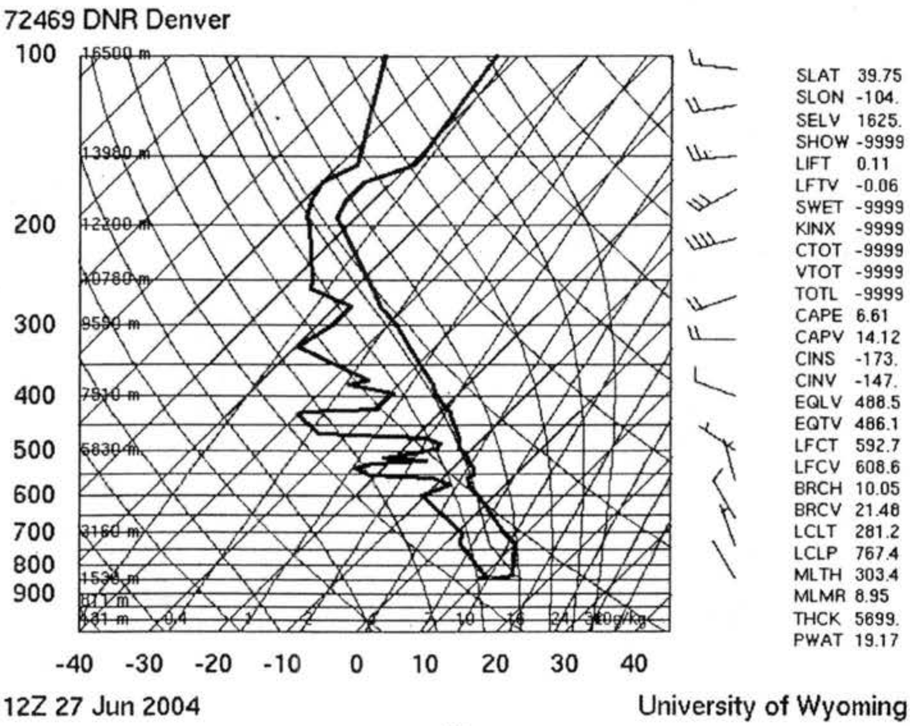

b)

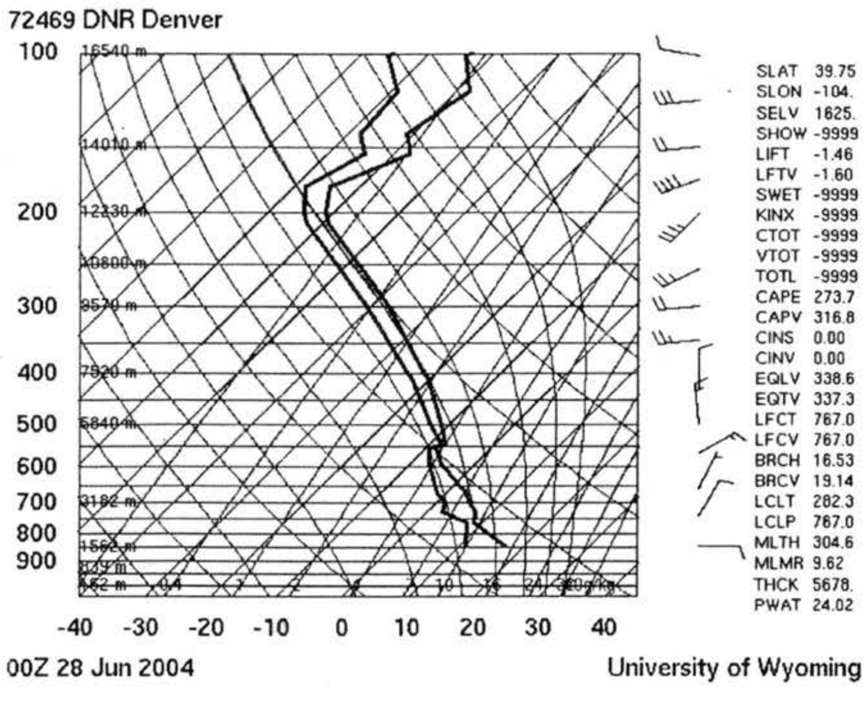

Figure 4.16: Denver Sounding from a) 12 UTC on 09 June 2004 and b) 0 UTC on 10 June 2004. (Image generated from http://weather.uwyo.edu/upperair/sounding.html).

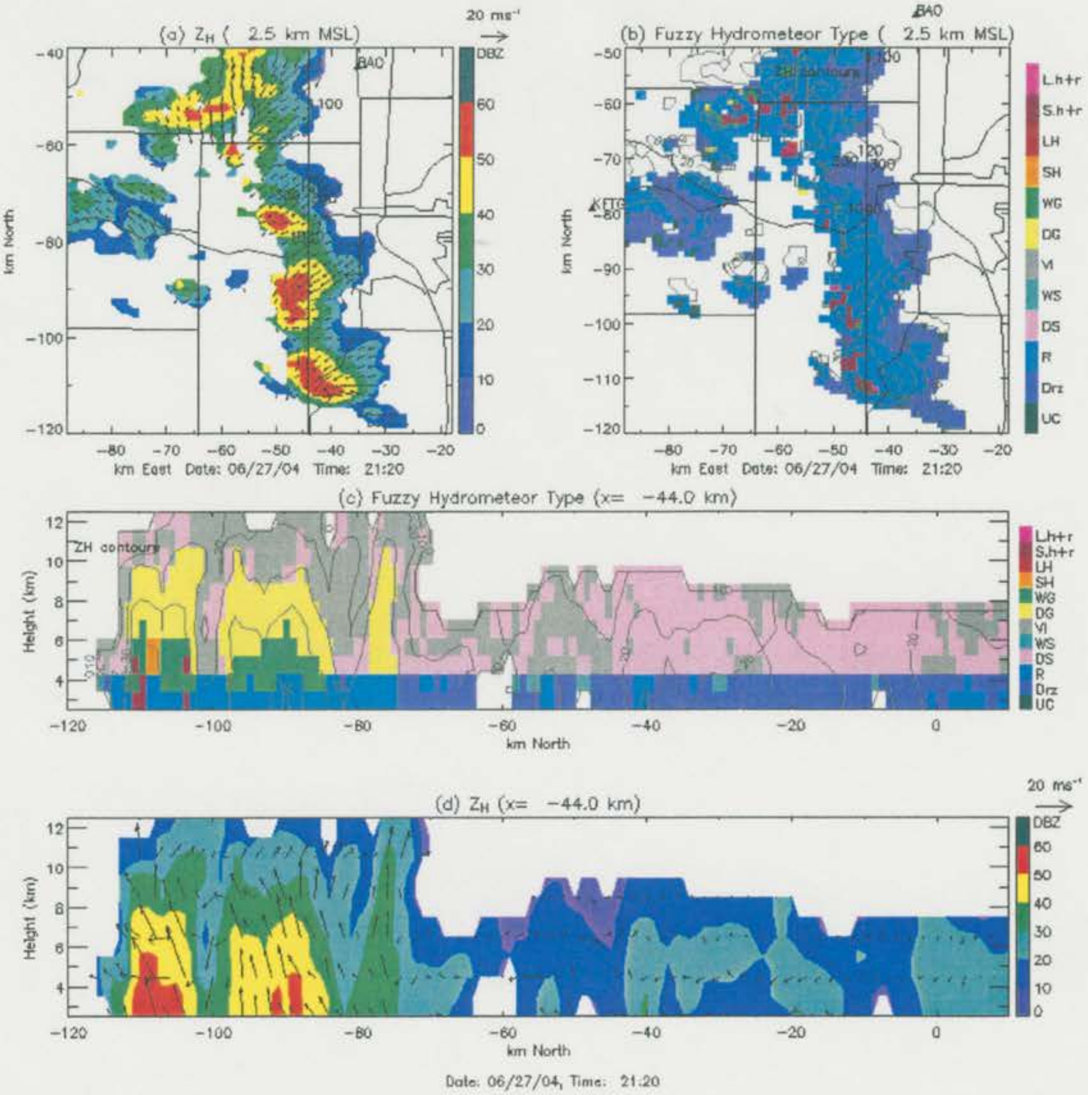

Figure 4.17: Algorithm analysis and display from 2229 UTC on 27 June 2004. Grid origin is located at the CHILL radar. Panels show a) CHILL reflectivity at 2.5 km MSL with dual-Doppler winds (black arrows), b) Hydrometeor type identified by the fuzzy logic algorithm with grey contours corresponding to CHILL reflectivities at 2.5 km MSL, c) vertical cross-section of hydrometeor type at x=-44.0 km with gray contours indicating the corresponding CHILL reflectivity, and d) vertical cross section of CHILL reflectivity with dual-Doppler derived vertical winds at x=-44.0 km.

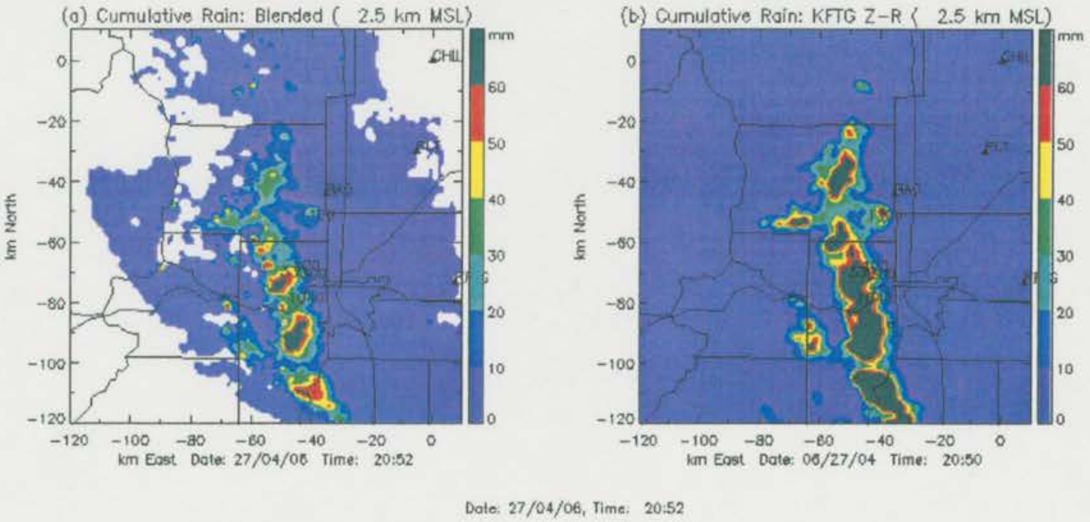

Figure 4.18: Total rain accumulation using the a) CSU blended algorithm and b) the NEXRAD Z-R accumulation between 2050 UTC and 2359 UTC on 27 June 2004. Grid is centered on the CHILL radar.

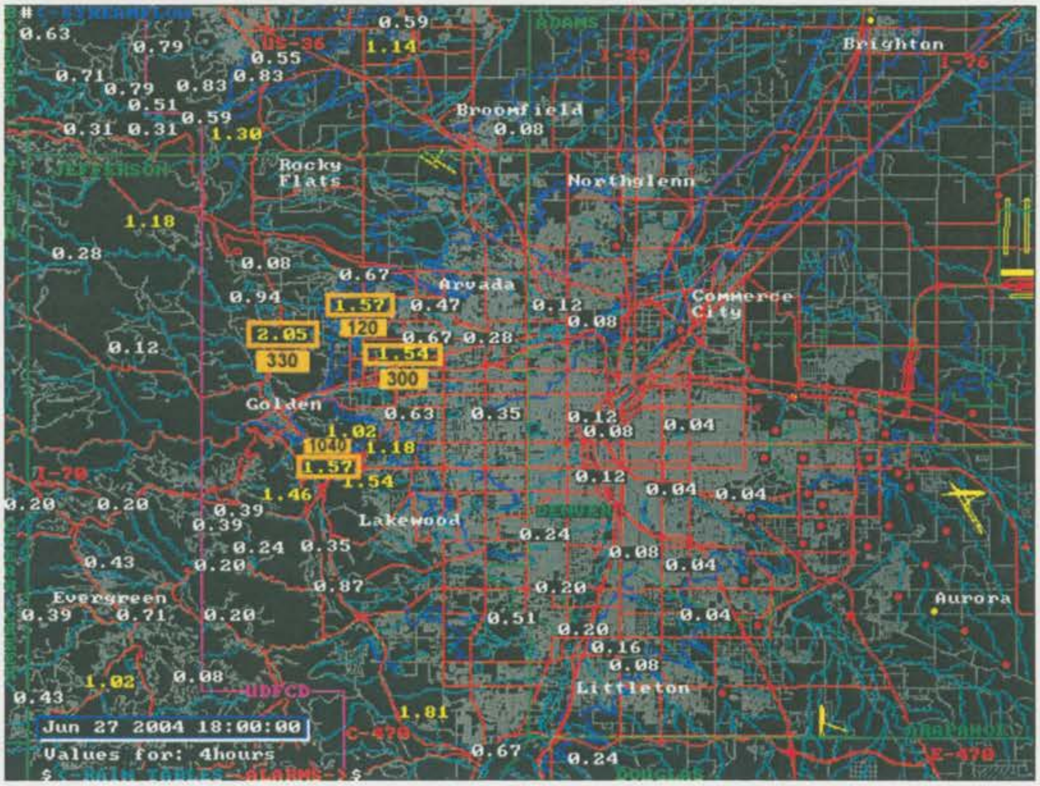

Figure 4.19: Rainfall totals for 4 hour period beginning at 2000 UTC (1400 LT) on 27 June 2004 from the Denver UDFCD gauge network. Stations selected for the study are highlighted in orange.

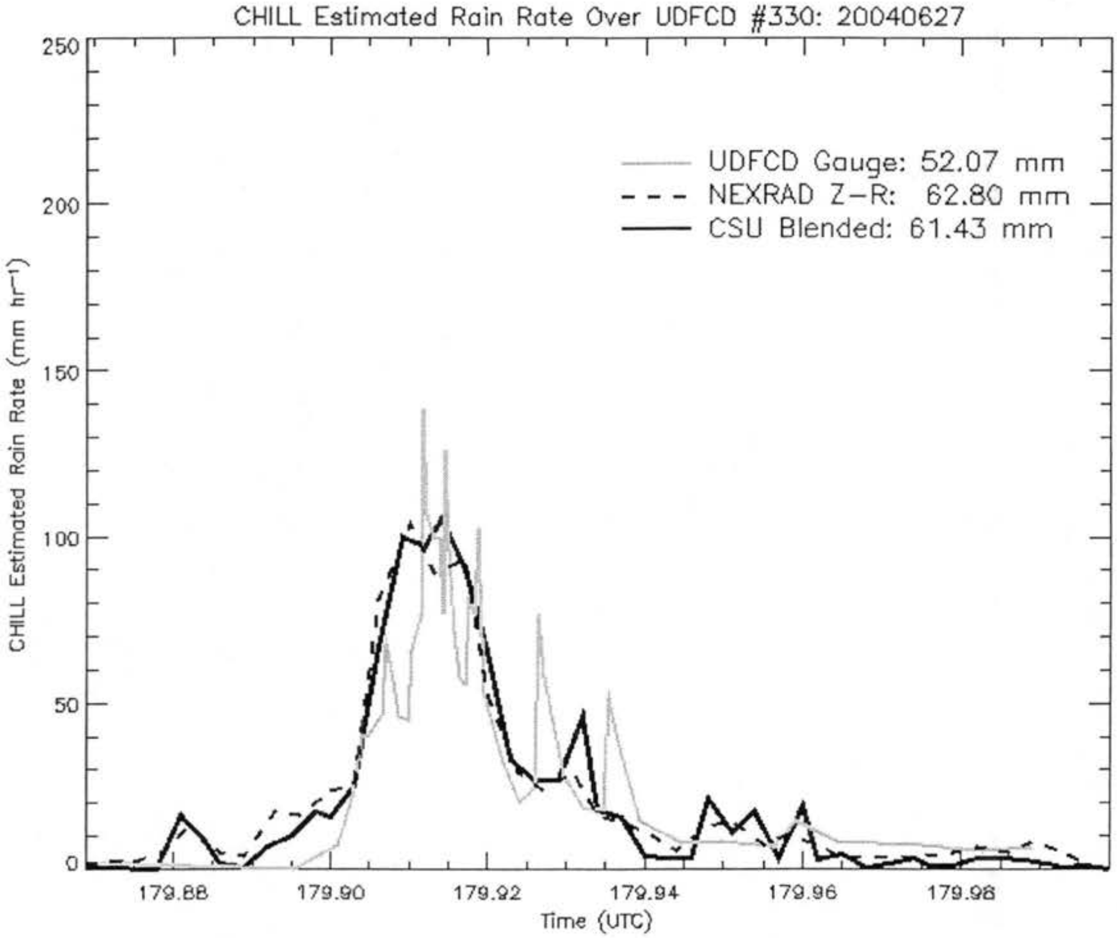

Figure 4.20: Rain rate trace over gauge #330 on 27 June 2004 between 2100 UTC and 2359 UTC. The dashed line is the NEXRAD Z-R, gray solid line is the UDFCD gauge trace, and the black solid line is the CSU blended technique. Time is in fraction of a Julian day, beginning at 2100 UTC and ending at 2359 UTC.

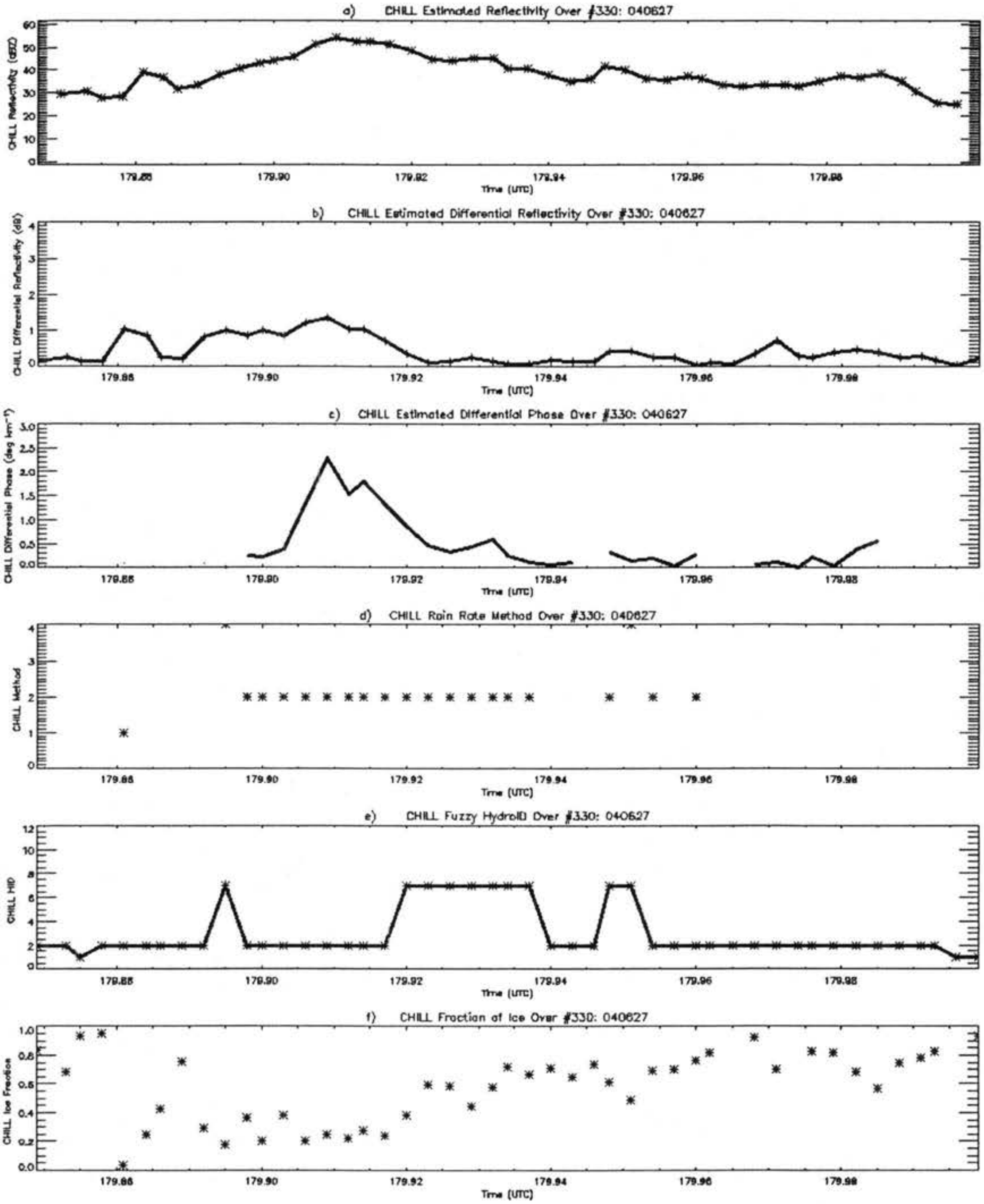

Figure 4.21 Time series of CHILL data on 27 June 2004 over UDFCD gauge #330 for a) Reflectivity, b) differential reflectivity, c) differential phase, d) blended algorithm rain rate calculation method, e) fuzzy logic hydrometeor type, and f) fraction of ice. The methods correspond to 1=R(K_{dp}, Z_{dr}), 2=R(K_{dp}), 3=R(Z_h, Z_{dr}) and R(Z_h). Hydrometeor types correspond to 0=no data, 1=drizzle, 2=rain, 3=dry snow, 4=wet snow, 5=vertical ice, 6=dry graupel, 7=wet graupel, 8=small hail, 9=large hail, 10=small hail mixed with rain, and 11=large hail mixed with rain. Time is in fraction of a Julian day, beginning at 2100 UTC and ending at 2359 UTC.

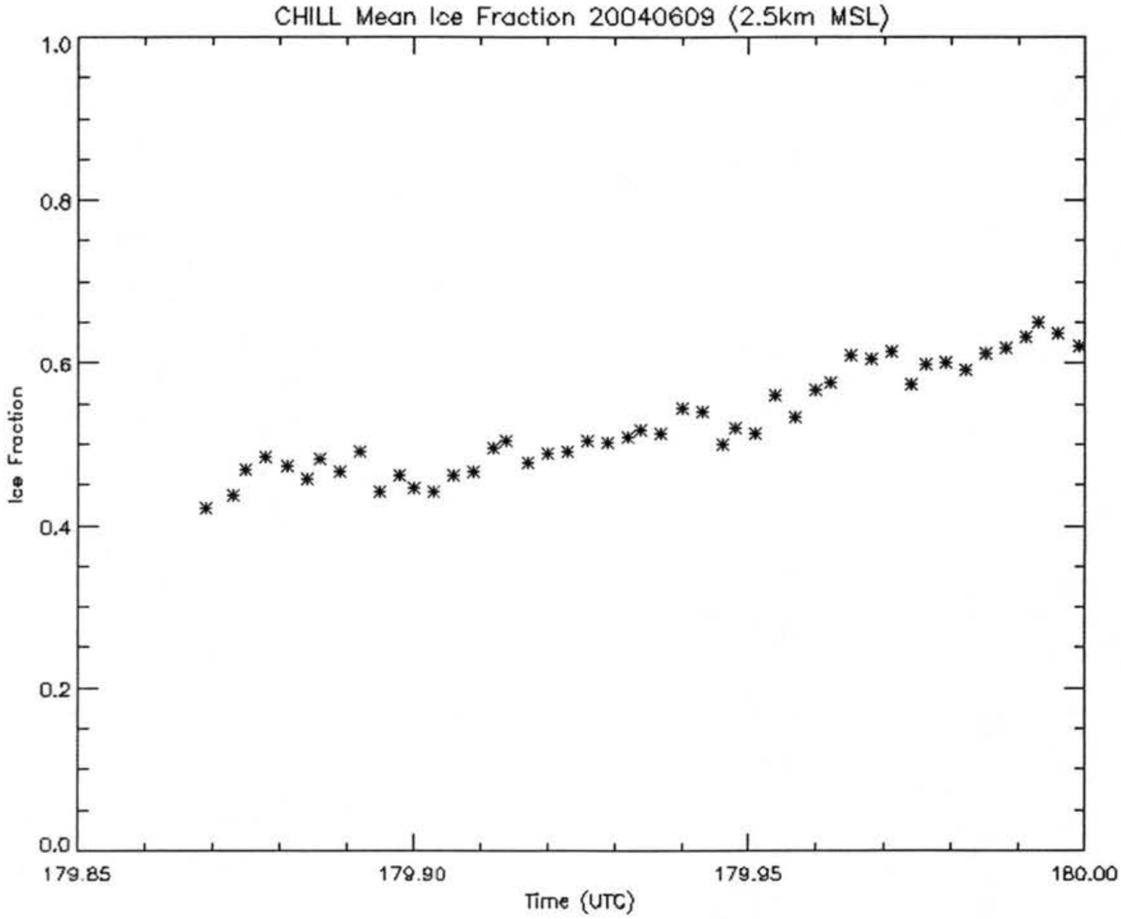

Figure 4.22: Total ice fraction in the xy-grid domain for 27 June 2004.

Table 4.1: Total rainfall accumulations in mm for the KFTG and CHILL radar estimates and the UDFCD rain gauges for the period 2100-2359 UTC on 09 June 2004. Negative indicates an underestimate of the radar compared to the rain gauge.

Gauge #	NEXRAD	UDFCD	CHILL	CHILL-UDFCD	NEXRAD-UDFCD	CHILL-NEXRAD
1900	14.32	3.05	10.97	7.92	11.27	-3.35
1420	35.14	5.08	14.44	9.36	30.06	-20.70
1810	35.23	9.91	22.23	12.32	25.32	-13.0
1660	10.92	26.56	14.55	-12.01	-15.64	3.63

Table 4.2: Total rainfall accumulations in mm for the KFTG and CHILL radar estimates and the UDFCD rain gauges for the period 2100-2359 UTC on 27 June 2004. Negative indicates an underestimate of the radar compared to the rain gauge.

Gauge #	NEXRAD	UDFCD	CHILL	CHILL-UDFCD	NEXRAD-UDFCD	CHILL-NEXRAD
300	38.05	39.12	31.12	-8.0	-1.07	-6.93
330	62.80	52.07	61.43	9.36	10.73	-1.37
1040	32.34	38.1	30.69	-7.41	-5.76	-1.66
120	39.88	53.03	47.18	-5.85	-13.15	7.30

CHAPTER 5

Conclusions and Future Work

5.1 Conclusions

Radars have been used for decades to observe precipitation and other weather phenomena. Advancements such as Doppler and dual-polarization capabilities have greatly increased the amount of information that can be retrieved for scientific insights about storms. Over the years, scientists have continued to develop new ways of combining radar data from multiple radars, as well as other observing platforms, to achieve efficient and insightful methods of viewing the vast amount of data in real-time. The Cooperative Convective Precipitation Experiment in 1981 involved eight radars, 14 research aircraft, mesonet stations and upper-air sounding sites to achieve ten broad scientific goals. This field project was deemed successful partly due to the cooperation and direction of the Sunday Creek operations center whose primary goal was to coordinate, operate, and guide the numerous instruments involved in the project. The Severe Environmental Storms and Mesoscale Experiment (SESAME) in 1979 provided unique dual-Doppler observations of a tornado. At the time, quality dual-Doppler datasets that could be used for the testing of hypotheses were rare. Many different platforms for observing the atmosphere were integrated during the Oklahoma-Kansas

Preliminary Regional Experiment for STORM (PRE-STORM) program in 1985. The field experiment included rawinsondes, surveillance radars, Doppler radars, wind profilers, several aircraft, and satellite products. Real-time color displays of Doppler radar data were used to determine flow characteristics in MCSs. Hydrometeor identification using polarimetric measurements has become available during various field projects in recent years, adding to the data available for microphysical characteristics. Most recently, real-time dual-Doppler winds were available during the Mesoscale Alpine Programme (MAP) in 1999. The winds, combined with real-time hydrometeor identification, were important in determining the precipitation and airflow structure to direct aircraft in the complex terrain of northern Italy. In general though, having multiple platforms available for field projects also presents significant challenges to studying and analyzing the data in real-time to guide field operations.

Motivated by what has been available in previous projects described above, the goal of this thesis was to design and test a real-time analysis and display tool for the four radars along the Colorado front range. The analysis tool combined reflectivity and velocity data from CSU-CHILL, PAWNEE, and the KCYS and KFTG WSR-88D radars, as well as the polarimetric data provided by CSU-CHILL, to derive products such as hydrometeor identification, rain rate, total rainfall, and wind field in real-time in a common, user-friendly display format.

The algorithm and display were tested during the summer of 2004 at the CSU-CHILL facility, coincident with the Global Precipitation Measurement mission Front Range Pilot Project. Though the PAWNEE radar was not operational, the other three front range radars were used to successfully test the analysis algorithm and display in real-time under field project conditions. Derived products were available within 15 minutes after the beginning of the radar volume scan, with CHILL data being the most 'real-time', as it was available within three minutes of a scan volume. Dual-Doppler winds took the longest to acquire (15 minutes after the WSR-88D volume scan), in part due to the time required to download the large files from Unisys' Local Data Manager. The data supplied by the NEXRAD WSR-88D radars supplemented CHILL data, giving scientists a larger view of storms while still meeting the scientific goals of the GPM project. Although the data were not real-time in an instantaneous sense, it still provided important information for characterizing storms throughout their lifetime. The suite of radar products on the interactive display tool allowed the scientist to visualize updraft locations and strengths, determine hydrometeor types present at both the surface and upper-levels of the storm, and identify characteristics in the wind field such as mesocyclones. Comparisons could also be made between radars, revealing differences in the rain rate estimation techniques used by CHILL and WSR-88D.

National Weather Service forecasters will also profit from the accessibility of real-time products via the Internet. Forecasters from the Boulder office have already expressed interest in the continuing availability of rain rate and total rainfall accumulation images (C. Gimmestad, personal communication, 2004).

This study found that a real-time analysis and display tool proved a valuable resource for analyzing and visualizing copious amounts of data from several radars succinctly and efficiently. The software developed for this project provided scientists with numerous options to process and view data from Doppler and polarimetric radars without requiring prior knowledge of the intricacies related to the interpretation of radial velocity and polarimetric variables. Future field experiments, especially those in which a primary objective of CHILL is to direct aircraft, will greatly benefit from such a software tool.

5.2 Future Work

Future work needs to be done in three major areas: 1) improvements to the software algorithm in terms of both the functionality and the processing, 2) continued testing in the field, and 3) portability to other radar networks.

There has already been feedback regarding improvements that can be made to the functionality of the algorithm and display tool. It was apparent during the field testing phase that a loop of the last hour of data would be a useful addition to assist in the analysis of storm development and motion. In terms of the user interface, interest in satellite and surface data overlays has been expressed, as well as lightning data and possibly rain gauge data from the UDFCD network. With respect to the processing of data, a storm tracking algorithm similar to that used by the National Weather Service would be a better method for determining storm advection information for dual-Doppler analysis. The melting level could be determined using the radar data instead of the local sounding, resulting in better estimates of the actual environment present in the storm. A stratiform and convective partitioning algorithm could be useful in hydrometeor identification to assist in the elimination of unlikely hydrometeor types under certain conditions, and could also be useful in viewing real-time data. Additionally, software could be implemented to process the real-time dual-Doppler winds to look for Tornado Vortex Signatures (TVS) or detect circulation or convergence in the wind field. Personal communications with some of the Boulder office NWS forecasters yielded suggestions to mimic their displays with accumulated precipitation and horizontal slices of precipitation type with the ability to toggle and/or overlay them with a loop of reflectivity and radial velocity (C. Gimmestad, personal communication, 2004). Future versions of the software should have better integration between the display and analysis tools, providing the user with more input into the processing of the real-time data. For example, the user could change the technique used for determining the vertical wind component of the dual-Doppler synthesis. Or the user could change the grid size and resolution from the display tool.

Future work needs to be done to improve the 'real-time' of the data output. Since the LDM was the bottleneck in the real-time processing, eliminating the number of servers on the LDM before data reaches the CSU-CHILL radar facility could decrease the time needed to download WSR-88D files from the network. Since the most time-consuming computer process is associated with the interpolation of radar data to a Cartesian grid, new methods for interpolation could improve the time spent in this step of the analysis.

Further field testing with emphasis on the KCYS and PAWNEE radars needs to be completed in order to illustrate the full functionality of the algorithms and display. This can be done as soon as the PAWNEE radar is functional again and a data link between CSU-CHILL and PAWNEE has been established. Additionally, testing during a field project involving aircraft would assist in determining what features may or may not be necessary.

Finally, with a few modifications, the analysis and display could be ported to other radar networks, specifically those that use data from WSR-88D's to supplement data collected by a polarimetric radar. Work has already begun setting up the algorithm for the University of Alabama-Huntsville Advanced Radar for Meteorological and Operational Research (ARMOR) and the NWS KHTX WSR-88D radar.

Appendix

A. *Fuzzy Logic Membership Beta Functions*

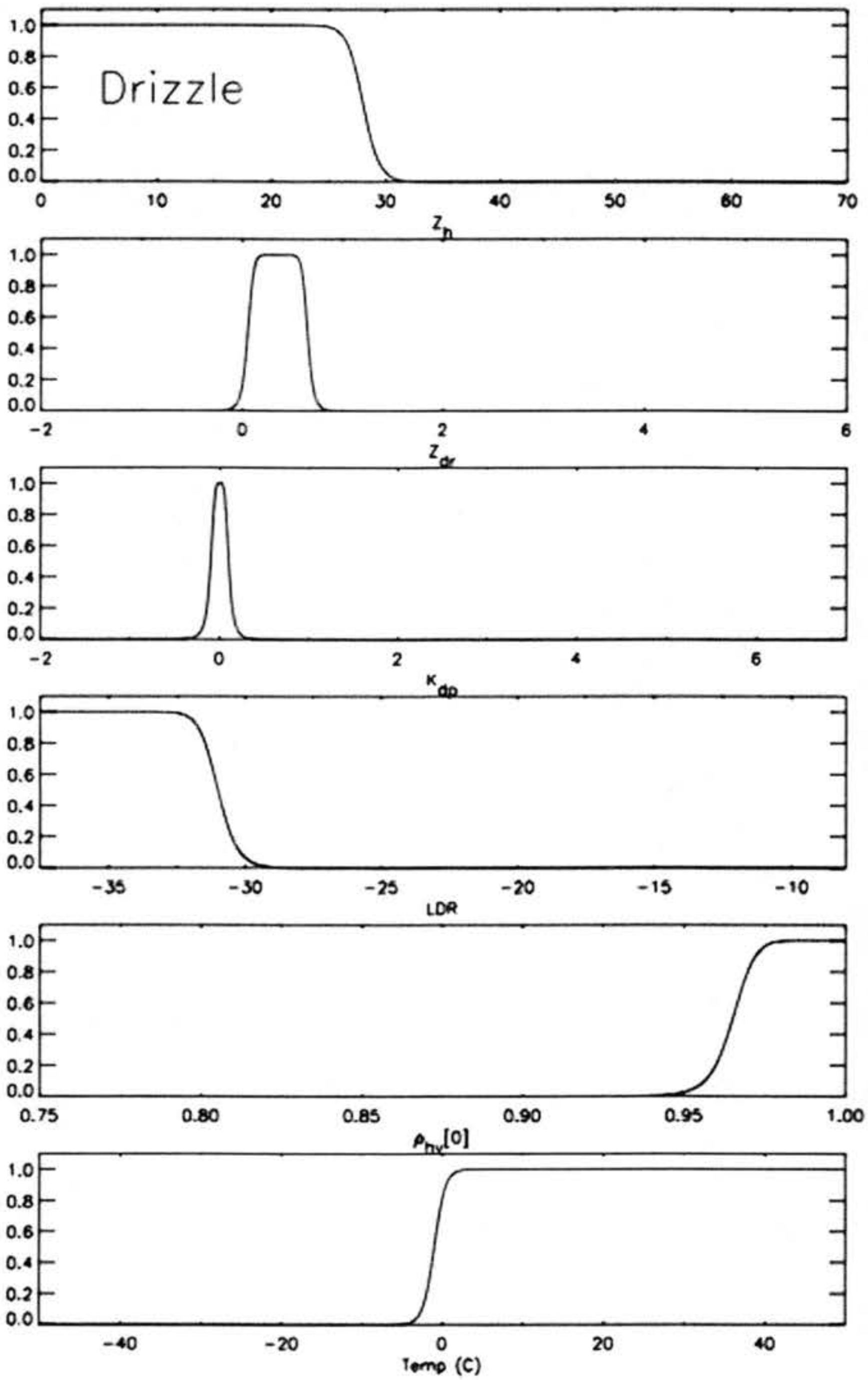

Figure A.1: Fuzzy logic Membership Beta Function (MBF) for Drizzle.

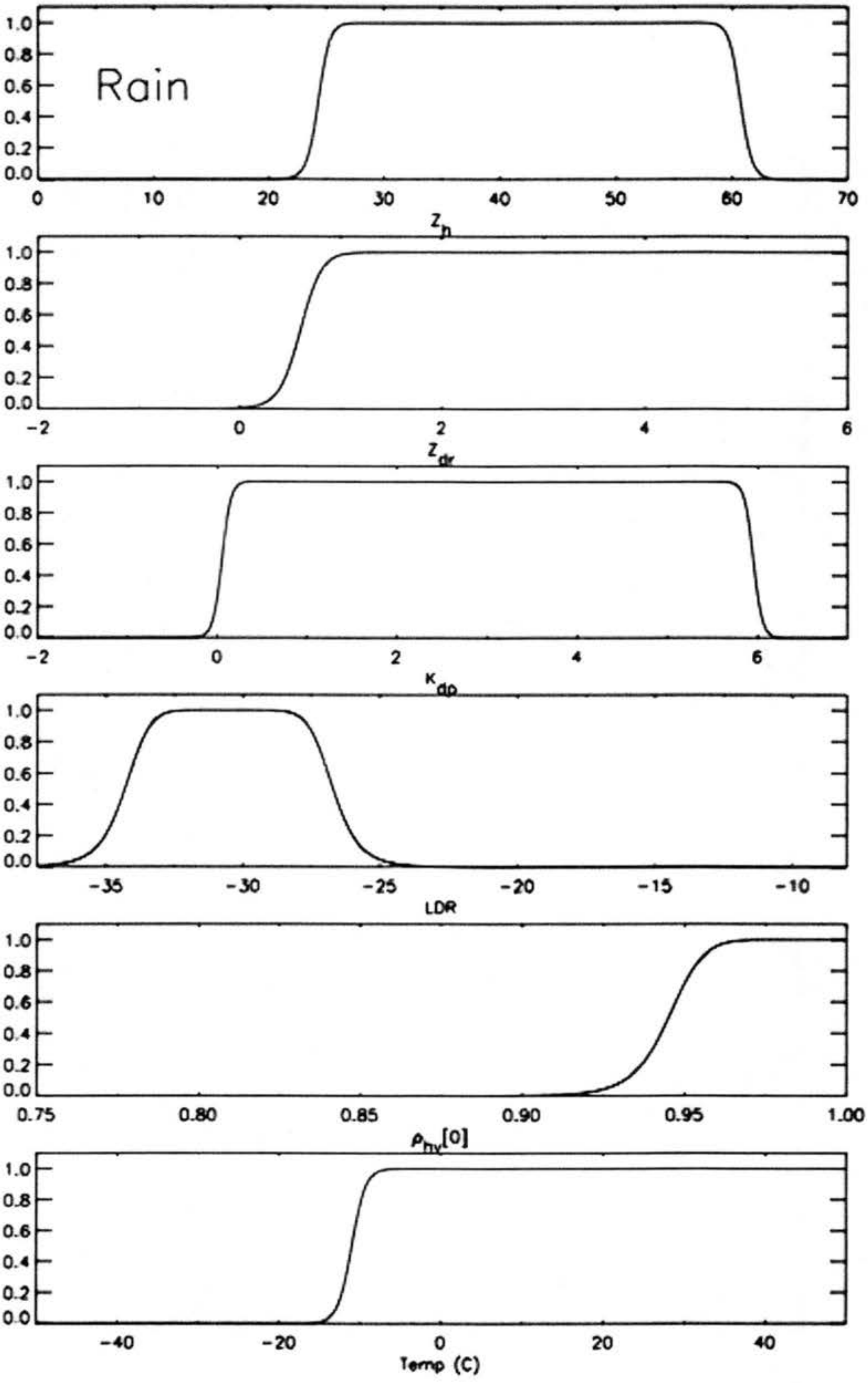

Figure A.2: Fuzzy logic MBF for Rain.

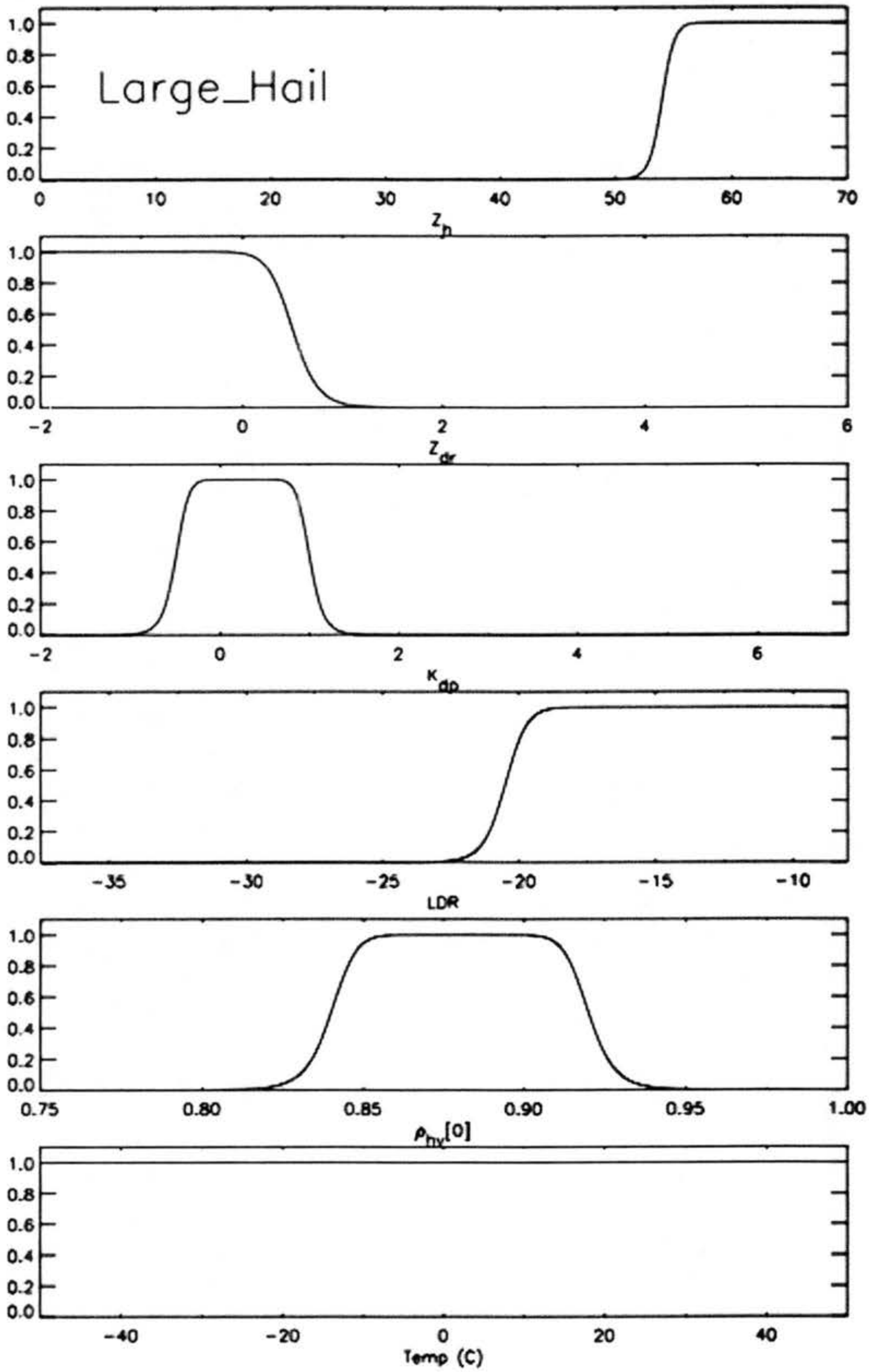

Figure A.3: Fuzzy logic MBF for Large Hail.

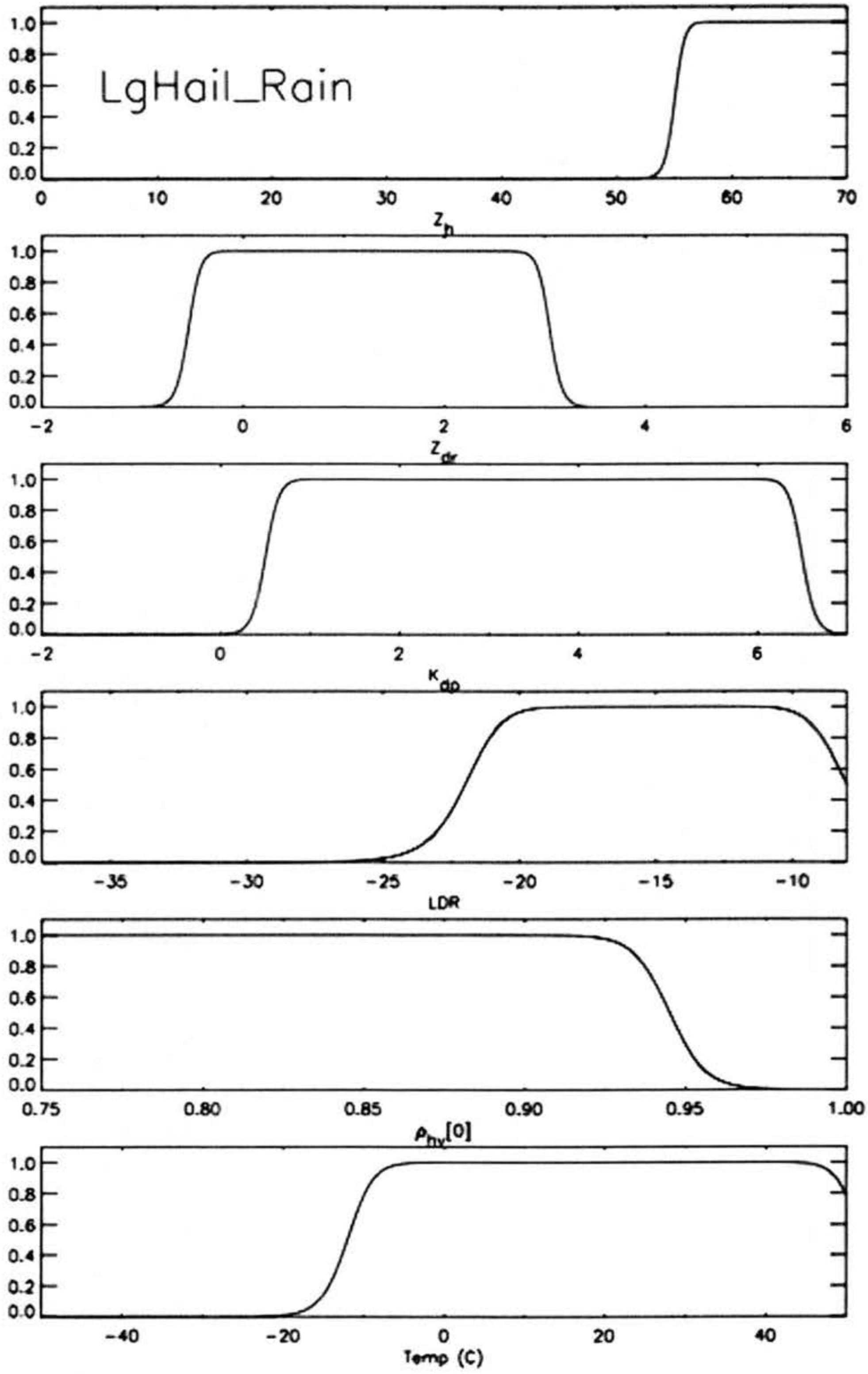

Figure A.4: Fuzzy logic MBF for Large Hail mixed with Rain.

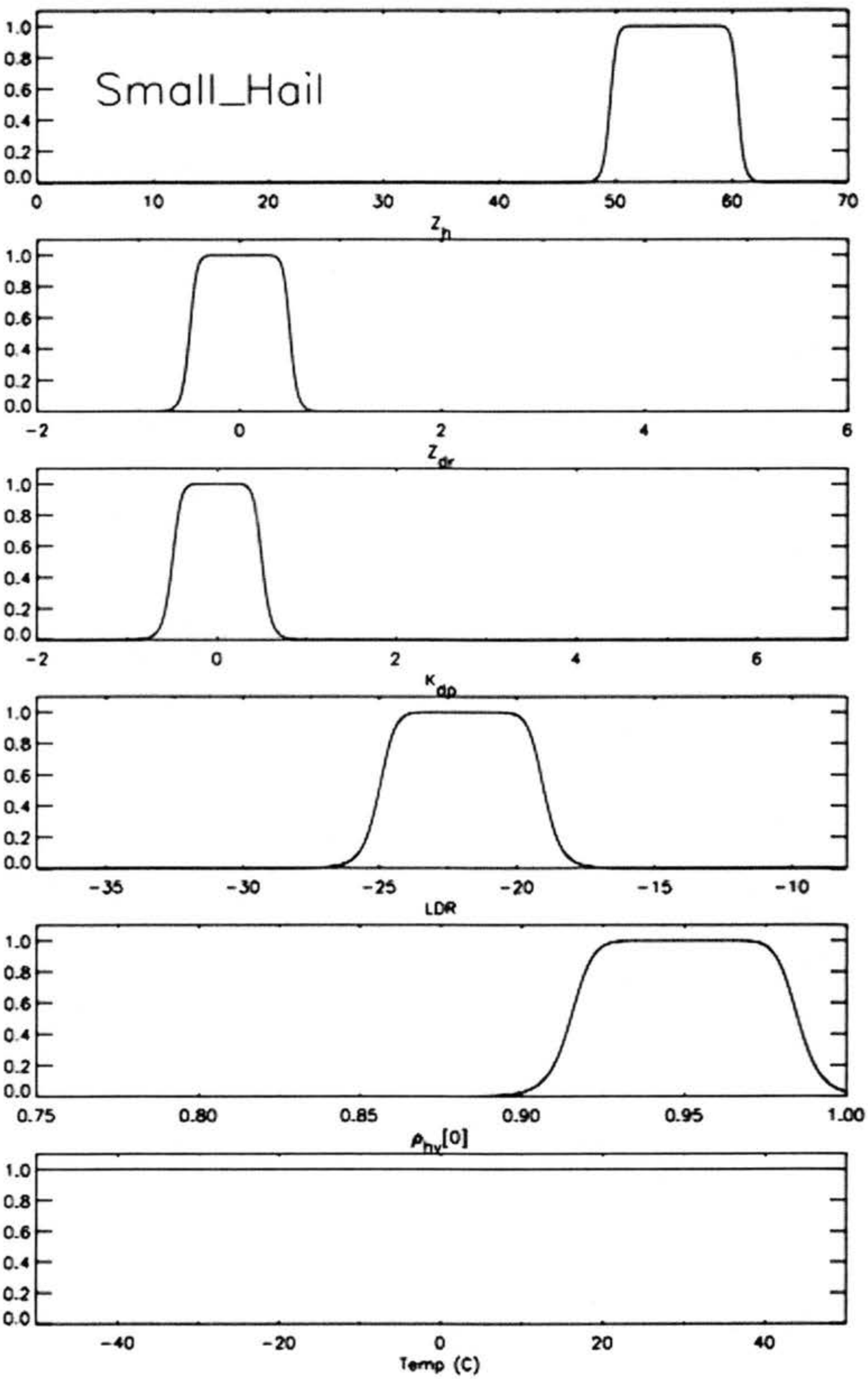

Figure A.5: Fuzzy logic MBF for Small Hail.

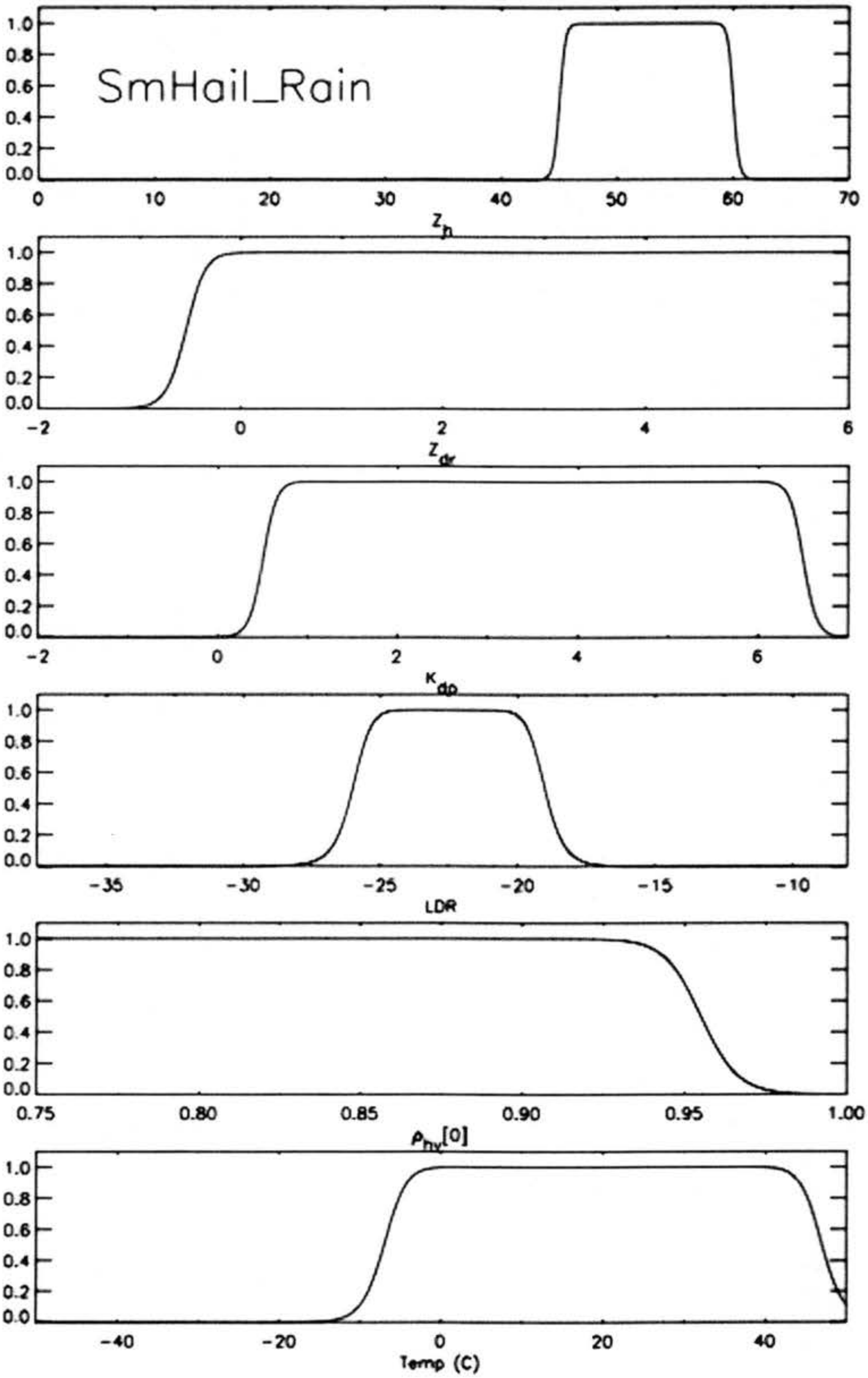

Figure A.6: Fuzzy logic MBF for Small Hail mixed with Rain.

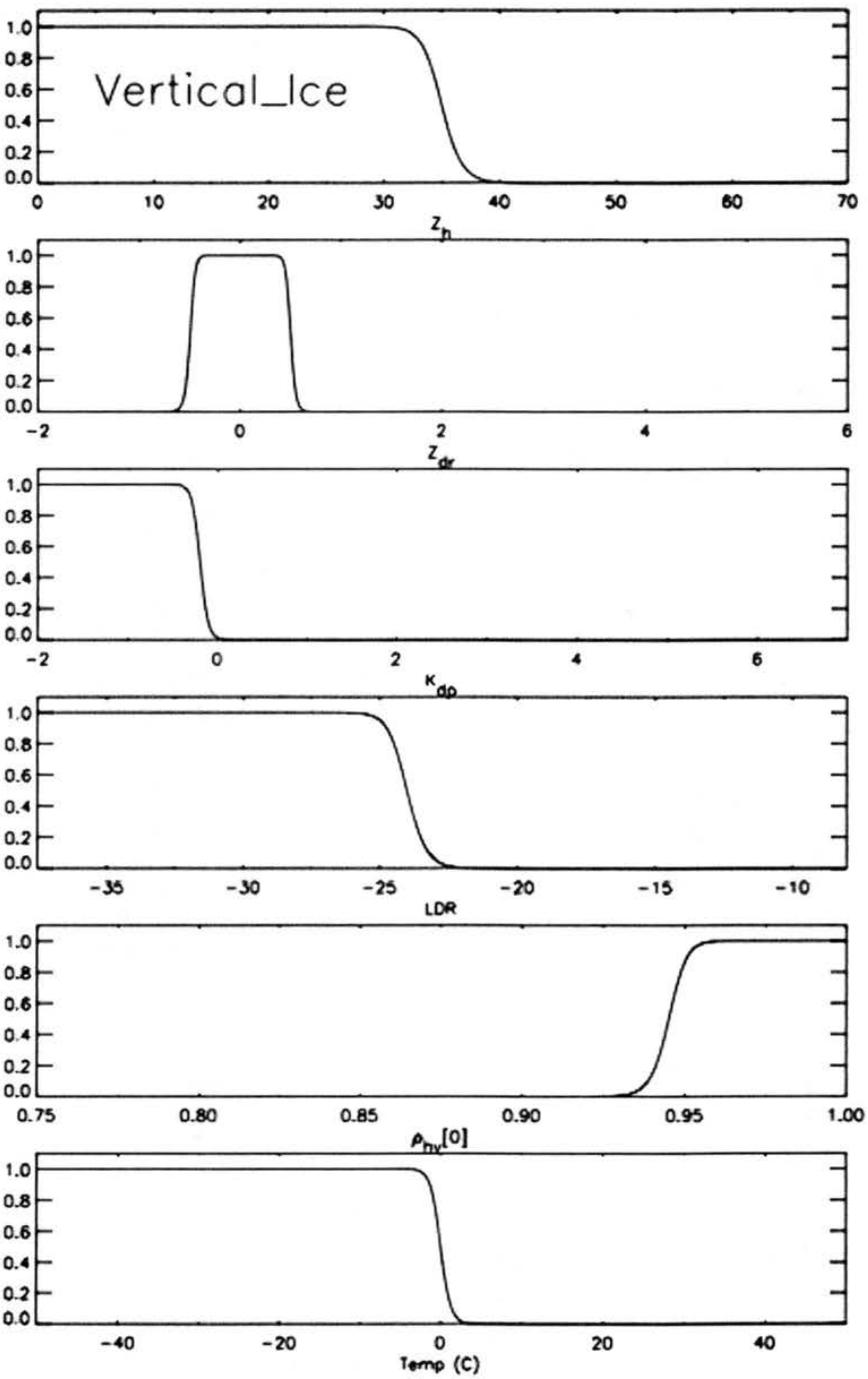

Figure A.7: Fuzzy logic MBF for Vertical Ice.

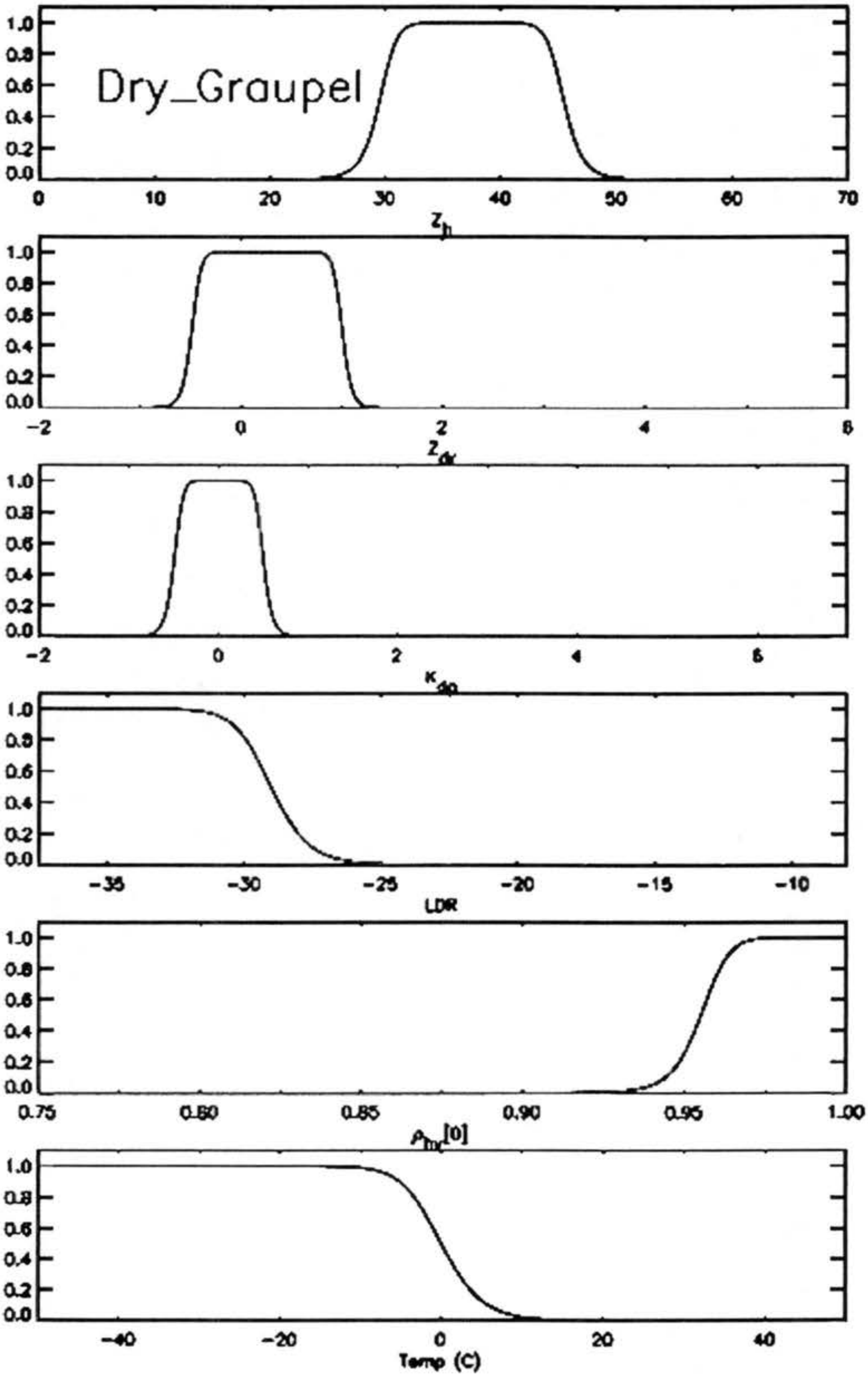

Figure A.8: Fuzzy logic MBF for Dry Graupel.

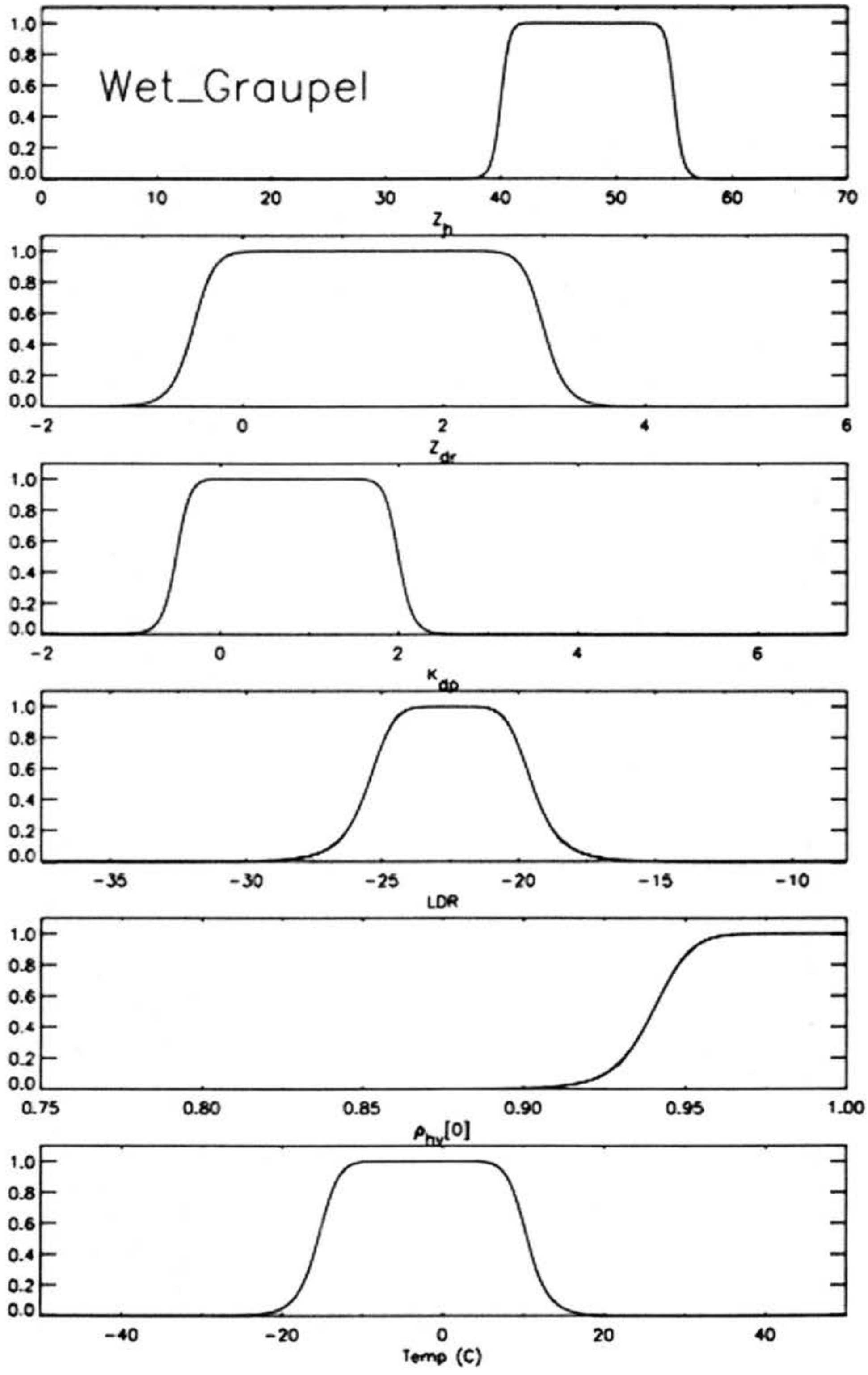

Figure A.9: Fuzzy logic MBF for Wet Graupel.

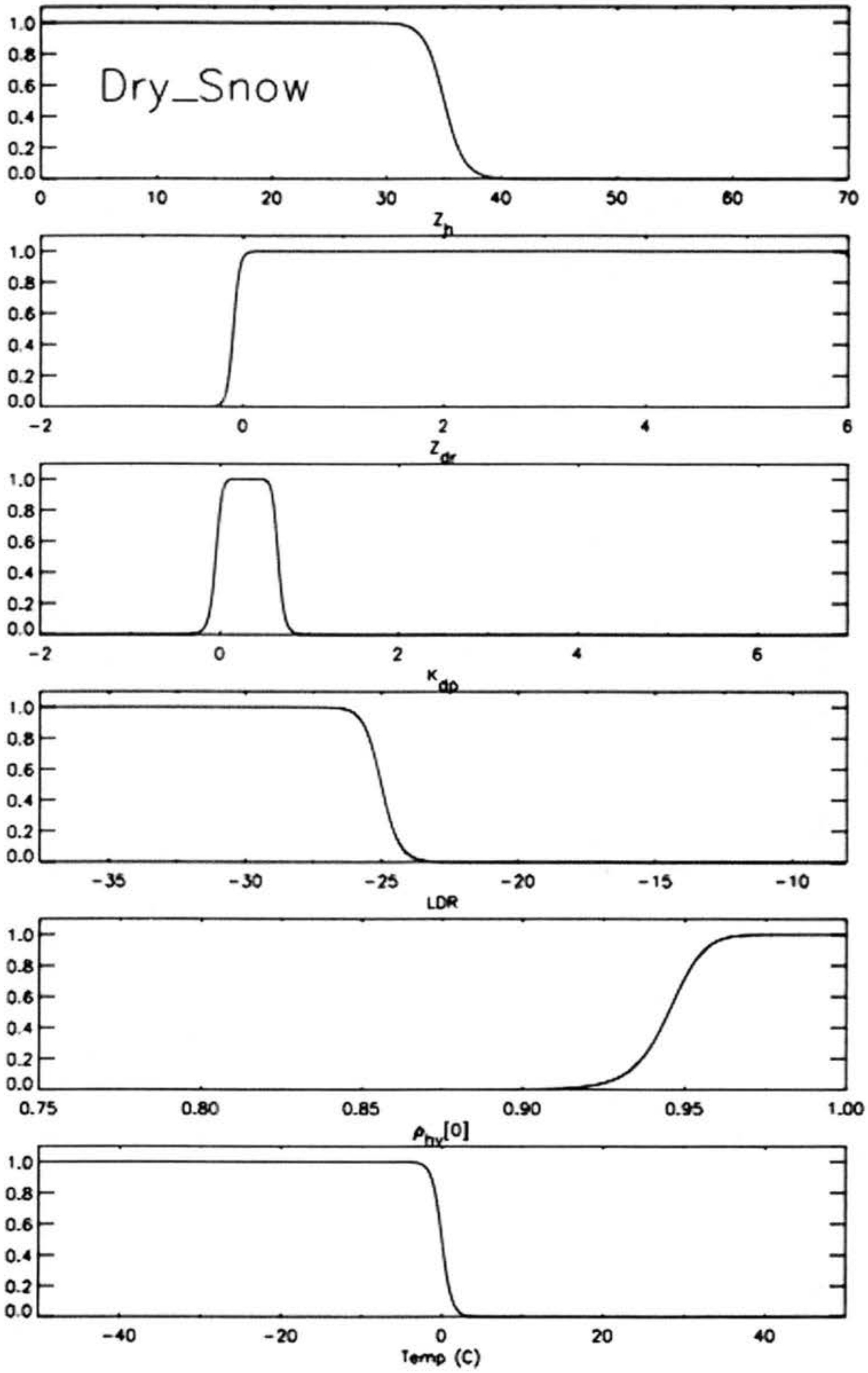

Figure A.10: Fuzzy logic MBF for Dry Snow.

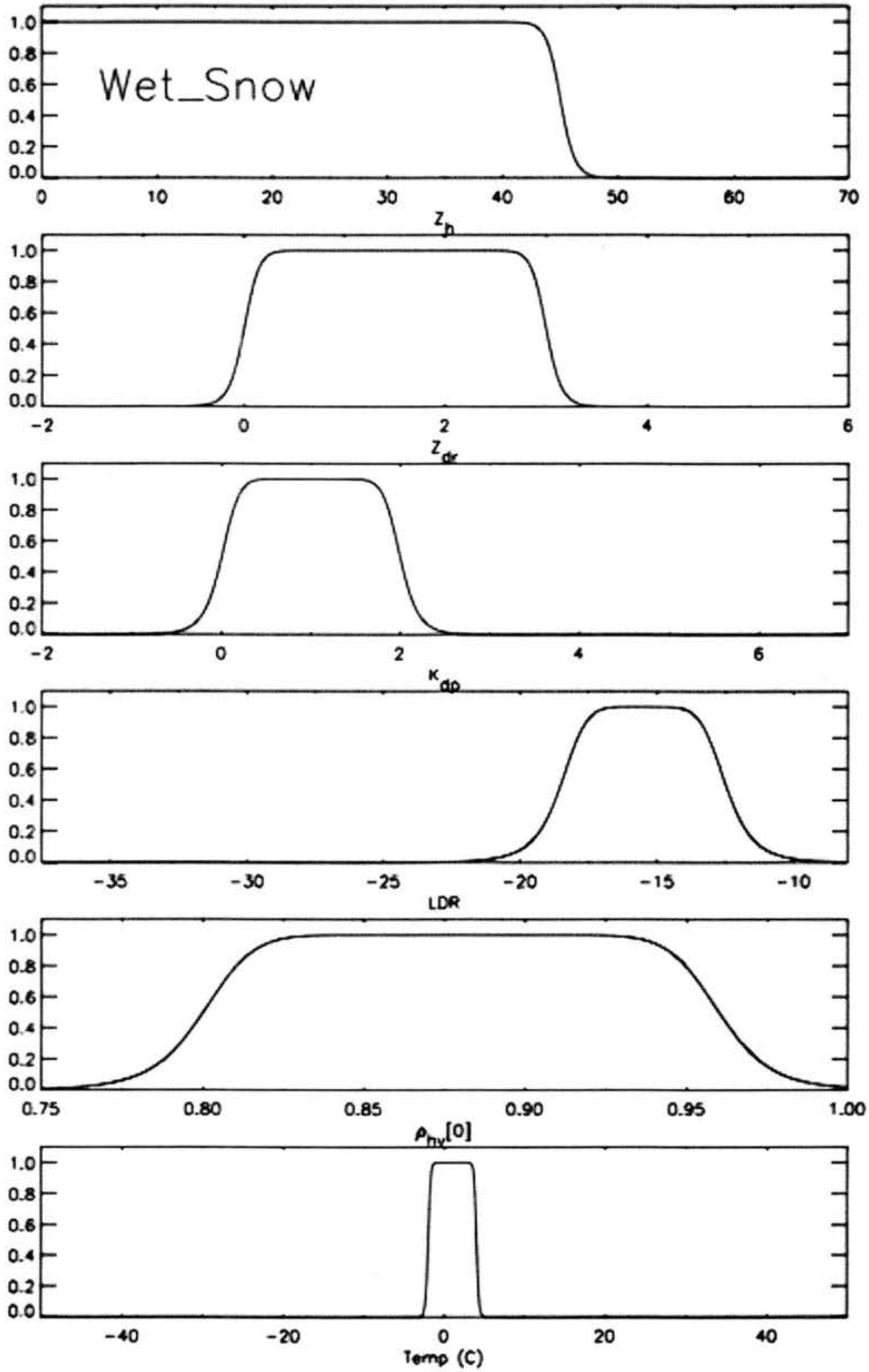

Figure A.11: Fuzzy logic MBF for Wet Snow.

Tables A.1-A.11: Variable threshold ranges for selected hydrometeor types from Straka et al. (2000) (S2000), Carey and Rutledge (1998) (CR1998), Liu and Chandrasekar (2000) (LC2000), Lopez and Aubagnac (1997) (LA1997), and Lim (2001) (Lim2001). FHC(2004) refers to the fuzzy logic hydrometeor classification algorithm used in this thesis. 'NA' indicates that variable was not used to classify the hydrometeor type. (Tables courtesy of K. Wiens, personal communication, 2004)

Table A.1: Drizzle

Source	Z_h	Z_{dr}	K_{dp}	L_{DR}	ρ_{hv}	**T**
S(2000)	< 28	0-0.07	0-0.03	< -32	> 0.97	> 0
LC(2000)	< 25	0-1.1	-0.1 to 0.1	< -34	> 0.98	NA
Lim(2001)	< 20	0-0.7	0-0.1	< -33	> 0.97	> 0
FHC(2004)	< 28	0-0.7	-0.1 to 0.1	< -32	> 0.97	> 0

Table A.2: Rain

Source	Z_h	Z_{dr}	K_{dp}	L_{DR}	ρ_{hv}	**T**
S(2000)	28-60	> 0.7	> 0.03	> -34 to –25	> 0.95	> -10
LC(2000)[1]	25-60	2-D	> 0	> -33 to –27	> 0.97	NA
CR(1998)	< 60	> 0.5	> 0.5	< -27	> 0.97	> 0
LA(1997)	25-60	0.5-4	0-10	NA	NA	NA
Lim(2001)[1]	15-60	2-D	2-D	-36 to –17	> 0.95	NA
FHC(2004)	25-60	> 0.7	0.03-6	-33 to -27	> 0.95	> -10

[1] Liu and Chandrasekar (2000) and Lim (2001) use 2-D MBFs for radar measurements of variables that are correlated for certain hydrometeor types. These functions are in a two-dimensional space including Z_h and the variable.

Table A.3: Large Hail (D > 2 cm)

Source	Z_h	Z_{dr}	K_{dp}	L_{DR}	ρ_{hv}	T
S(2000)	> 55	-2 to 0.5	-0.5 to 1	> -20	< 0.92	> -25
LC(2000)	> 55	< -0.5	-1 to 1	-15 to –10	> 0.96	NA
CR(1998)[2]	> 55	< 0.5	< 0.5	> -18 (>-26)	< 0.96(> 0.97)	> 0 (<0)
LA(1997)	55-70	< 0.5	-1 to 1	NA	NA	NA
Lim(2001)	> 55	< 0.5	-0.5 to 1	> -20	0.84 to 0.92	NA
FHC(2004)	> 55	< 0.5	-0.5 to 1	> -20	0.85 to 0.92	NA

Table A.4: Large Hail and Rain

Source	Z_h	Z_{dr}	K_{dp}	L_{DR}	ρ_{hv}	T
FHC	> 55	-0.5 to 3	0.5 – 6.5	> -22	< 0.92	> -10
S(2000)	> 55	-0.5 to 3	> 0	> -22	< 0.92	> -10
LC(2000)	> 50	-1 to 1	> 0	-20 to –10	> 0.9	NA
CR(1998)	> 55	< 1	> 0.5	> -20	< 0.96	> 0
LA(1997)	50-70	-1 to 1	0-10	NA	NA	NA
Lim(2001)[1]	> 45	2-D	2-D	-24 to –14	< 0.94	NA
FHC(2004)	> 55	0.5-3	0.5-0.65	-20 to -10	< 0.93	> -10

Table A.5: Small Hail

Source	Z_h	Z_{dr}	K_{dp}	L_{DR}	ρ_{hv}	T
S(2000)	45-60	-0.5 to 0.5	-0.5 to 0.5	-26 to –20	0.92-0.97	> -15
LC(2000)	50-60	-0.5 to 0.5	-0.5 to 0.5	< -20	NA	NA
CR(1998)[2]	> 50 (> 55)	< 0.5	< 0.5	< -18 (> -26)	> 0.96 (> 0.97)	> 0 (< 0)
LA(1997)	50-60	-0.5 to 0.5	-0.5 to 0.5	NA	NA	NA
Lim(2001)	50-60	-1 to 0.5	-0.5 to 0.5	> -25	0.91-0.98	NA
FHC(2004)	50-60	-0.5 to 0.5	-0.5 to 0.5	-24 to –18	0.92-0.98	NA

[2] Carey and Rutledge (1998) identify different parameters for hail if it is located above the freezing level or below the freezing level. In these tables, the () values correspond to values when hail is below the melting level.

Table A.6: Small Hail and Rain

Source	Z_h	Z_{dr}	K_{dp}	L_{DR}	ρ_{hv}	T
S(2000)	45-60	-0.5 to 6	> 0	> -25	< 0.95	> -5
LC(2000)	>50	-1 to 1	> 0	-20 to –10	> 0.9	NA
CR(1998)	> 50	< 1	> 0.5	-27 to –20	< 0.98	> 0
LA(1997)	50-70	-1 to 1	0-10	NA	NA	NA
Lim(2001)	> 45	2-D	2-D	-24 to –14	< 0.94	NA
FHC(2004)	45-60	> -0.5	-0.5 to 6.5	-26 to –19	< 0.95	> -5

Table A.7: Vertical Ice

Source	Z_h	Z_{dr}	K_{dp}	L_{DR}	ρ_{hv}	T
S(2000)	< 35	-0.5 to 0.5	-0.6 to 0	< -24	> 0.95	< 0
CR(1998)	< 40	NA	< -0.25	NA	NA	< -20
FHC(2004)	< 35	-0.5 to 0.5	< -0.25	< -25	> 0.95	< 0

Table A.8: Dry Graupel

Source	Z_h	Z_{dr}	K_{dp}	L_{DR}	ρ_{hv}	T
S(2000)	20-35	-0.5 to 1	0-0.5	< -25	> 0.95	< 0
LC(2000)	40-50	-0.5 to 1	-0.5 to 0.5	< -30	> 0.96	NA
LA(1997)	40-50	-0.5 to 1	-0.5 to 0.5	NA	NA	NA
Lim(2001)	20-45	2-D	2-D	-30 to –25	> 0.95	NA
FHC(2004)	30-45	-0.5 to 1	-0.5 to 0.5	< -30	> 0.97	< 0

Table A.9: Wet Graupel

Source	Z_h	Z_{dr}	K_{dp}	L_{DR}	ρ_{hv}	T
S(2000)	30-50	-0.5 to 2	0-1.5	-30 to –20	> 0.95	> -15
LC(2000)	40-55	-0.5 to 3	-0.5 to 2	-25 to –20	> 0.95	NA
LA(1997)	40-55	-0.5 to 3	-0.5 to 2	NA	NA	NA
Lim(2001)[1]	30-52	2-D	2-D	-27 to –18	> 0.94	NA
FHC(2004)	40-55	-0.5 to 3	-0.5 to 2	-25 to –20	> 0.95	-15 to 10

Table A.10: Dry Snow

Source	Z_h	Z_{dr}	K_{dp}	L_{DR}	ρ_{hv}	**T**
S(2000)	< 35	0-6	0-0.6	< -25	> 0.95	< 0
LC(2000)	< 35	0-5	0-1	< -25	> 0.95	NA
Lim(2001)	10-35	-0.1 to 1	-0.1 to 0.2	< -24	> 0.95	NA
FHC(2004)	< 35	> -0.1	0-0.6	< -25	> 0.95	< 0

Table A.11: Wet Snow

Source	Z_h	Z_{dr}	K_{dp}	L_{DR}	ρ_{hv}	**T**
S(2000)	< 45	0.5-3	0-0.5	-10 to –20	0.5-0.9	> 0
LC(2000)	< 45	0-3	0-2	-18 to –15	0.82-0.95	NA
Lim(2001)	28-45	-0.1 to 3	-0.1 to 0.5	> -23	< 0.9	NA
FHC(2004)	< 45	0-3	0-2	-18 to –13	0.82-0.95	-2 to 4

B. Rain rate comparisons with Gauge data

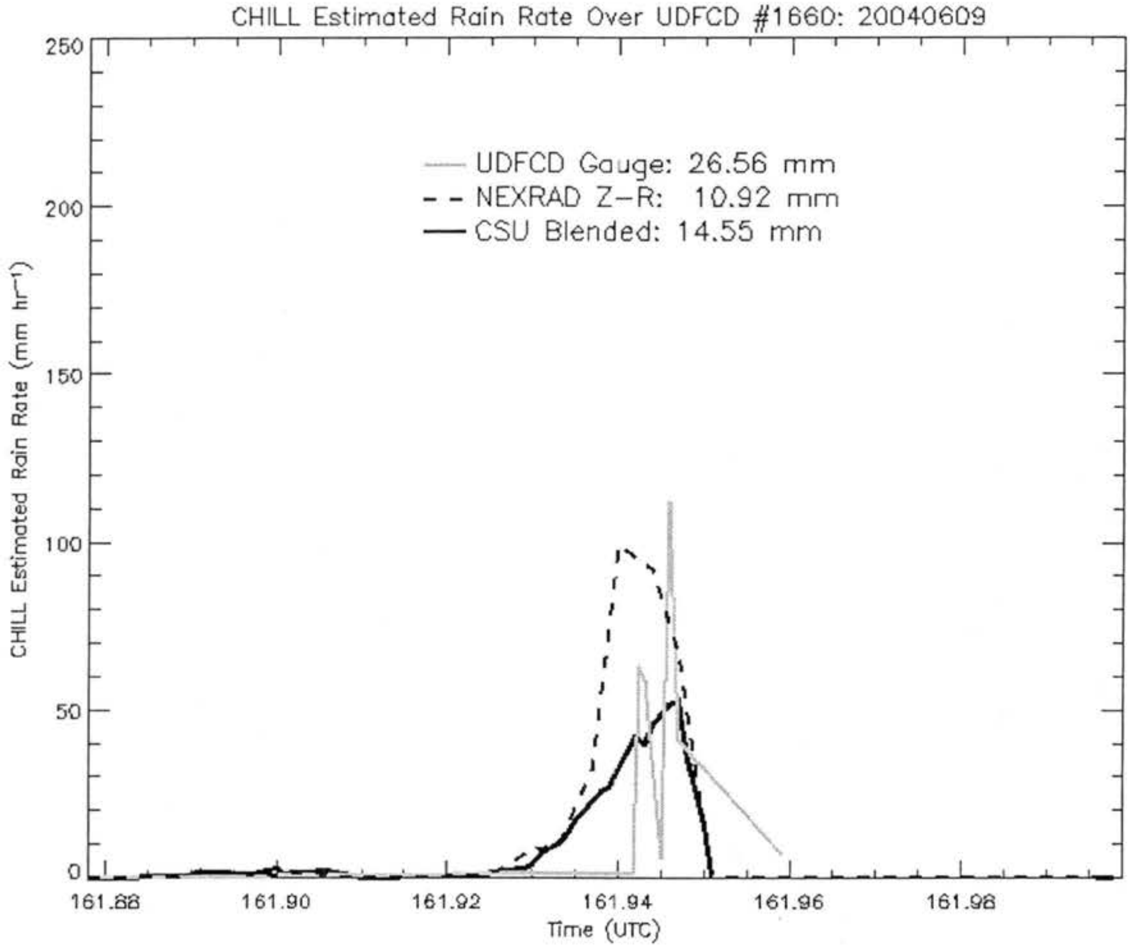

Figure B.1 Rain rate trace over the UDFCD gauge #1660 on 09 June 2004. CSU blended algorithm is the black solid line, the NEXRAD Z-R relation is the dashed line, and the gauge is the gray solid trace. Time is in fraction of a Julian day, beginning at 2100 UTC and ending at 2359 UTC.

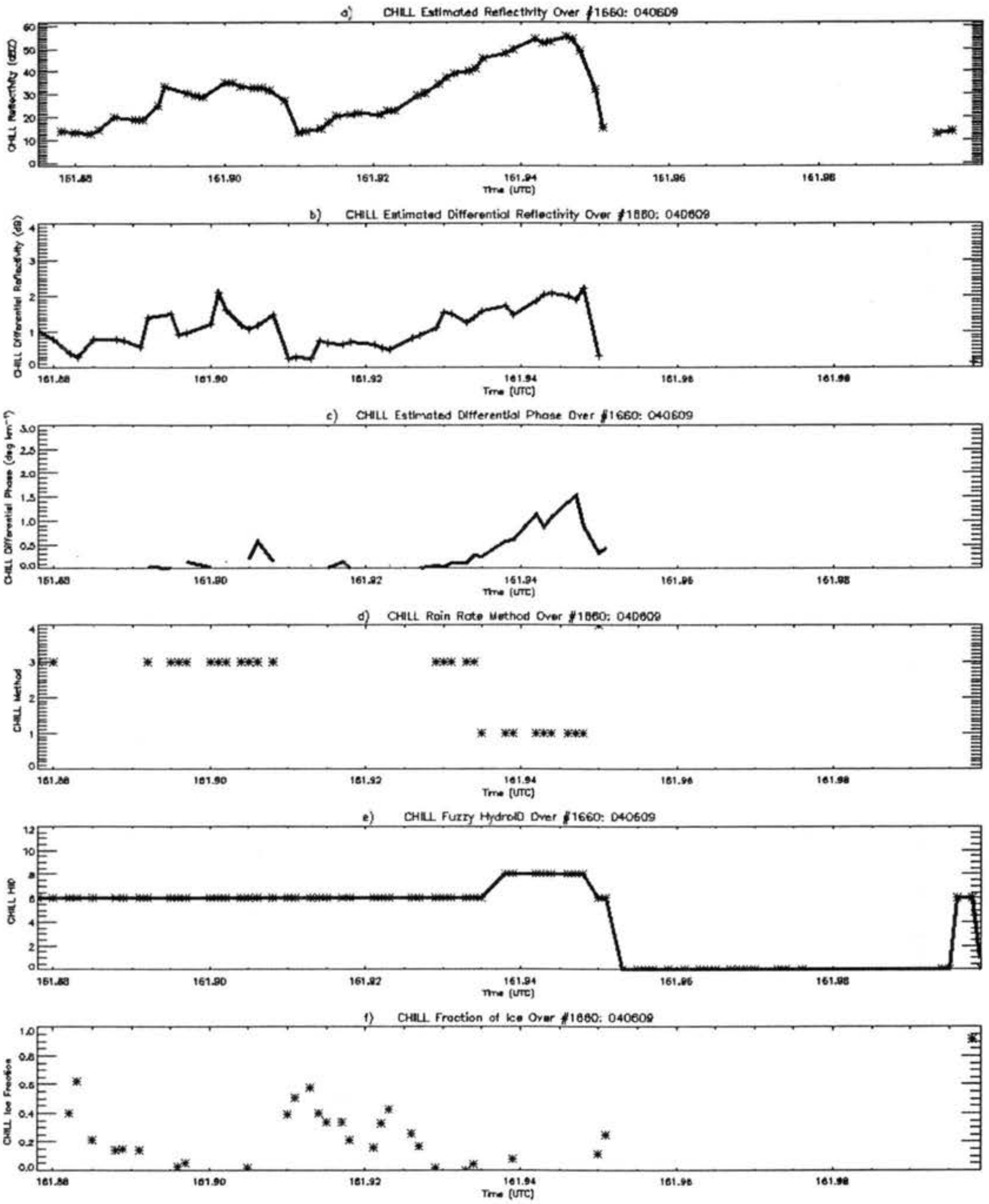

Figure B.2 Time series of CHILL data on 09 June 2004 over UDFCD gauge #1660 for a) Reflectivity, b) differential reflectivity, c) differential phase, d) blended algorithm rain rate calculation method, e) fuzzy logic hydrometeor type, and f) fraction of ice. The methods correspond to 1=R(K_{dp}, Z_{dr}), 2=R(K_{dp}), 3=R(Z_h, Z_{dr}) and R(Z_h). Hydrometeor types correspond to 0=no data, 1=drizzle, 2=rain, 3=dry snow, 4=wet snow, 5=vertical ice, 6=dry graupel, 7=wet graupel, 8=small hail, 9=large hail, 10=small hail mixed with rain, and 11=large hail mixed with rain. Time is in fraction of a Julian day, beginning at 2100 UTC and ending at 2359 UTC.

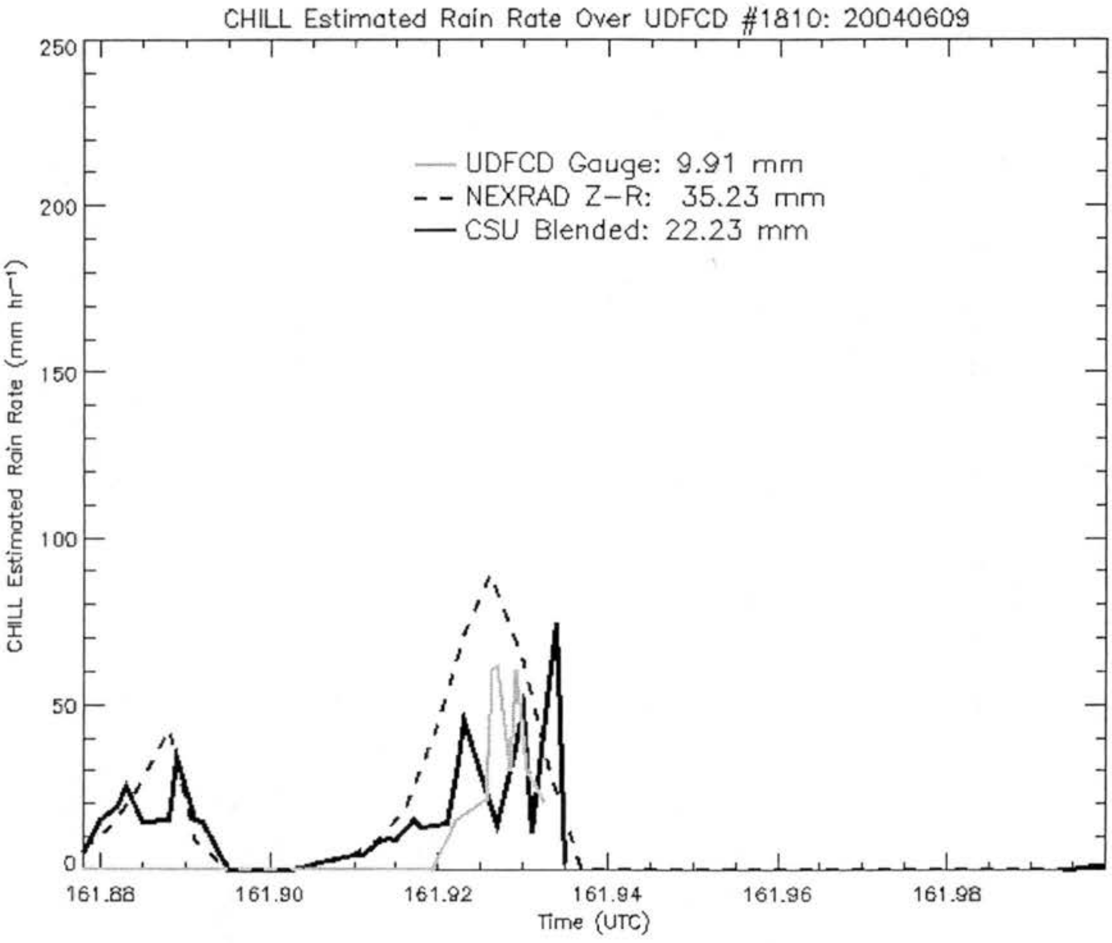

Figure B.3 Rain rate trace over the UDFCD gauge #1810 on 09 June 2004. CSU blended algorithm is the black solid line, the NEXRAD Z-R relation is the dashed line, and the gauge is the gray solid trace. Time is in fraction of a Julian day, beginning at 2100 UTC and ending at 2359 UTC.

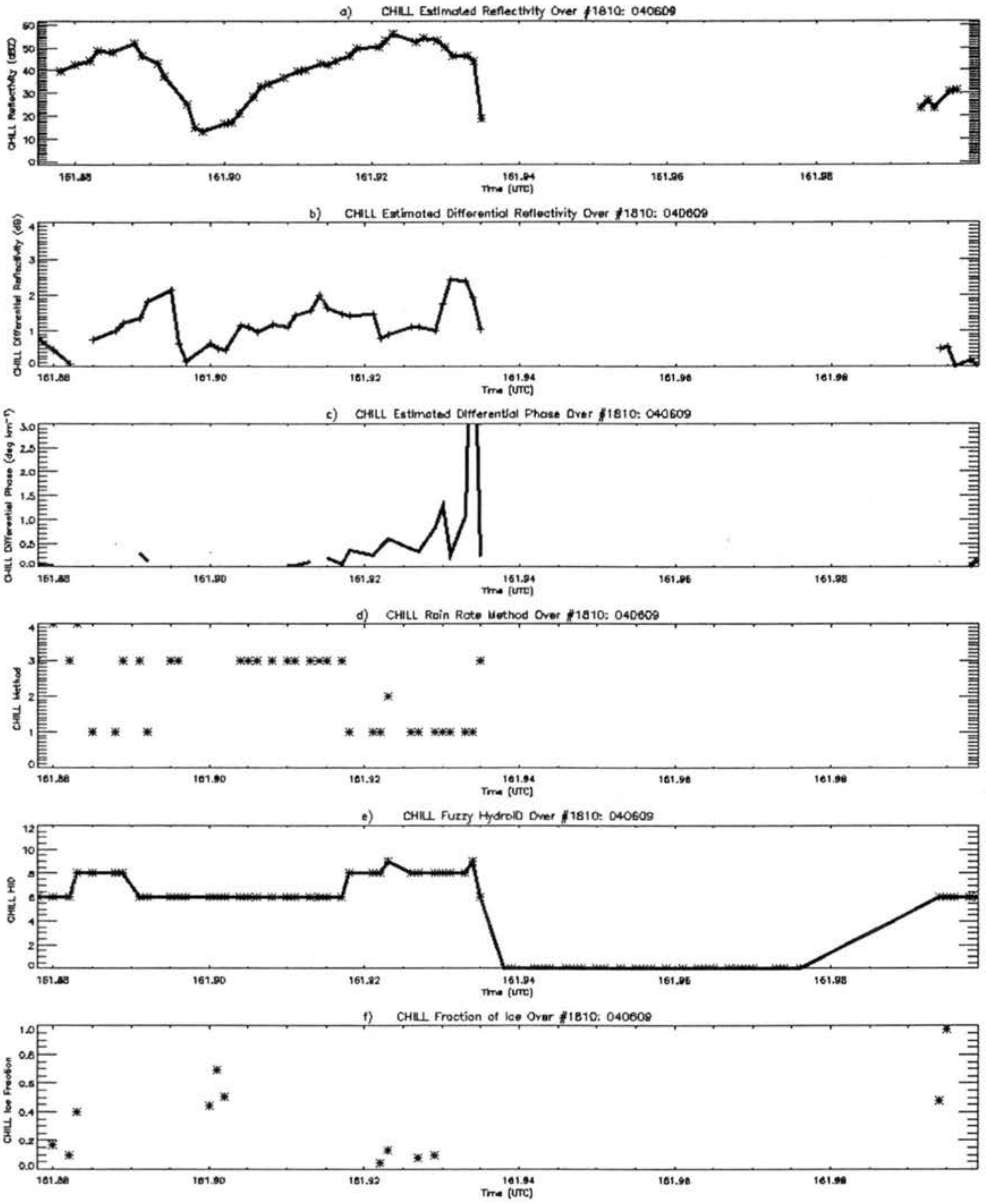

Figure B.4 Time series of CHILL data on 09 June 2004 over UDFCD gauge #1810 for a) Reflectivity, b) differential reflectivity, c) differential phase, d) blended algorithm rain rate calculation method, e) fuzzy logic hydrometeor type, and f) fraction of ice. The methods correspond to 1=R(K_{dp}, Z_{dr}), 2=R(K_{dp}), 3=R(Z_h, Z_{dr}) and R(Z_h). Hydrometeor types correspond to 0=no data, 1=drizzle, 2=rain, 3=dry snow, 4=wet snow, 5=vertical ice, 6=dry graupel, 7=wet graupel, 8=small hail, 9=large hail, 10=small hail mixed with rain, and 11=large hail mixed with rain. Time is in fraction of a Julian day, beginning at 2100 UTC and ending at 2359 UTC.

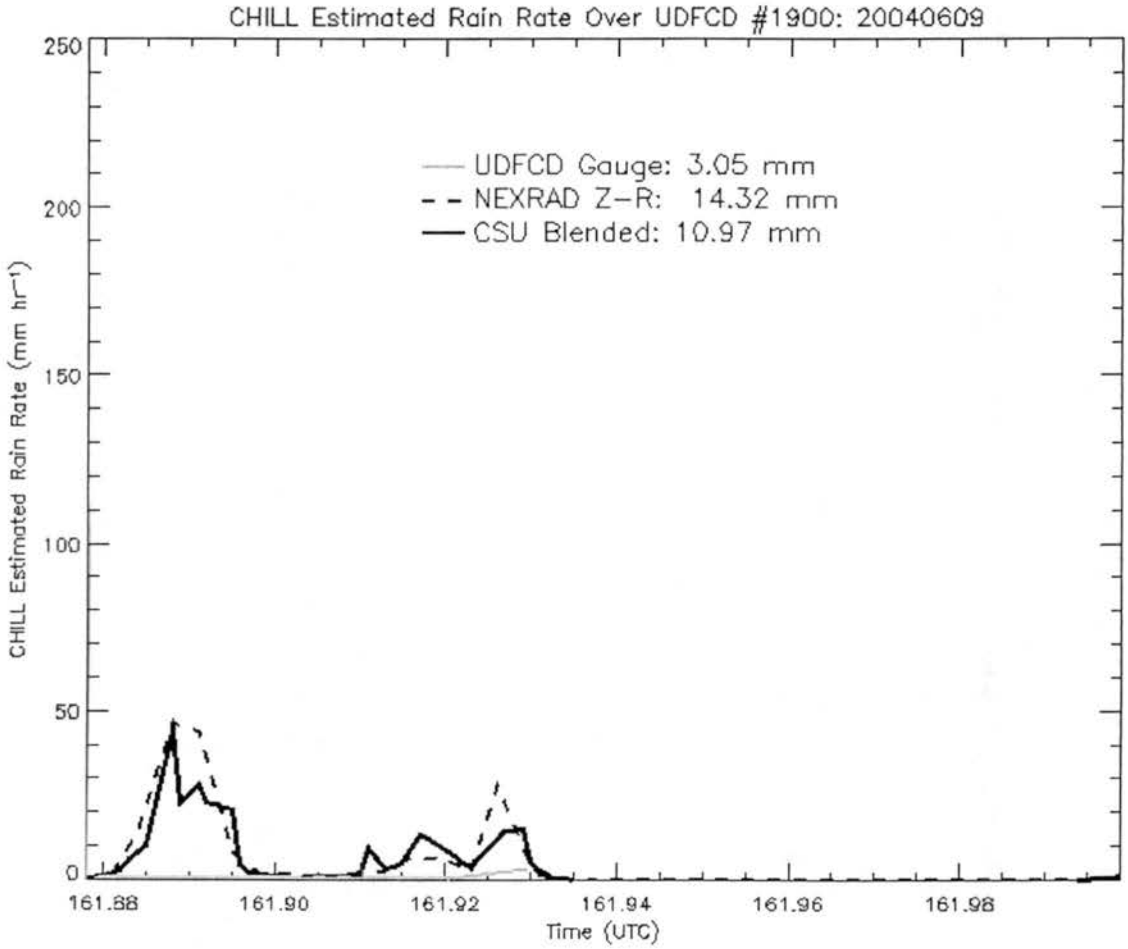

Figure B.5 Rain rate trace over the UDFCD gauge #1900 on 09 June 2004. CSU blended algorithm is the black solid line, the NEXRAD Z-R relation is the dashed line, and the gauge is the solid gray trace. Time is in fraction of a Julian day, beginning at 2100 UTC and ending at 2359 UTC.

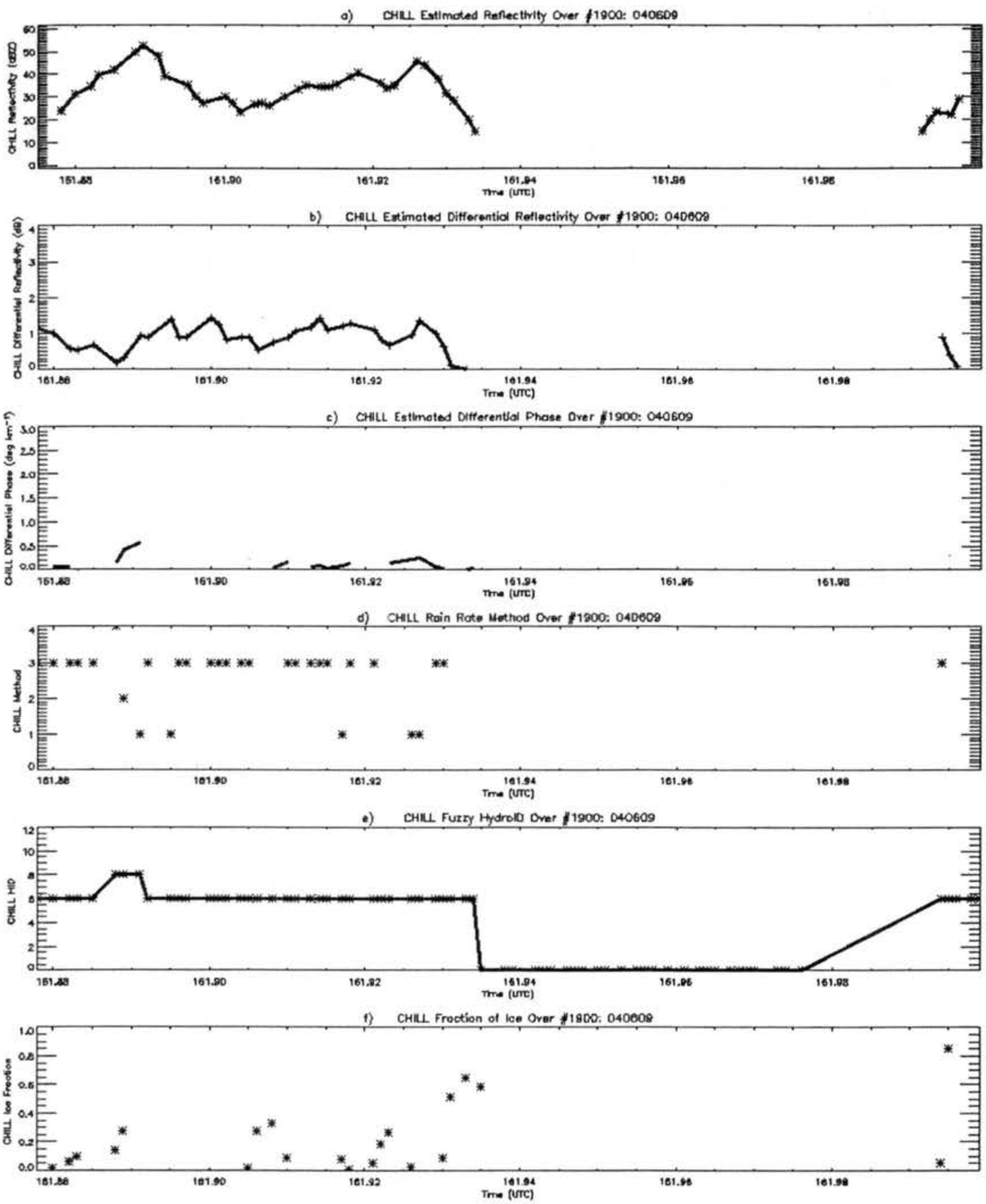

Figure B.6 Time series of CHILL data on 09 June 2004 over UDFCD gauge #1900 for a) Reflectivity, b) differential reflectivity, c) differential phase, d) blended algorithm rain rate calculation method, e) fuzzy logic hydrometeor type, and f) fraction of ice. The methods correspond to 1=R(K_{dp}, Z_{dr}), 2=R(K_{dp}), 3=R(Z_h, Z_{dr}) and R(Z_h). Hydrometeor types correspond to 0=no data, 1=drizzle, 2=rain, 3=dry snow, 4=wet snow, 5=vertical ice, 6=dry graupel, 7=wet graupel, 8=small hail, 9=large hail, 10=small hail mixed with rain, and 11=large hail mixed with rain. Time is in fraction of a Julian day, beginning at 2100 UTC and ending at 2359 UTC.

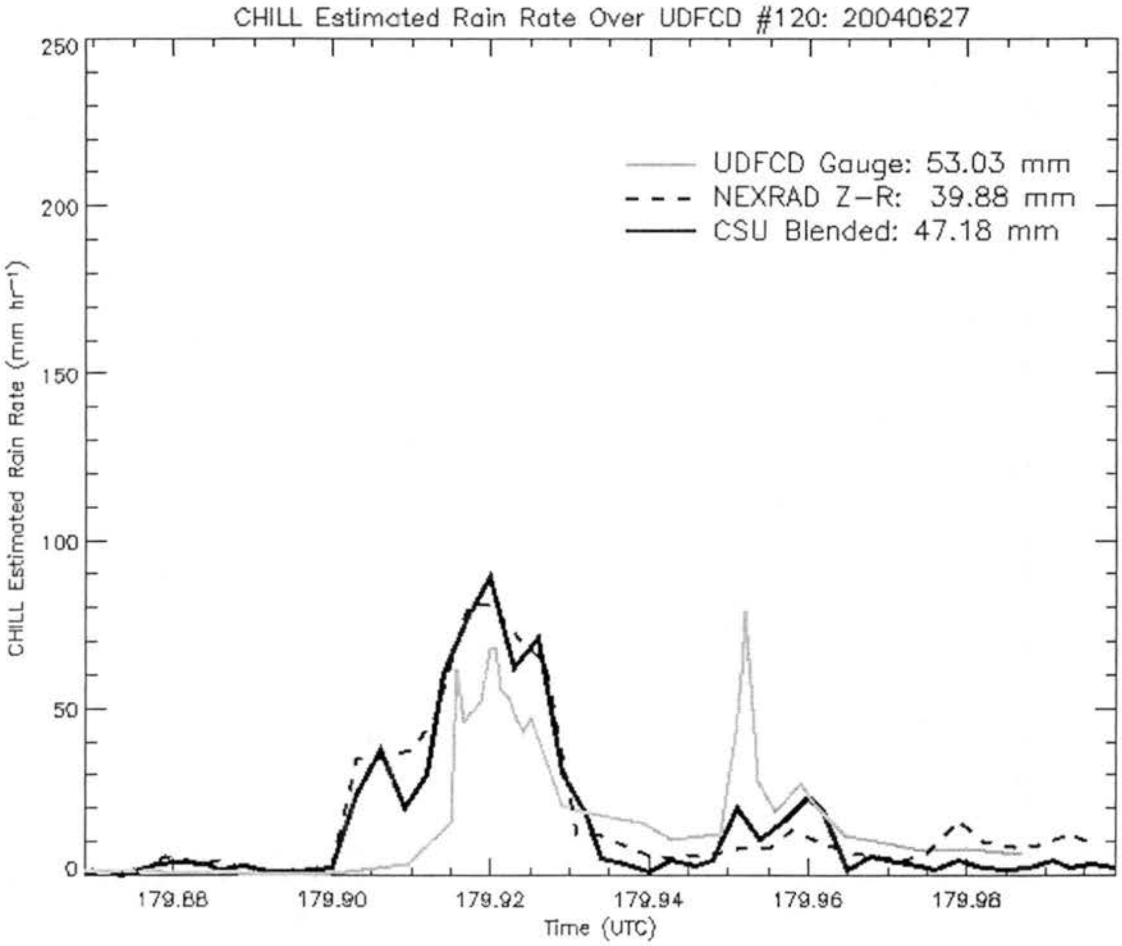

Figure B.7 Rain rate trace over the UDFCD gauge #120 on 27 June 2004. CSU blended algorithm is the black solid line, the NEXRAD Z-R relation is the dashed line, and the gauge is the solid gray trace. Time is in fraction of a Julian day, beginning at 2100 UTC and ending at 2359 UTC.

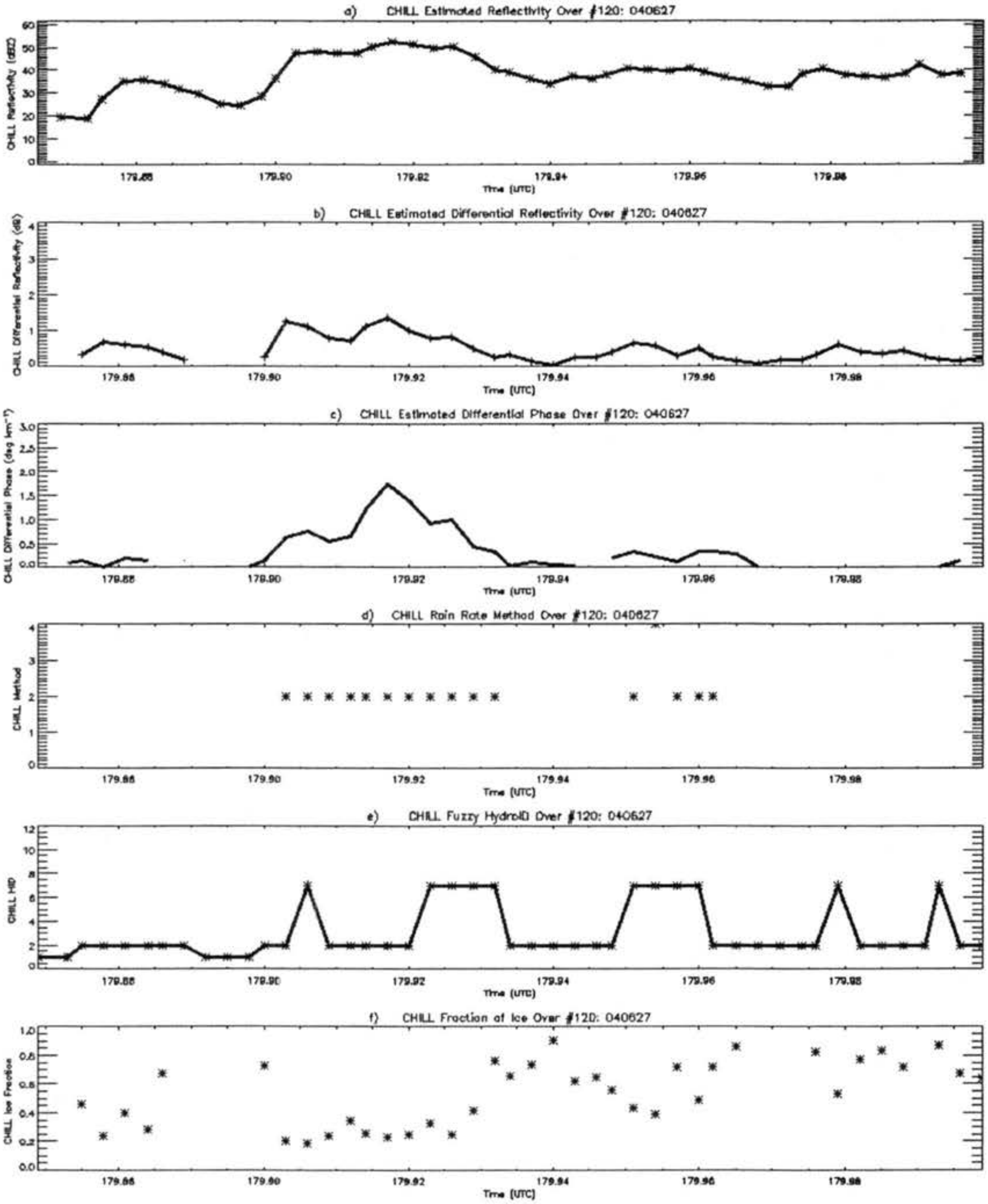

Figure B.8 Time series of CHILL data on 27 June 2004 over UDFCD gauge #120 for a) Reflectivity, b) differential reflectivity, c) differential phase, d) blended algorithm rain rate calculation method, e) fuzzy logic hydrometeor type, and f) fraction of ice. The methods correspond to 1=R(K_{dp}, Z_{dr}), 2=R(K_{dp}), 3=R(Z_h, Z_{dr}) and R(Z_h). Hydrometeor types correspond to 0=no data, 1=drizzle, 2=rain, 3=dry snow, 4=wet snow, 5=vertical ice, 6=dry graupel, 7=wet graupel, 8=small hail, 9=large hail, 10=small hail mixed with rain, and 11=large hail mixed with rain. Time is in fraction of a Julian day, beginning at 2100 UTC and ending at 2359 UTC.

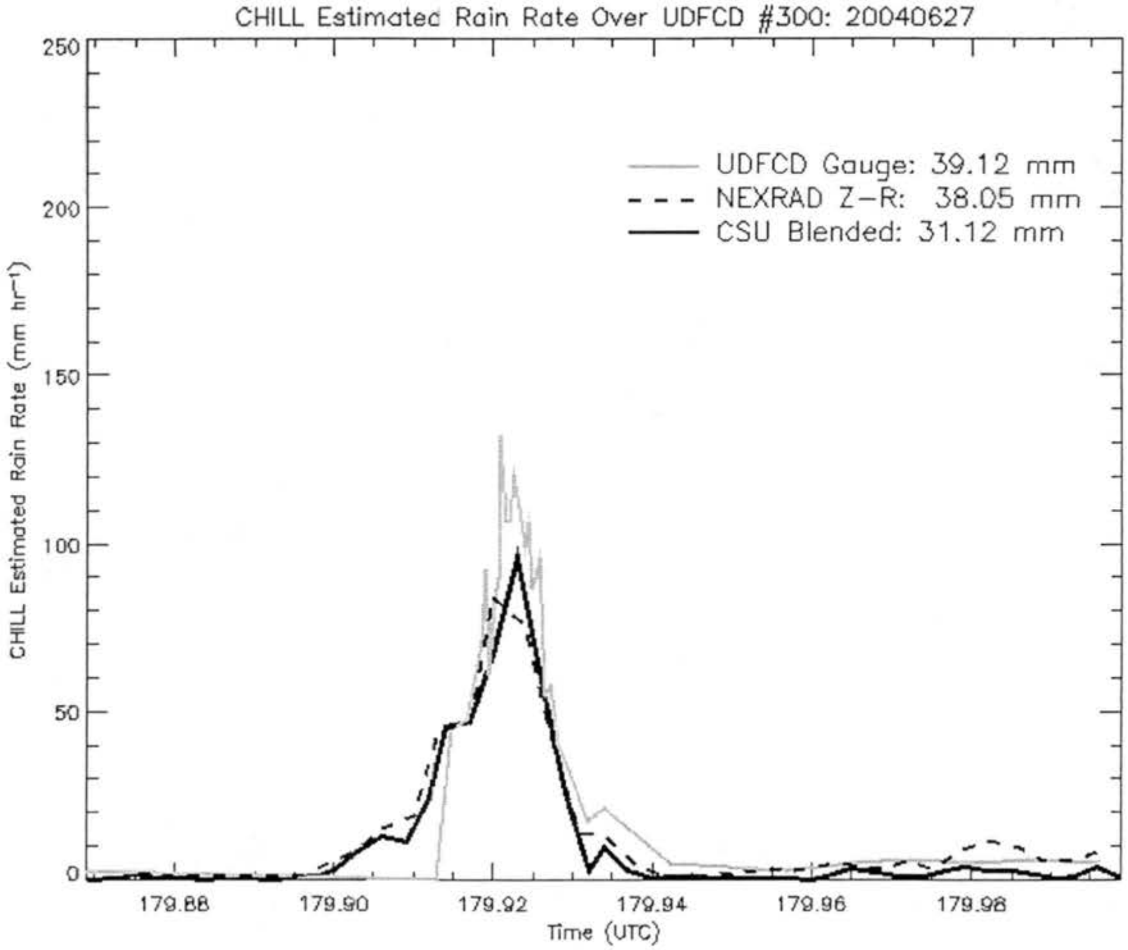

Figure B.9 Rain rate trace over the UDFCD gauge #300 on 27 June 2004. CSU blended algorithm is the black solid line, the NEXRAD Z-R relation is the dashed line, and the gauge is the solid gray trace. Time is in fraction of a Julian day, beginning at 2100 UTC and ending at 2359 UTC.

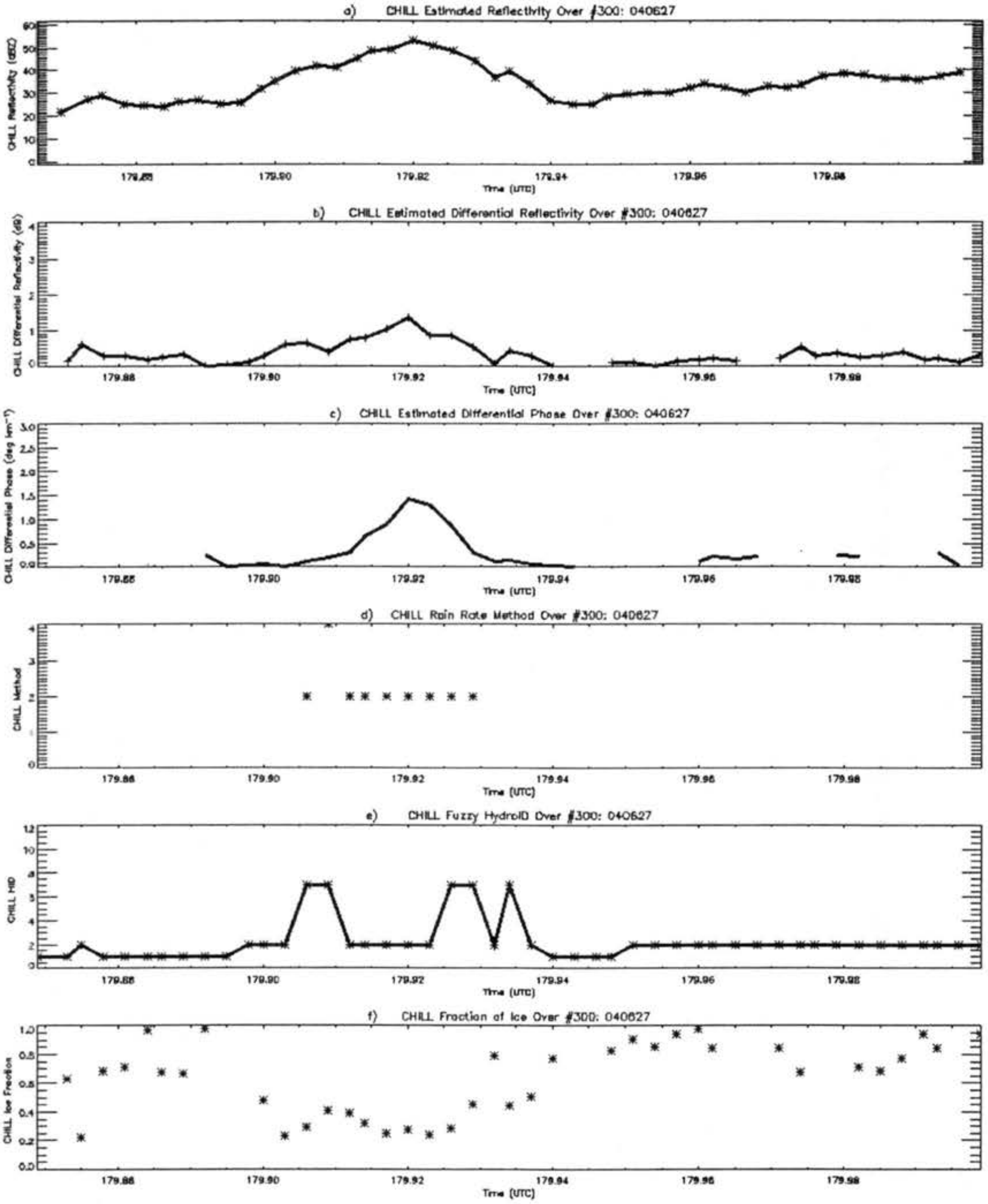

Figure B.10 Time series of CHILL data on 27 June 2004 over UDFCD gauge #300 for a) Reflectivity, b) differential reflectivity, c) differential phase, d) blended algorithm rain rate calculation method, e) fuzzy logic hydrometeor type, and f) fraction of ice. The methods correspond to 1=R(K_{dp}, Z_{dr}), 2=R(K_{dp}), 3=R(Z_h, Z_{dr}) and R(Z_h). Hydrometeor types correspond to 0=no data, 1=drizzle, 2=rain, 3=dry snow, 4=wet snow, 5=vertical ice, 6=dry graupel, 7=wet graupel, 8=small hail, 9=large hail, 10=small hail mixed with rain, and 11=large hail mixed with rain. Time is in fraction of a Julian day, beginning at 2100 UTC and ending at 2359 UTC.

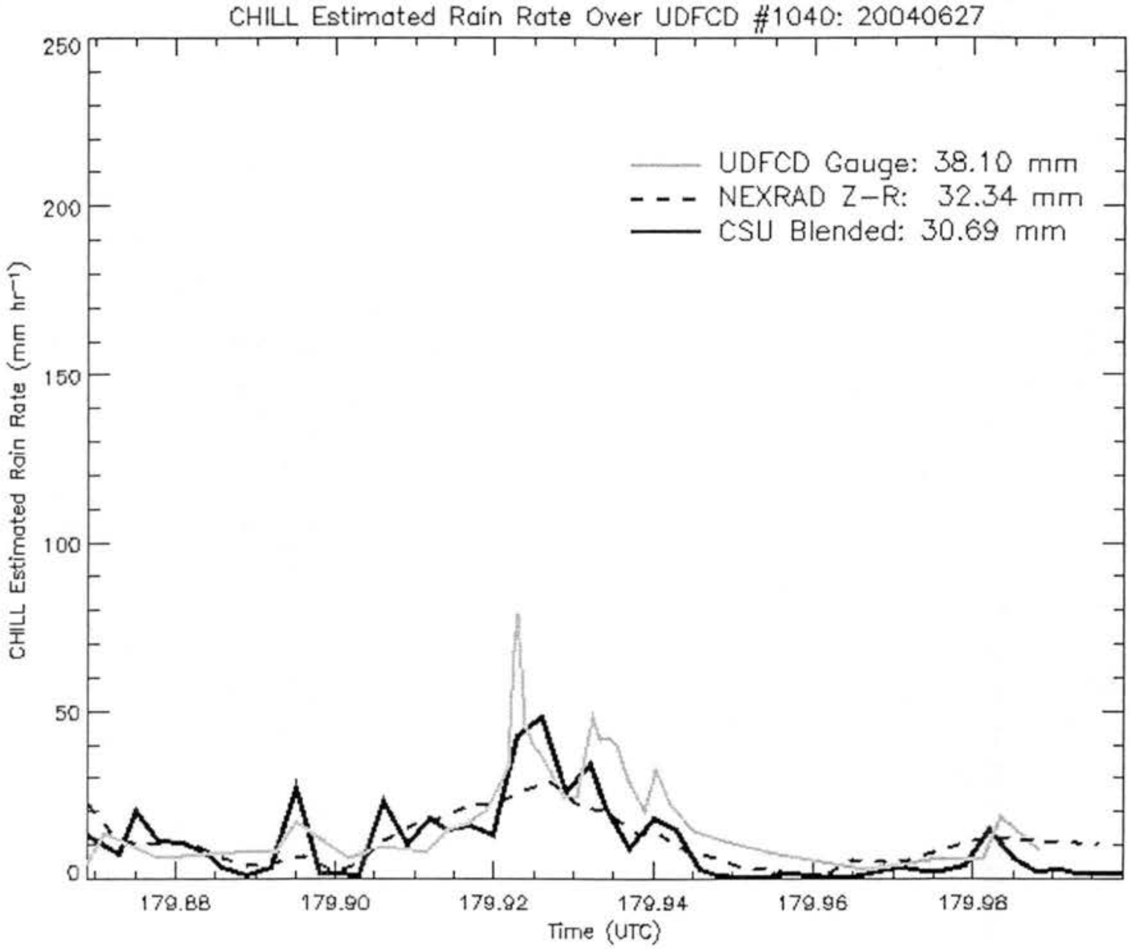

Figure B.11 Rain rate trace over the UDFCD gauge #1040 on 27 June 2004. CSU blended algorithm is the black solid line, the NEXRAD Z-R relation is the dashed line, and the gauge is the solid gray trace. Time is in fraction of a Julian day, beginning at 2100 UTC and ending at 2359 UTC.

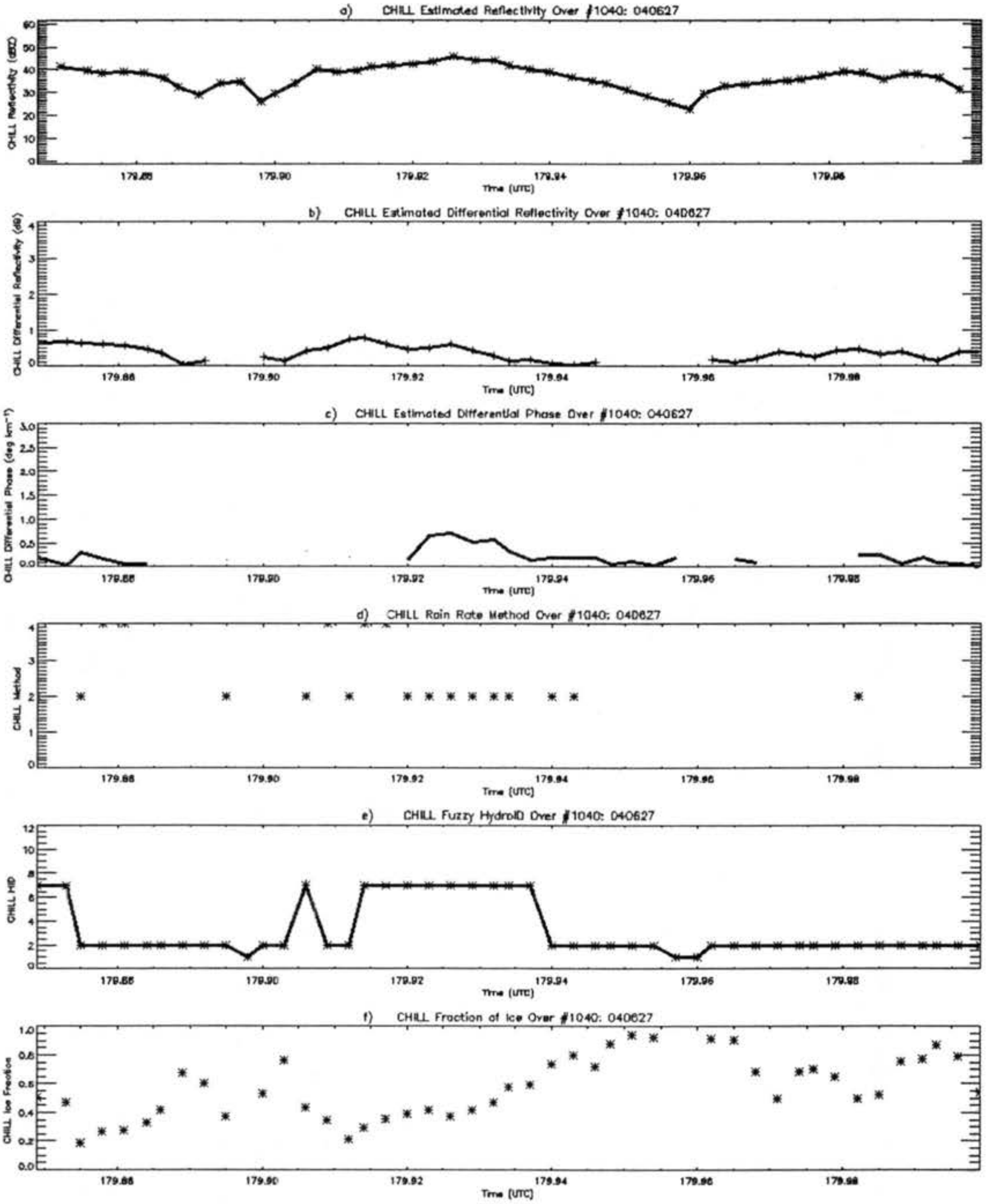

Figure B.12 Time series of CHILL data on 27 June 2004 over UDFCD gauge #1040 for a) Reflectivity, b) differential reflectivity, c) differential phase, d) blended algorithm rain rate calculation method, e) fuzzy logic hydrometeor type, and f) fraction of ice. The methods correspond to 1=R(K_{dp}, Z_{dr}), 2=R(K_{dp}), 3=R(Z_h, Z_{dr}) and R(Z_h). Hydrometeor types correspond to 0=no data, 1=drizzle, 2=rain, 3=dry snow, 4=wet snow, 5=vertical ice, 6=dry graupel, 7=wet graupel, 8=small hail, 9=large hail, 10=small hail mixed with rain, and 11=large hail mixed with rain. Time is in fraction of a Julian day, beginning at 2100 UTC and ending at 2359 UTC.

REFERENCES

Armijo, L., 1969: A theory for the determination of wind and precipitation velocities with Doppler radars. *J. Atmos. Sci.,* **26,** 570-575.

Aydin, K., Seliga, T.A. and V.N. Bringi, 1984: Differential radar scattering properties of model hail and mixed phase hydrometeors. *Radio Sci.,* **19**, 58-66.

Battan, L.J., 1973: *Radar Observations of the Atmosphere*. University of Chicago Press, 324pp.

Beard, K.V. and Chuang, C., 1987: A new model for the equilibrium shape of raindrops, *J. Atmos. Sci.,* **44**, 1509-1524.

Biter, C. J., and P.N. Johnson, 1982: Sunday Creek –The CCOPE operations center. *Bull. Am. Meteorol. Soc.*, **63**, 482-486.

Bohne, A. R., and R. C. Srivastava, 1975: Random errors in wind and precipitation fall speed measurement by a triple Doppler radar system. Univ. of Chicago, Tech. Report No 37, 50pp.

Bringi, V.N., and V. Chandrasekar, 2001: Polarimetric Doppler Weather Radar: Principles and Applications, Cambridge University Press, Cambridge, United Kingdom, 636pp.

Brown, Rodger, A., 1992: Initiation and Evolution of Updraft Rotation within an Incipient Supercell Thunderstorm. *J. Atmos. Sci.*, **49**, 1997-2014.

Carey, L. D., and S. A. Rutledge, 1996: A multiparameter radar case study of the microphysical and kinematic evolution of lightning producing storm, *Meteorol. Atmos. Phys.*, **59**, 33-64.

Carey, L. D., and S. A. Rutledge, 1998: Electrical and multiparameter radar observations of a severe hailstorm. *J. Geophys. Res.,* **103**, 13979-14000.

Chandrasekar, V., V. N. Bringi, N. Balakrishnan and D. S. Zrnić, 1990: Error structure of multiparameter radar and surface measurements of rainfall. Part III: Specific differential phase. *J. Atmos. Oceanic Tech.,* **7,** 621-629.

Chandrasekar, V., C. A. Atwater and T. H. Vonder Haar, 1991: Convective latent heating estimates from radar data, Preprints, *25th Conference on Radar Meteorology,* Paris, France, 155-158.

Chandrasekar, V., E. Gorgucci, and G. Scarchilli, 1993: Optimization of multiparameter radar estimates of rainfall. *J. Appl. Meteor.,* **32**, 1288-1293.

Chong, M., J.-F. Georgis, O. Bousquet, S. R. Brodzik, C. Burghart, S. Cosma, U. Germann, V. Gouget, R. A. Houze Jr., C. N. James, S. Prieur, R. Rotunno, F. Roux, J. Vivekanandan, and Z.-X. Zeng, 2000: Real-time wind synthesis from Doppler radar observations during the mesoscale alpine programme. *Bull. Am. Meteorol. Soc.,* **81**, 2953-2962.

Cifelli, R., D. Barjenbruch, D. Brunkow, L. Carey, C. Davey, N. Doesken, C. Gimmestad, T. Huse, P. Kennedy, and S. A. Rutledge, 2004: Evaluation of an operational polarimetric rainfall algorithm. AMS 31st Conference on Radar Meteorology, Seattle, WA, 6-12 August 2003.

Conway, J. W., and D. S. Zrnić, 1993: A study of embryo production and hail growth using dual-Doppler and multiparameter radars. *Mon. Wea. Rev.*, **121**, 2511-2528.

Cressman, G. P., 1959: An operational objective analysis system. *Mon. Wea. Rev.,* **87,** 367-374.

Cunning, John. B., 1986: The Oklahoma-Kansas Preliminary Regional Experiment for STORM-Central. *Bull. Am. Meteorol. Soc.*, **67**, 1478-1486.

Davies-Jones, R.P., 1979: Dual-Doppler radar coverage area as a function of measurement accuracy and spatial resolution. *J. Appl, Meteor.,* **18**, 1229-1233.

Doviak, R. J., and D.S. Zrnić, 1993: Doppler Radar and Weather Observations, 2nd Ed., Academic Press, San Diego, California, 562pp.

Dye, J. E., and B. E. Martner, 1978: The relationship between radar reflectivity factor and hail at the ground for northeast Colorado thunderstorms. *J. Appl. Meteor.,* **17**, 1335-1341.

Golestani, Y., V. Chandrasekar, and V. N. Bringi, 1989: Intercomparison of multiparameter radar measurements. Proc. 24th Conf. Radar Meteorology, Tallahassee, FL, Amer. Meteor. Soc., 309-314.

Groisman, P. Y., and D. R. Legates, 1994: The accuracy of United States precipitation data. *Bull. Amer. Meteorol. Soc*, **75**, 215-227.

Heymsfield, G. M., R. H. Blackmer, Jr., and S. Schotz, 1983: Upper-level structure of Oklahoma tornadic storms on 2 May 1979. I: Radar and Satellite Observations. *J. Atmos. Sci.*, **40**, 1740-1754.

Houze, R. A. Jr., S. A. Rutledge, M. I. Biggerstaff, and B. F. Smull, 1989: Interpretation of Doppler weather radar displays of midlatitude mesoscale convective systems. *Bull. Am. Meteorol. Soc.*, **70**, 608-619.

Houze, R. A. Jr., 1993: Cloud Dynamics, Academic Press, San Diego, California, 573pp.

Humphrey, M. D., Istok, J. D., Lee, J. Y., Hevesi, J. A., Flint, A. L.. 1997: A New Method for Automated Dynamic Calibration of Tipping-Bucket Rain Gauges. *Journal of Atmospheric and Oceanic Technology*: Vol. 14, No. 6, pp. 1513–1519.

James, C. N., S. R. Brodzik, H. Edmon, R. A. Houze Jr., and S. E. Yuter, 2000: Radar data processing and visualization over complex terrain. *Wea. Forecasting,* **15**, 327-338.

Jameson, A.R., 1985: Microphysical interpretation of multiparameter radar measurements in rain. Part III: interpretation and measurement of propagation differential phase shift between orthogonal linear polarizations. *J. Atmos. Sci.,* **42**, 607-614.

Knight, C.A., Ed., 1982: the Cooperative Convective Precipitation Experiment (CCOPE), 18 May-7August 1981. *Bull. Am. Meteorol. Soc.*, **63**, 386-398.

Lhermitte, R. M., and L.J. Miller, 1970: Doppler radar methodology for the observation of convective storms. *Preprints 14th Conf. Radar Meteorology,* Tucson, Amer. Meteor. Soc., 133-138.

Lim, Sanghun, 2001: Fuzzy logic for hydrometeor classification from polarimetric radar measurements. Master's thesis, Colorado State University, Department of Electrical and Computer Engineering, 97pp.

Liu, H., and V. Chandrasekar, 2000: Classification of hydrometeors based on polarimetric radar measurements: Development of fuzzy logic and neuro-fuzzy systems, and in situ verification. *J. Atmos. Oceanic Tech.,* **17,** 140-164.

Lopez, R. E., and J. P. Aubagnac, 1997: The lightning activity of a hailstorm as a function of changes in its microphysical characteristics inferred from polarimetric radar observations. *J. Geophys. Res.*, **102,** 16799-16813.

Mohr, C. G., and L. J. Miller, 1983: CEDRIC – A software package for Cartesian space editing, synthesis and display of radar fields under interactive control. *Preprints, 21st Conf. On Radar Meteorology,* Boston, *Amer. Meteor. Soc.,* 569-574.

Nemec, J., 1969: Instruments, methods of observation and processing of basic data on precipitation and evaporation. Hydrometeorological Instruments, *Observations and Networks in Africa*, D. A. Davies, Ed., World Meteorological Organization, 11-61.

O'Brien, J.J., 1970: Alternative solutions to the classical vertical velocity problem. *J. Appl. Meteor.,* **9,** 197-203.

Parkin, D. A., W. D. King and D. E. Shaw, 1982: An automatic recording raingage network for a cloud-seeding experiment. *J. Appl. Meteor.*, **21**, 227-236.

Petersen, W. A., L. D. Carey, S. A. Rutledge, J. C. Knievel, N. J. Doesken, R. H. Johnson, T. B. McKee, T. Vonder Haar and J. F. Weaver, 1999: Mesoscale and radar observations of the Fort Collins Flash Flood of 28 July 1997. *Bull. Amer. Meteorol. Soc.,* **80,** 191-216.

Protat, A., and I. Zawadzki, 1999: A variational method for real-time retrieval of three-dimensional wind filed form multiple-Doppler bistatic radar network data. *J. Atmos. Oceanic Technol.,* **16**, 432-449.

Pruppacher, H. R. and K. V. Beard, 1970: A wind tunnel investigation of the internal circulation and shape of water drops falling at terminal velocity in air. *Quart. J. Roy. Meteor. Soc.,* **96**, 247-256.

Rinehart, R. E., 1997: Radar for Meteorologists, Rinehart Publications, Grand Forks, North Dakota, 428pp.

Rutledge, S. A., R. C. Cifelli, S. Nesbitt, T. Lang, P. Kennedy, S. Matrosov, C Williams, V. N. Bringi, and V. Chandrasekar, 2004: The Front Range Pilot Project for GPM. International Precipitation Conference, Vancouver, BC, 8-11 August 2004.

Ryzhkov, A. V., and D. S. Zrnić, 1998: Polarimetric Rainfall Estimation in the Presence of Anomalous Propagation. *J. Atmos. Oceanic Tech.*, **15**, 1320-1330.

Satoh, S., and J. Wurman, 1999: Accuracy of composite wind fields derived from a bistatic multiple-Doppler radar network. Preprints, *29th Int. Conf. On Radar Meteorology,* Montreal, PQ, Canada, Amer. Meteor. Soc., 221-224.

Straka, J. M., D. S. Zrnić, and A. V. Ryzhkov, 2000: Bulk hydrometeor classification and quantification using polarimetric radar data: Synthesis of relations. *J. Appl. Meteor.*, **39**, 1341-1372.

Vivekanandan, J., D.S. Zrnić, S.M. Ellis, R. Oye, A. V. Ryzhkov, and J. Straka, 1999: Cloud microphysics retrieval using S-band dual-polarization radar measurements. *Bull. Am. Meteorol. Soc.*, **80**, 381-388.

Wurman, J., 1994: Vector winds form a single-transmitter bistatic dual-Doppler radar network. *Bull. Amer. Meteor. Soc.*,**75**, 983-994.

Zrnić, D.S., A. Ryzhkov, J. Straka, Y. Liu, and J. Vivekanandan, 2001: Testing a procedure for automatic classification of hydrometeor types. *J. Atmos. Oceanic Tech.*, **18**, 892-913.